UNIVERSITY OF CAPE TOWN

Uniaxial Strain Effect on Graphene-Nanoribbon Resonant Tunneling Transistors

Author:
Mahmood Akbari

Supervisor:
Prof. Alireza Baghai-Wadji

A thesis submitted in fulfillment of the requirements for the degree of Master of Science

in the

Computational Electronics Group
Department of Electrical Engineering

October 15, 2018

Declaration of Authorship

I know the meaning of plagiarism and declare that all the work in the document, save for that which is properly acknowledged, is my own. This dissertation has been submitted to the Turnitin module and I confirm that my supervisor has seen my report and any concerns revealed by such have been resolved with my supervisor.

Signed by candidate

Mahmood Akbari

October 15, 2018

"*There are only two ways to live your life. One is as though nothing is a miracle. The other is as though everything in a miracle.*"

Albert Einstein (1879 - 1955)

UNIVERSITY OF CAPE TOWN

Abstract

Faculty of Engineering and the Built Environment

Department of Electrical Engineering

Master of Science

Uniaxial Strain Effect on Graphene-Nanoribbon Resonant Tunneling Transistors

by Mahmood Akbari

Graphene is an atomically thin two-dimensional (2-D) crystal with unique thermal, mechanical, and electronic transport properties such as the high mobility of carriers, perfect 2-D confinement and linear dispersion, etc., has been attracted many interest as a promising candidate for nano-scale devices over the past decades. Multilayer stacks of graphene and other stable, atomically thin, 2-D materials offer the prospect of creating a new class of heterostructure materials. Hexagonal boron- nitride (hBN), is a great candidate to be stacked with graphene due to an atomically 2-D layered structure with a lattice constant very similar to graphene (1.8% mismatch), large electrical band gap (~ 4.7 eV) , and excellent thermal and chemical stability. The graphene/hBN based tunneling transistors show the resonant tunneling and strong negative differential resistance (NDR). These devices which have potential for future high-frequency and logic applications such as high-speed IC circuits, signal generators, data storage, etc., has been studied both theoretically and experimentally recently.

The aim in this dissertation has been to study the effect of the uniaxial strain on the graphene nanoribbon resonant tunneling transistors (RTTs). The uniaxial strain may be induced either by an external stress applied to the graphene in a particular direction or by a substrate due to deposition of graphene on top of the other materials. The strain modifies distances between carbon atoms which leading to different hopping amplitudes among neighboring sites.

A resonant tunneling transistor consisting of armchair graphene nanoribbon (AGNR) electrodes with three layers of hBN tunnel barrier between them has been considered. By using the nearest-neighbor tight-bind (TB) method and the nonequilibrium Green function (NEGF) formalism, the electronic transport characteristics of RTT is calculated. In this work, we focus on how the strain affects the current-voltage characteristics of AGNR/hBN RTT.

Acknowledgements

First and foremost, I would like to thank my advisor, Prof. Alireza Baghai-Wadji, for his trust and support. Without his gracious offer for me to work at the Computational Electronics Group, none of this would have ever happened. His patience allowed me to steadily work on some of the most interesting projects that I have ever worked on.

I also would like to extend my special thanks to my friend, Dr. Mohsen Modarresi, who has given me immeasurable guidance to gain deeper insight of the field of nano-scaled materials and to Dr. Yunqi Zhao and Prof. Nobuya Mori for their helpful and valuable discussions. Helpful discussions with Dr Razieh Morad are also gratefully acknowledged.

Additionally, I thank the Council for Scientific and Industrial Research (CSIR) for supporting me awarding a scholarship: CSIR-DST Inter-Programme Bursary Award.

Finally, and most importantly, I would like to thank my wife, Razieh, for her unwavering support throughout the tough times, and my parents for their trust, inspiration and support.

Contents

List of Figures

List of Tables

List of Abbreviations

1-D	**O**ne **D**imentional
2-D	**T**wo **D**imentional
3-D	**T**hree **D**imentional
hBN	**h**exagonal **B**oron **N**itride
NDR	**N**egative **D**ifferential **R**esistance
NDC	**N**egative **D**ifferential **C**onductance
AGNR	**A**rmchair **G**raphene **N**ano**R**ibbon
ZGNR	**Z**igzag **G**raphene **N**ano**R**ibbon
RTT	**R**esonant **T**unneling **T**ransistor
TB	**T**ight **B**inding
NEGF	**N**on**E**quilibrium **G**reen's **F**unction
SU	**S**pecial **U**nitary
BZ	**B**rillouin **Z**one
DoS	**D**ensity **o**f **S**tates
GNR	**G**raphene **N**ano**R**ibbon
NEMS	**N**ano**E**lectro**M**echanical **S**ystem**S**
GaAs	**G**allium **A**rsenide
DBRTD	**D**ouble **B**arrier **R**esonant **T**unneling **D**iode

List of Publications

[1] Uniaxial Strain Effect on Graphene Nanoribbon Resonant Tunneling Transistors. Mahmood Akbari, Alireza Baghai-Wadji, Razieh Morad, Prepared to submit for IEEE Trans. on Electron Device journal, 2018.

[2] Strain Effect Consideration on Vertical Heterostructures Based on Graphene and other 2-D Materials. Mahmood Akbari, Alireza Baghai-Wadji, Accepted as an oral presentation at 63th Annual Conference of the South African Institute of Physics, Bloemfontein, South Africa, 25-29 June 2018.

[3] Modeling of A Resonant Tunneling Transistor Under Uniaxial Strain. Accepted as an poster presentation at the International Conference on Multi-Condensate Superconductivity and Superfluidity in Solids and Ultra-Cold Gases, ICTP, Italy, 14-18 May 2018.

List of Symbols

a	distance
E	energy
E_F	Fermi energy
V	potential energy
μ	chemical potential energy
e	electron charge
m	mass
h	Planck constant
$\hbar$	hbar (h/2π)
I	current
T	temperature
v_F	Fermi velocity
H	Hamiltonian
G	Green's function
Γ	broadening function
σ	self energy
$\mathbf{k}$	wave vector
ψ	wave function
T(E)	transmission function
ε	on-site potential energy
ε_0	modulus of strain
t	interaction parameter
η	infinitesimal number
n	electron density
p	hole density
L	length of device
W	width of device
ϑ	the angle with respect to the zigzag direction
N_a	the number of armchair chains
N_z	the number of zigzag chains
f(E)	Fermi-Dirac distribution function
V_g	gate voltage
V_b	bias voltage

Dedicated to my wife Razieh, for all of her love and support.

Chapter 1

Introduction

1.1 Why nonequilibrium Green's function (NEGF)?

Today, the semiconductor industry is a giant market with over $300 billion value achieving tremendous development in decreasing costs of processing, transmission and storage capabilities. One of the fundamentals of semiconductor research is understanding how electronic devices operate. Device physics along with the computational electronics can accurately predict the operational behaviors of an electronic device without any actual fabrication of the device which offers many advantages such as decreasing industrial design cycle time, providing problem diagnostics, gaining insights for future products, and shortening time to market.

The transport behavior of electrons and holes, two basic charge carriers in semiconductor devices, determines the operation of semiconductor electronics. Traditionally, charge carriers are moving through the device driven by electric field act as the semiclassical particles expressing by drift-diffusion equations. For the most simple devices, such as field-effect-transistors, the diffusive carriers transport is adequate and the traditional TCAD tools solve the drift-diffusion equation, current continuity equation, self-consistently with the Poisson's equation in the simulation process. This semiclassical approach can describe properly devices in micrometer and sub-micrometer scale.

In 1965, Gordon Moore noticed that the number of transistors per square inch on integrated circuits had doubled every year leading to the rapid scaling down of semiconductor feature size [1]. Today, the whole device engineering scaled down to the nanoscale range. There is the scaling limit of a few nanometers for the traditional devices based on silicon. So, investigating new devices built from semiconductor

[1] Although, the number of transistors per square inch has since doubled approximately every 18 months. This is used as the current definition of Moore's law.

nanowires, graphene, carbon nanotubes and organic molecules becomes a trend nowadays. Although, the electrical properties of materials are sensitive to the structures in atomistic level due to quantum confinement and a semi-classical picture of the carrier transport is no longer valid in this regime [1]. Examining the semiconductors at atomistic scale is also difficult and challenging experimentally. Therefore, more fundamental physics is required to seek a practical analyzing and simulation approaches for nanomaterial engineers. In this approach, the electrons and holes shall be treated quantum mechanically in atomistic scale rather than continuous one.

When the device dimensions are comparable to the scattering length due to phonons, photons and other electrons (dimensions below 10nm), the modeling approach should capture mechanisms such as quantum tunneling, quantum confinement, and scattering mechanisms. In these cases, even using the basic Schrödinger's equation instead of drift-diffusion equation is not adequate and a more powerful modeling approach is required. The nonequilibrium Green's function (NEGF) approach [1, 2, 3] based on the self-consistent coupling of Schrödinger and Poisson equations, is designed to capture decoherence effects including electron-phonon scattering.

The main features of NEGF can be briefly described as follows:

- The main ingredient of the method is the Green's function, which is a function of two spacetime coordinates and it is useful to calculate physical quantities such as currents and densities, electron addition and removal energies and the total energy of the system.

- In the absence of external fields the NEGF method reduces to the equilibrium Green function method which has had important applications in quantum chemistry.

- The method can be applied to both extended and finite systems.

- The strong external fields (such as electron-electron interactions) can be treated non-perturbatively in the method by considering infinite summations.

- Dissipative processes and memory effects in transport that occur due to electron-electron interactions and coupling of electronic to nuclear vibrations can be clearly diagrammatically analyzed.

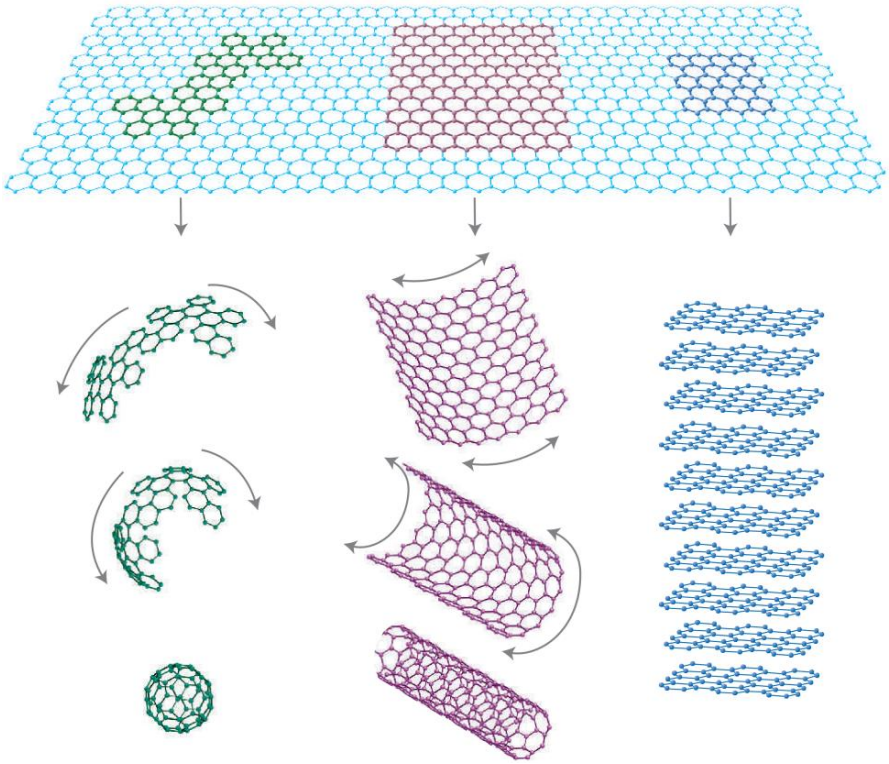

FIGURE 1.1: Graphene is a 2-D building material for carbon materials of all other dimensionalities [8]

In Ref. [4], many practical aspects of implementing the NEGF method are discussed in a rather pedagogical way using the matrix representation of the Green functions of the two terminal structures.

1.2 Graphene based heterestructures

Graphene, a single sheet of carbon atoms tightly packed into a two-dimensional honeycomb lattice has been experimentally discovered in 2005 by Novoselov et.al [5, 6]. The strictly two-dimensional graphene can be seen as the basic building block for the other graphite materials, having different dimensionalities, see Fig. (1.1). It can be wrapped up into 0D buckyballs (the spherical molecule called fullerene which was found in 1985), rolled into 1D nanotubes (produced in 1991), or stacked into 3D graphite. Graphene properties have been theoretically investigated for sixty years now (see Refs. [7]).

In addition to being a purely 2-D crystal of only one atomic layer thickness, graphene has a unique electronic structure which is fundamentally different from other

materials and make this material interesting for both theoreticians, experimentalists, and engineers. One of the most important features of graphene is its linear energy spectrum at low energies. This kind of spectrum is known from high-energy physics where it corresponds to massless particles like neutrino. Consequently, graphene is an experimentally accessible condensed matter system for studying relativistic quantum mechanics. Relativistic-like dispersion relation is responsible for such effects as Klein tunneling -unimpeded penetration of particle through the infinitely large potential barrier [9]. The electrons in graphene propagate at extremely high velocities, only 300 times smaller than the velocity of light acting like Dirac fermions with effective mass. This makes graphene the best known conductor with mobility up to 200,000 $cm^2\,V^{-1}s^{-1}$ at room temperatures. Another fascinating feature of graphene is the minimum conductivity of order $\frac{2e^2}{h}$ at the Dirac (neutrality) point, even though the density of states vanishes at that point. Furthermore, it is known, that the two basic edge shapes, namely zigzag and armchair, lead to different electronic spectra for graphene nanoribbons.

The possible applications of graphene are very extensive. Graphene is considered as the main candidate for a future post-silicon electronics [10] due to its high mobility. Another particular application of graphene is transistors operating at ultrahigh radio frequencies [11]. Due to its high optical transmittance ($\approx 97.7\%$), graphene is proposed to be used as a flexible transparent electrode in touchscreen devices [12]. Also, graphene posses a broad spectral bandwidth and fast response times, which makes this material attractive for optoelectronics and, in particular, phototransistors [13].

Meanwhile, other 2-D materials have also attracted the attention of researchers. One of them, in particular, is hBN, material that possesses a hexagonal structure made up of boron and nitrogen atoms. It's a lattice constant only differs from that of graphene by 1.8% but has huge 4.7 eV band gap due to the boron and nitrogen bonding. The wide band gap means that hBN can function as a good insulator with an atomically flat surface. When hBN is used as a substrate for graphene, the electron mobilities in graphene can easily exceed 10,000 $cm^2\,V^{-1}s^{-1}$ compared to that in graphene on SiO_2 surface which is only 7000 $cm^2\,V^{-1}s^{-1}$. hBN is very resistant both to mechanical manipulation and chemical interactions, so it can be used to encapsulate materials [14]. Additionally, hBN may provide an atomically smooth surface free of dangling bonds and charge traps, which is the ideal material for gate dielectrics [15]. Single-layer hBN, atomically thin, can be used as tunneling barriers for the devices

[16, 17, 18]. hBN substrates leave the band structure of graphene near the Dirac point virtually unperturbed and dramatically improve the mobility of graphene devices [19].

Looking beyond this field, isolated atomic planes can also be reassembled into heterostructures made layer by layer in a precisely chosen sequence to achieve new properties that differ from that of the original materials. Basically, the single layer of two-dimensional materials is constructed with strong covalent bonds in the plane. The few layers of the two-dimensional materials are made up by weak interactions between neighboring two-dimensional layers (in the out of plane direction), namely van der Waals force which is sufficient to allow influences between the layers of 2-D materials. Specific electronic and optical properties that arise in van der Waals heterostructures are convenient for controlling the generation, transportation and recombination of charge carriers, excitons, photons, and are beneficial for the design of unique electronic and photoelectronic devices.

The van der Waals heterostructures provide the chance for engineering a new device at the atomic level, so as to invent the ultra-thin, low-power and flexible device. For example, placing graphene on hBN improves the electronic mobility and if the lattice of graphene is well aligned with that of hBN, self-replicas of the Dirac cones can be observed due to many-body interactions.

1.3 Thesis outline

We begin with an introductory part consisting of Chapters 2 and 3. In Chapter 2, we present the general techniques and computational methods used within this thesis such as Landauer-B üttiker formalism, tight-binding model, and Green's function formalism.

Chapter 3 is dedicated to graphene. In this chapter, we present the widely used single-band, single-electron tight-binding Hamiltonian. The band structure of the graphene is studied and its linear properties are described. Two different types of graphene nanoribbons are introduced briefly. The chapter ends with exploring the effect of uniaxial strain applied on the graphene band structure. In Chapter 4, we theoretically explore the effect of uniaxial strain on the Current-Voltage,$I-V$, characteristic of an AGNR-hBN-AGNR multilayer heterostructure device. In such devices, resonant tunneling occurs if the applied gate voltage align the Dirac points of the top and bottom graphene electrodes. Applying strain on the device deforms the Dirac

points of the graphene (electrodes) so will result in deforming the transport properties of the device. We consider the uniaxial strain applying in the armchair or zigzag direction of both electrodes, such that it changes the intra-layer atomic distances in all layers in the same way. For simplicity, we have ignored the mismatch of the lattice constant between hBN and graphene. By using the tight-binding model and nonequilibrium Green's function formalism the current-voltage characteristic of the device is calculated in the presence of the uniaxial strain.

Finally, Chapter 5 outlines the conclusions of this work and suggestions for future work.

Chapter 2

Techniques

2.1 Landauer-Büttiker formalism

Measurements revealed that the phase coherence length of electrons in graphene is up to several microns long [20]. As a result, electronic transport properties of small graphene devices will rely strongly on quantum coherence effects. The theoretical framework commonly used to describe transport through these so-called mesoscopic devices is the Landauer-Büttiker approach. In this section, we briefly will review the Landauer-Büttiker approach and explain how current can be described in terms of transmission probabilities. The Landauer-Büttiker approach is a well-established method and detailed reviews can be found in Refs. [4, 21, 22, 23, 24].

The standard setup for the theory consists of a mesoscopic device connected to electron reservoirs via leads (See Fig. (2.1)). The reservoirs provide thermalized electrons to occupy the states of the leads. The contacts between leads and reservoirs are considered to be reflectionless, so that electrons coming from the leads can enter the reservoir without suffering reflections, and are thermalized before being re-emitted.

Furthermore, the leads are considered perfect; i.e., they are translational invariant in the propagating direction. The finite width in the transverse direction, however, leads to quantized transverse modes. The wavefunctions in the leads are thus of the form $e^{ikx}\varphi_n(y)$. The transverse modes $\varphi_n(y)$ are referred to as eigenchannels.

The conductance through the sample can now be expressed in terms of transmission probabilities T_n; i.e., the probability for an electron in channel n to be transmitted through the sample. The result is the Landauer formula

$$G = \frac{2e^2}{h} \sum_n T_n(E_F), \tag{2.1}$$

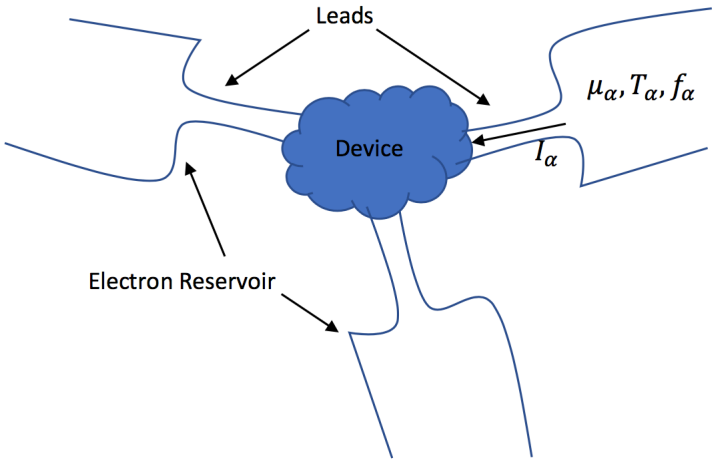

FIGURE 2.1: Set up for Landauer-Büttiker formalism.

where h is the Planck constant, e is the electron charge, E_F is the Fermi energy, and G is the conductance.

We will now give an intuitive derivation of the Landauer formula, for more details see Refs. [4, 24].

The population of the states in the leads is given by the Fermi-Dirac distribution $f(E-\mu_\alpha)$, where μ_α is the chemical potential of the reservoir $\alpha = 1, 2,...$ The electrical current originating from electrons in lead α carried by channel n is given by

$$I_{\alpha nE} = \frac{2e}{L} \sum_k T_n(E)\, v(k)\, f(E-\mu_\alpha), \tag{2.2}$$

where L is the length of the device. The factor 2 accounts for the spin, v(k) is the group velocity of the electrons and $T_n(E)$ gives the transmission probability of channel n at energy E(k) .

The net current is calculated from the difference between the currents originating from the different leads and must be summed over all quantum channels (n). For

example in a system with two leads, the net current is

$$\begin{aligned} I &= \sum_n [I_{1nE} - I_{2nE}] \\ &= \frac{2e}{L} \sum_{n,k} T_n(E)\, v(k)\, (f(E-\mu_1) - f(E-\mu_2)), \end{aligned} \tag{2.3}$$

The current which is positive when flowing from the lead to the device can be written as

$$I = \frac{2e}{h} \sum_n \int dE\, T_n(E)\, (f(E-\mu_1) - f(E-\mu_2)), \tag{2.4}$$

where we converted the sum over the momentum, k into an integral according to

$$\sum_k \rightarrow \frac{L}{2\pi} \int dk, \tag{2.5}$$

and the group velocity is related to the energy as

$$v(k) = \frac{1}{\hbar} \frac{dE}{dk}. \tag{2.6}$$

At low temperatures and for low voltages $eV = \mu_1 - \mu_2$, one can make the following Taylor expansion around the Fermi energy, (E_F)

$$f(E-\mu_1) - f(E-\mu_2) \approx \delta(E-E_F)\,(\mu_1 - \mu_2). \tag{2.7}$$

Substituting the Eq. (2.7) into the Eq. (2.4), the conductance through the system can be obtained as

$$I = \frac{2e}{h} \sum_n T_n(E_F)\, (\mu_1 - \mu_2), \tag{2.8}$$

For the systems with more than two leads, a sum over all leads (indexed by α and β) has to be taken. The total current through lead α is then given by

$$I_\alpha = \frac{2e}{h} \sum_{\beta \neq \alpha} [T_{\beta\alpha}(E_F)\mu_\alpha - T_{\alpha\beta}(E_F)\mu_\beta], \tag{2.9}$$

where $T_{\beta\alpha}(E_F)$ is the total transmission coefficient from lead α to lead β (sum of all transmission probabilities $T_{n\beta\alpha}(E_F)$) . Introducing the electric potential $V_\alpha = \frac{\mu_\alpha}{e}$, this

equation can be rewritten

$$I_\alpha = \sum_\beta [G_{\beta\alpha} V_\alpha - G_{\alpha\beta} V_\beta], \tag{2.10}$$

where the conductances

$$G_{\alpha\beta} = \frac{2e^2}{h} T_{\alpha\beta}(E_F), \tag{2.11}$$

describe the conductance between the different leads.

From a physical point of view, we need to ensure current conservation and gauge invariance. Current conservation implies for a multi-terminal geometry that

$$\sum_\alpha I_\alpha = 0. \tag{2.12}$$

The gauge invariance means that no current arises when all chemical potentials are shifted by the same value. These two physical considerations lead to the following property

$$\sum_\alpha G_{\alpha\beta} = \sum_\beta G_{\alpha\beta} = 0. \tag{2.13}$$

We then rewrite Eq. (2.10) as

$$I_\alpha = \sum_\beta G_{\beta\alpha}(E)[V_\alpha - V_\beta]. \tag{2.14}$$

Consequently, calculating transport properties of a mesoscopic device essentially boils down to determining transmission coefficients [4, 24].

2.2 Tight-binding model

In order to numerically compute physical quantities, such as the transmission coefficients (T(E)) in the Landauer-B üttiker formalism, one needs to represent a numerical model of the problem that is straightforward, simple to use, and sufficiently unrestricted. To this end, a tight-binding representation in one dimension and its extension to a layered structure are considered in this section.

The tight-binding of a system can be calculated by discretizing the Hamiltonian on a lattice. It should be kept in mind that each lattice site is not necessarily corresponding to an atom as in first-principal calculations; instead, a site may serve a

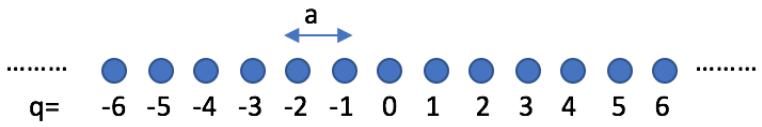

FIGURE 2.2: One dimensional lattice points $x_q = qa$.

region containing many atoms. which is small compared to physically relevant quantities such as Fermi wavelength [25].

2.2.1 Tight-binding in one-dimension

The Hamiltonian for a 1-D system is

$$H = -\frac{\hbar^2}{2m}\frac{d^2}{dx^2} + V(x). \tag{2.15}$$

For a system described by a set of one-dimensional lattice point, Fig. (2.2), with uniform spacing a, Hamiltonian can be written as ($x_q = qa$ and assuming that only nearest neighbor lattice point are coupled)

$$[H\psi(x)]_{x=qa} = [-\frac{\hbar^2}{2m}\frac{d^2\psi}{dx^2}]_{x=qa} + V_q\psi_q\,, \tag{2.16}$$

where q is an integer, V is the electrostatic potential, $\psi_q \rightarrow \psi(x = qa)$ is the wavefunction at point $x = qa$, and $V_q \rightarrow V(x = qa)$.

Using the method of finite difference to approximate the derivative operator [4]

$$\text{First derivative} \rightarrow [\frac{d\psi}{dx}]_{x=(q+\frac{1}{2})a} \longrightarrow \frac{1}{a}[\psi_{q+1} - \psi_q], \tag{2.17}$$

$$\text{Second derivative} \rightarrow [\frac{d^2\psi}{dx^2}]_{x=qa} \longrightarrow \frac{1}{a^2}[\psi_{q-1} - 2\psi_q + \psi_{q+1}]. \tag{2.18}$$

Substituting Eq. (2.17), Eq. (2.18) in Eq. (2.16), we could obtain

$$[H\psi(x)]_{x=qa} = -\frac{\hbar^2}{2ma^2}\psi_{q-1} + \frac{\hbar^2}{ma^2}\psi_q - \frac{\hbar^2}{2ma^2}\psi_{q+1} + V_q\psi_q. \tag{2.19}$$

Introducing $t \equiv \frac{\hbar^2}{2ma^2}$ as the hopping parameter and $\varepsilon \equiv V_q + 2t = V_q + \frac{\hbar^2}{ma^2}$ as the onsite energy, then Hamiltonian can be written as

$$[H\psi(x)]_{x=qa} = -t\psi_{q-1} + \varepsilon\psi_q - t\psi_{q+1}. \tag{2.20}$$

Therefore by substituting Eq. (2.20) in the Schrödinger's equation, we have

$$(E-H)\psi = 0 \rightarrow \begin{pmatrix} \bullet & \bullet & \bullet & & & & & & \\ & \bullet & \bullet & \bullet & & & & & \\ & & -t & E-\varepsilon & -t & & & & \\ & & & & -t & E-\varepsilon & -t & & \\ & & & & & -t & E-\varepsilon & -t & \\ & & & & & & \bullet & \bullet & \bullet \\ & & & & & & & \bullet & \bullet & \bullet \end{pmatrix} \begin{pmatrix} \bullet \\ \bullet \\ \Psi_{q-1} \\ \Psi_q \\ \Psi_{q+1} \\ \bullet \\ \bullet \end{pmatrix} = 0\,. \tag{2.21}$$

Here, ε and t represent the onsite potential energy and interaction between nearest neighbor lattice points q and $q-1$ or $q+1$ respectively.

By using Bloch's theorem [1], the solution of Eq. (2.21) can be verified as

$$E(k) = \varepsilon + 2\,t\,\cos(ka), \tag{2.22}$$

$$\Psi_q(k) = e^{i\,kqa}. \tag{2.23}$$

Finally, we write a general nearest neighbor tight binding Hamiltonian by [1],

$$-t_{q,q-1}\psi_{q-1} + (E-\varepsilon_q)\psi_q - t_{q,q+1}\psi_{q+1} = 0. \tag{2.24}$$

2.2.2 Tight-binding for layered structures

A layer can be considered as a planar arrangement of lattice points in a certain desirable configuration. As an example consider the structure in Fig. (2.3). Here, layer q consists of three lattice points a, b and c. The form of the Hamiltonian remains the same as in Eq. (2.24) except the fact that ε_q and $t_{q,q+1}$ or $t_{q,q-1}$ must now be replaced by (3×3) matrices and ψ_q by a (3×1) vector as given below

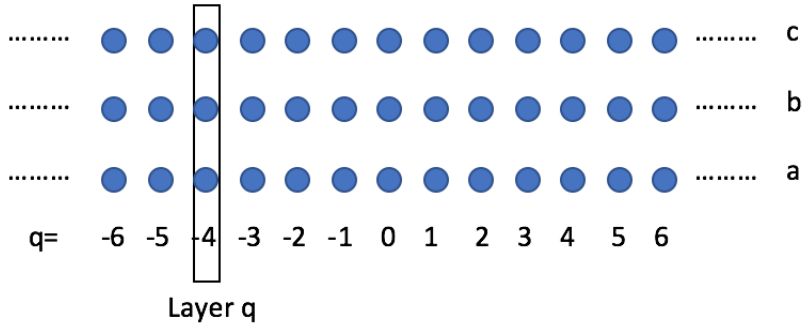

FIGURE 2.3: A generic layered structure along with lattice points.

$$\varepsilon_q \rightarrow \begin{pmatrix} \varepsilon_q^a & \varepsilon_q^{ab} & \varepsilon_q^{ac} \\ \varepsilon_q^{ba} & \varepsilon_q^b & \varepsilon_q^{bc} \\ \varepsilon_q^{ca} & \varepsilon_q^{cb} & \varepsilon_q^c \end{pmatrix}, \tag{2.25}$$

$$t_{q,q+1} \rightarrow \begin{pmatrix} t_{q,q+1}^a & t_{q,q+1}^{ab} & t_{q,q+1}^{ac} \\ t_{q,q+1}^{ba} & t_{q,q+1}^b & t_{q,q+1}^{bc} \\ t_{q,q+1}^{ca} & t_{q,q+1}^{cb} & t_{q,q+1q}^c \end{pmatrix}, \tag{2.26}$$

$$\psi_q \rightarrow \begin{pmatrix} \psi_q^a \\ \psi_q^b \\ \psi_q^c \end{pmatrix}, \tag{2.27}$$

where ε_q^a, ε_q^b and ε_q^c are the diagonal elements of the Hamiltonian at grid points a, b and c ,respectively, in layer q. Furthermore, the entries $t_{q,p}^{ij}$ represent interaction between the lattice point i in layer q and the lattice point j in layer p, while $i, j \in a, b, c$ [1].

2.3 Green's function formalism

Assuming a tight-binding model, a numerical representation of the system was established in the previous section. We still need a mathematical formalism in which various physical characteristics can be calculated. To this end, Green's functions offer themselves as a precious. One of the advantages is the relative ease with which they can be calculated compared with the direct numerical solution of the Schr ödinger's equation. In particular, a highly efficient recursive approach is available to obtain the Green's functions which are essential for the evaluation of the transmission coefficients in the Landauer-B üttiker formalise [4, 21]. This approach is discussed in detail in this section.

2.3.1 Green's function: the principle

In quantum physics, $\hat{G}(E)$ as the single-particle Green's function of a system which is described by a hamiltonian $\hat{H}$ can be defined as the solution for the operator equation [4, 21, 26]

$$[E - \hat{H}]\,\hat{G}(E) = \hat{1}. \tag{2.28}$$

A formal solution for this equation is given by $\hat{G}(E) = (E - \hat{H})^{-1}$. However, this solution is not well-defined for values of E corresponding to the eigenvalues of the Hamiltonian [25]. The Eq. (2.28) can be written in the position space as

$$[E - \hat{H}(\mathbf{r})]\,G(\mathbf{r}, \mathbf{r'}, E) = \delta(\mathbf{r} - \mathbf{r'}), \tag{2.29}$$

where $G(\mathbf{r}, \mathbf{r'}, E) =< \mathbf{r}\,|\hat{G}(E)|\,\mathbf{r'} >$ is called the Green's function of the system which can be considered as a wavefunction at position r responding to a Dirac delta function excitation localized at r′ . However, we also take G into account as the source for such excitation. In fact, both solutions satisfy Eq. (2.28), but they correspond to various boundary conditions: if H is the Hamiltonian for a particle which moves in a constant potential, the first solution corresponds to an out-going wave from the point r′, whereas the second one is an incoming wave. To include such boundary conditions into a unique definition for the Green's function, we may add an infinitesimal

imaginary variable into the energy, leading to

$$G^{\pm}(\mathbf{r}, \mathbf{r'}, E) \equiv \lim_{\eta \to 0^+} G(\mathbf{r}, \mathbf{r'}, E \pm i\eta), \tag{2.30}$$

where the functions $G^{\pm}$ satisfy the equation

$$[E \pm i\eta) - H(r)]\, G^{\pm}(\mathbf{r}, \mathbf{r'}, E) = \delta(\mathbf{r} - \mathbf{r'}). \tag{2.31}$$

The functions G^{+} and G^{-} are called retarded and advanced Green's function, respectively. In the above example, the retarded Green's function corresponds to the outgoing wave and the advanced Green's function to the incoming one. Actually, Fourier transforming the functions $G^{\pm}$ to the time domain by a closed contour integral in the complex plane, the resulting functions relate to the casual and anti-casual solutions [27].

Consequently, the retarded and advanced Green's function for any value of E are defined by the relation

$$\hat{G}^{\pm}(E) \equiv \lim_{\eta \to 0^+} \frac{1}{E \pm i\eta - \hat{H}}. \tag{2.32}$$

For brevity of notation the hat in $\hat{G}$, will be omitted in the next subsection. From the context, it is obvious that Green's function stands for a function, a matrix in the discrete system, or an operator. Besides, we will drop the subscript ± which distinguishes retarded from advanced Green's function. There, G will denote a retarded Green's function. From Eq. (2.32), it is evident that the advanced Green's function corresponds to the Hermitian conjugate of the retarded Green's function, meaning that $G^{+} = (G^{-})^{\dagger} \equiv G^{\dagger}$ [25].

2.3.2 Transmission coefficients and the Green's function

In the Landauer-Büttiker formalism discussed in Section 1, a central device is connected to perfect leads, and we express I-V characteristics in terms of the transmission coefficients between the leads. The transmission coefficients are related to the Green's function of the device. In a tight-binding representation [28, 29], the transmission coefficient between the leads p and q can be written as

$$T_{pq} = \mathrm{trace}[\Gamma_p\, G_{pq}\, \Gamma_q\, G_{pq}^{\dagger}], \tag{2.33}$$

where G_{pq} is a submatrix of the whole system's Green's function: it includes only the elements of Green's function between the sites in the central device that is connected to the leads p and q. The matrix Γ_p in Eq. (2.33) is the so-called broadening function of the lead p and it can be expressed in terms of the self-energy Σ_p of the lead.

$$\Gamma_p = i(\Sigma_p - \Sigma_p^\dagger), \tag{2.34}$$

As will be clear momentarily the self-energy is relevant to the elements of G between sites at the surface of the leads [25]. Further details will be provided in the following subsection.

2.3.3 Lattice Green's function approach

Judged superficially one might have the impression that all is necessary has already been stated about Green's function method: one just obtains the tight-binding Hamiltonian of the system under consideration, writes it down in the form of a matrix, and calculates the Green's function by using the inversion of matrix $E + i\eta - H$. Hence, physical quantities such as transmission coefficients of the Landauer - Büttiker formalism can be calculated by expressing them in terms of the Green's function.

However, since we are dealing with an open system (semi-infinite leads connected to the device) the tight-binding Hamiltonian matrix which describes the whole system is infinite dimensional and thus cannot be inverted numerically. Thus, even if we are able to meaningfully truncate the Hamiltonian matrix, inverting it directly would be numerically highly expensive. We will discuss these and related issues in this section. In our discussion, we will use the notation $G_{nn'}$ to indicate a submatrix of the whole Green's function matrix G. Here, $G_{nn'}$ describes the connection between the sites of columns n and n′; i.e.,

$$< m|G_{nn'}(E)|m' >= G_{nm,n'm'}(E) =< nm|G(E)|n'm' >, \tag{2.35}$$

where (m, n) label the sites in the tight-binding lattice [4, 21].

2.3.4 Semi-infinite leads: self-energy description

In the Landauer-B üttiker formalism, the system consist of a central device which is connected to the leads, Fig. (2.1). Consequently, we subdivide its Hamiltonian as

follows

$$H = H_C + \sum_i (H_l^i + V_{ld}^i + V_{dl}^i), \tag{2.36}$$

where H_C is the Hamiltonian of the central device and H_l^i is the Hamiltonian of lead i. V_{ld}^i describes the coupling between lead (l) and device (d). Numerically, it is impossible to obtain the Green's function by a direct inversion $[E + i\eta - H]^{-1}$, since each H_l^i have infinite dimension.

The standard approach to solve this problem accounts for the influence of the lead by a self-energy term. In this approach, the central device including the effects of the leads can be described by a finite dimensional Hamiltonian [21, 29]

$$\mathcal{H}_C = H_C + \sum_i \Sigma^i, \tag{2.37}$$

where Σ^i is the retarded self-energy of the lead i defined as

$$\Sigma^i = V_{dl}^i \, g_l^i \, V_{ld}^i. \tag{2.38}$$

Here, g_l^i is the Green's function of the isolated semi-infinite lead: $g_l^i = [E + i\eta - H_l^i]^{-1}$.

At first sight, it seems that the problem has just been shifted, since for the calculation of g_l^i we still require the inversion of infinite dimensional Hamiltonian H_l^i. However, based on the fact that a nearest-neighbor tight-binding model is used, the matrices V_{dl}^i and V_{ld}^i have nonzero elements only when the sites on the surface of the leads and their neighbor sites in the device are considered. This reflects that only the surface Green's function $(g_l^i)_{11}$ is required in Eq. (2.38), see Fig. (2.4). The key point is that various methods are available in order to calculate the associated Green's function: Major methods utilized in this work will be discussed in Chapter 4.

The Hamiltonian of the central device includes N lattice sites, $\mathcal{H}_C$ can be represented by a $2N \times 2N$ matrix (the factor 2 accounts for the spin). Thus, the corresponding Green's function can be obtained from the following expression

$$G_C = [E + i\eta - \mathcal{H}_C]^{-1}. \tag{2.39}$$

However, the number of floating point operations which are essential for inverting a $2N \times 2N$ matrix scales as $(2N)^3$, and thus the inversion in Eq. (2.39) causes heavy constraints on the numerically reachable system size. There is an efficient recursive

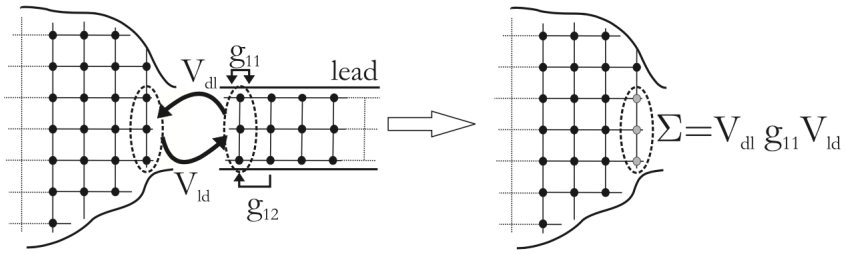

FIGURE 2.4: The influence of an lead can be described by adding its self-energy to the Hamiltonian of the device [25].

method to obtain G_C, which is presented in the next subsection.

2.3.5 Recursive method: standard approach

Recursive methods which are the most useful methods to evaluate the Green's function are based on the division of the device in smaller parts. These parts are glued together by using Dyson's equation [27]

$$G = g + g\,V\,G, \tag{2.40}$$

which allows us to relate the Green's function g of two disconnected subsystems to the Green's function G of the connected system. Here, V denotes the hopping between the subsystems.

Before we start a detailed discussion on the recursive Green's function method, we will illustrate the use of Dyson's equation by an example, shown in Fig. (2.5). Consider a system composed of two parts with the known isolated Green's function g. We would like to obtain G_{N1}, which is the elements of the Green's function between the first and the last column of the coupled device. This can be done by projecting Eq. (2.40) between columns N and 1

$$G_{N1} =< N|G|1 > \tag{2.41}$$

$$=< N|g|1 > + \sum_{|\alpha>,|\beta>} < N|g|\alpha >< \alpha|V|\beta >< \beta|G|1 > \tag{2.42}$$

$$=< N|g|n >< n|V|n+1 >< n+1|G|1 > \tag{2.43}$$

$$= g_{Nn}\,V_{n,n+1}\,G_{n+1,1}\,. \tag{2.44}$$

In obtaining the Eq. (2.43), we have used the fact that the hopping matrix V

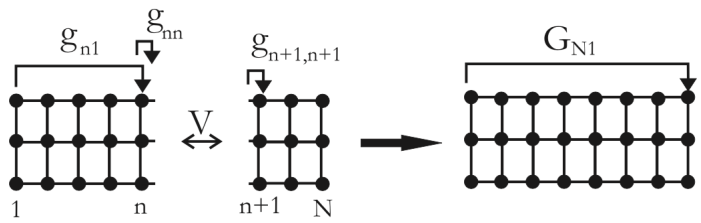

FIGURE 2.5: Connecting two isolated sections with Dyson's equation to evaluate Green's functions for the connected system [25].

between disconnected systems has only nonzero elements between columns n and n+1 in the nearest-neighbor tight-binding model. Furthermore, we have $g_{N1} = 0$, because g is only for the disconnected system. Now, we proceed to find the unknown $G_{n+1,1}$ in Eq. (2.44) by taking again the appropriate matrix elements of Dyson's equation. We follow this procedure until we find a closed set of equations as

$$G_{n+1,1} = g_{n+1,n+1}\, V_{n+1,n}\, G_{n1} \tag{2.45}$$

$$G_{n1} = g_{n1} + g_{nn}\, V_{n,n+1}\, G_{n+1,1}. \tag{2.46}$$

By using the above equations, we obtain

$$G_{n+1,1} = [1 - g_{n+1,n+1}\, V_{n+1,n}\, g_{nn}\, V_{n,n+1}]^{-1} g_{n+1,n+1}\, V_{n+1,n}\, G_{n1}. \tag{2.47}$$

Substituting this relation in Eq. (2.44), we will obtain an equation for G_{N1} in terms of Green's functions for the isolated parts, which was our original objective.

Now, we have sufficient technical knowledge to proceed to the recursive Green's function method [21, 30]. In the following, we will consider a central device which is discretized on a rectangular tight-binding lattice composed of M rows and N columns Fig. (2.6) .The influence of the leads which are connected to this central device will be explained by their self-energy, which give rise to a finite dimensional Hamiltonian $\mathcal{H}_C$ for the device, as explained in the previous subsection. We will assume that all leads are connected at the right and left edges of the central device so that their self-energies only affect sites of the first and last columns of the device (illustrated in gray in the figures). If this is not the case, self-energy terms can introduce efficient hopping between lattice columns which are not the nearest neighbors, and under this condition, the recursive method cannot be used. For instance in the above example,

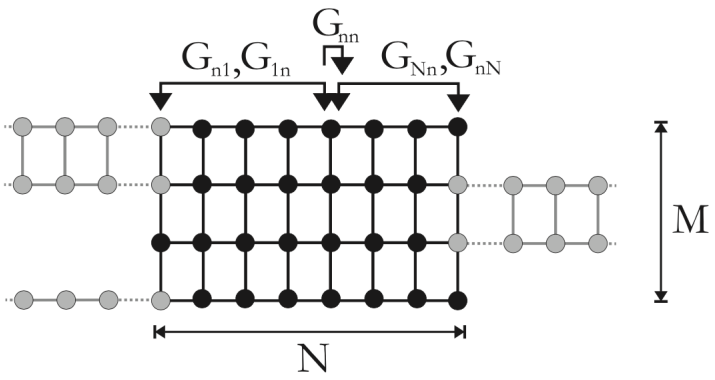

FIGURE 2.6: Subset of device Green's functions required to calculate the desired physical quantities. The leads connected to the central device are shown in gray [25].

if V has nonzero contributions between columns different from n and n + 1, then the Eq. (2.43) is much more complicated.

We write a wide range of physical quantities of such a system in terms of the small subset of Green's function matrices. In Fig. (2.6), the elements of the Green's function between the first or last column of the device and any intermediate one are displayed. The first step to calculate these quantities consists of separating the device in isolated columns and calculating the Green's function G_{ii}^{isol} for all of the isolated columns $i = 1, 2, ..., N$ by performing a direct inversion

$$G_{i,i}^{isol} = [E + i\eta - < i|\mathcal{H}_C|i >]^{-1}, \tag{2.48}$$

where $< i|\mathcal{H}_C|i >$ is the tight-binding Hamiltonian of column i. This step is shown in Fig. (2.7a). The next step is assembling the whole device gluing together one by one, as depicted in Fig. (2.7b). Assume that we already have the Green's functions G_{n1}^{L}, G_{1n}^{L}, G_{nn}^{L} of a strip of n columns which are connected together. We add the superscript L to indicate the fact that they only provide a section of the device (namely a strip of n columns), not the total device. We then obtain the Green's functions $G_{n+1,1}^{L}$, $G_{1,n+1}^{L}$ and $G_{n+1,n+1}^{L}$ for a part of n+1 columns by projecting Dyson's Equation; i.e., Eq. (2.40) between the appropriate columns, in the same way as performed in

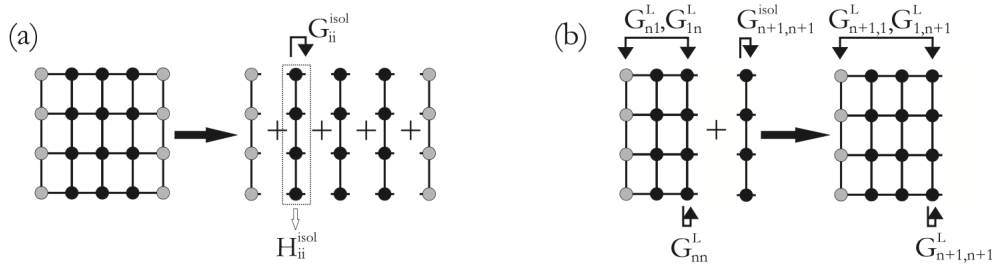

FIGURE 2.7: Standard recursive method. (a) The device is separated into its isolated columns and (b) Dyson's equation is applied to glue them in order to obtain the relevant Green's function [25].

the simple example explained above. Here, we will only write the final result

$$G^{L}_{n+1,n+1} = [1 - G^{isol}_{n+1,n+1}\, V_{n+1,n}\, G^{L}_{n,n}\, V_{n,n+1}]^{-1} G^{isol}_{n+1,n+1}, \tag{2.49}$$

$$G^{L}_{n+1,1} = G^{L}_{n+1,n+1}\, V_{n+1,n}\, G^{L}_{n,1}, \tag{2.50}$$

$$G^{L}_{1,n+1} = G^{L}_{1,n}\, V_{n,n+1}\, G^{L}_{n+1,n+1}. \tag{2.51}$$

When we start from the leftmost column n = 1 with $G^{L}_{1,1} = G^{isol}_{1,1}$, we continue in this direction (left to right) through the total sample and calculate $G^{L}_{n,1}$, $G^{L}_{1,n}$ and $G^{L}_{n,n}$ for all n. After connecting the last column, we obtain the Green's function submatrices G^{L}_{N1}, G_{N1} and G^{L}_{1N}, G_{1N} which connect the first and last column of the device. These steps finalize the standard recursive Green's function approach, and they suffice to describe transport quantities in the Landauer-Büttiker formalism [21, 30]. In fact, all leads are attached to the right and left edge of the system, and the Eq. (2.33) expresses the transmission coefficient in terms of the Green's function G_{N1} or G_{1N} [31, 32].

By reviewing the Eqs. (2.48) - (2.51), we observe that the computational operations which are essential in obtaining the final Green's functions are either products or inversions of $(2M \times 2M)$ matrices, and the total amount of these operations is proportional to the length N of the system. Since the computational effort for a matrix inversion or product scales as $(2M)^3$ in the number of floating point operations, the total numerical effort for the recursive method scales as M^3N for the large systems $(N \gg 1)$. Consequently, we gain a factor N^2 in efficiency compared with the direct inversion of the whole $2MN \times 2MN$ matrix $E + i\eta - \mathcal{H}_C$, which scaled as M^3N^3. The price one has to pay for increased efficiency is that one can only calculate a smaller

subset of Green's functions (direct inversion will give us $G_{nn'}$ for all n and n′).

Recursive method: an extension

The standard recursive method has been extended with the aim of obtaining the additional Green's functions $G_{Nn}, G_{nN}, G_{n1}, G_{1n}$ and G_{nn} depicted in Fig. (2.6). After we have completed the standard method, we begin from the Green's functions of the isolated columns, and glue them together as we did previously on the basis of Dyson's equation, but now we start from the right column. This procedure is shown in Fig. (2.8a). The Green's functions that we calculate with every step are $G^R_{Nn}, G^R_{nN}, G^R_{nn}$. They can be obtained in terms of the $G^R_{N,n+1}, G^R_{n+1,n+1}$ and $G^R_{n+1,N}$ as follows

$$G^R_{nn} = [1 - G^{isol}_{nn} V_{n,n+1} G^R_{n+1,n+1} V_{n+1,n}]^{-1} G^{isol}_{nn}, \tag{2.52}$$

$$G^R_{Nn} = G^R_{N,n+1} V_{n+1,n} G^R_{nn}, \tag{2.53}$$

$$G^R_{nN} = G^R_{nn} V_{n,n+1} G^R_{n+1,N}, \tag{2.54}$$

starting from $G^R_{NN} = G^{isol}_{NN}$, we are able to obtain G^R_{Nn}, G^R_{nN} and G^R_{nn} for all $n = N-1, N-2, ..., 1$. Again, we have added superscript R to indicate that these are Green's function for a subsection of the whole device.

The last step is composed of attaching the calculated Green's functions G^L and G^R in pairs as shown in Fig. (2.8b). We attach a strip of connected columns 1 to n (known Green's function G^L_{n1} and G^L_{nn}) to the strip of columns n + 1 to N (known Green's function $G^R_{N,n+1}$ and $G^R_{n+1,n+1}$), and this can be done for all $n = 1, ..., N$. Again, projecting Dyson's equation results in the relevant mathematical relations

$$G_{n1} = [1 - G^L_{nn} V_{n,n+1} G^R_{n+1,n+1} V_{n+1,n}]^{-1} G^L_{n1}, \tag{2.55}$$

$$G_{1n} = G^L_{1n} + G^L_{1n} V_{n,n+1} G^R_{n+1,n+1} V_{n+1,n} G_{nn}, \tag{2.56}$$

$$G_{nn} = [1 - G^L_{nn} V_{n,n+1} G^R_{n+1,n+1} V_{n+1,n}]^{-1} G^L_{nn}, \tag{2.57}$$

$$G_{Nn} = G^R_{N,n+1} V_{n+1,n} G_{nn}, \tag{2.58}$$

$$G_{nN} = G_{nn} V_{n,n+1} G^R_{n+1,N}. \tag{2.59}$$

These additional steps include several matrix multiplications and inversions which scales linearly in N. The numerical computation of the additional Green's functions with the extended recursive approach has the same efficiency as the standard method. Access to these additional Green's functions allows obtaining important quantities

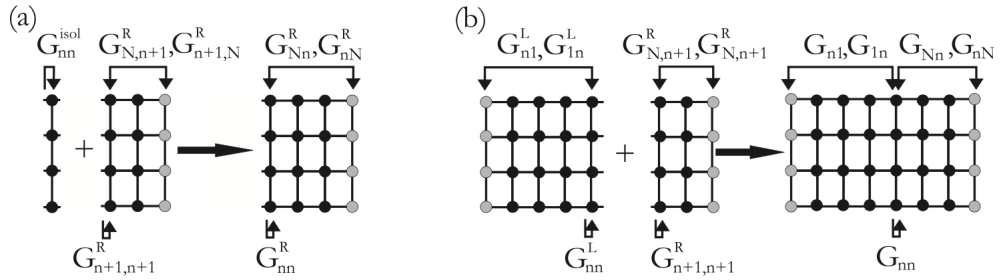

FIGURE 2.8: Extension of the standard recursive method. (a) The isolated columns are glued together, but now we begin from the right side. (b) The last step is adding these strips of columns to the ones calculated in Fig. (2.7), [25].

such as the current density distribution. Furthermore, particular quantities can be calculated with the higher efficiency using these additional Green's functions than just the standard Green's function G_{N1} and G_{1N} [25].

Chapter 3

Graphene

3.1 Introduction

Graphene, a single layer of carbon atoms arranged in hexagonal cells, has emerged as a fascinating system for fundamental studies in condensed matter physics, as well as a promising candidate material for future applications in nano-electronics and molecular devices [5, 6]. Graphene has unique electronic properties due to its peculiar band structure: it is an interesting mix of a semiconductor (zero density of states) and a metal (gaplessness) and has properties of soft matter. Since the spectrum has a conical shape near the Fermi energy, electrons effectively behave as ultra-relativistic particles as they move through the carbon lattice ($v_F \sim c/300$). Therefore, graphene's properties are very different from the usual materials and semiconductors.

On the other hand, these properties can be easily modified with the application of electric and magnetic fields, addition of layers, control of its geometry, and chemical doping. Moreover, graphene can be directly and relatively easily probed by various scanning probe techniques from mesoscopic down to atomic scales. This makes graphene one of the most flexible systems in condensed matter research. Besides the unusual basic properties, graphene has the potential for a large number of applications [6], from chemical sensors [33, 34] to transistors [35] .

3.2 Graphene's honeycomb lattice

Graphene is a truly 2-D crystal made of carbon atoms arranged in a hexagonal lattice. Carbon has 6 electrons in the configuration $1s^2\,2s^2\,2p^2$. The 2 electrons which fill the inner shell 1s, are irrelevant for chemical reactions. The 4 electrons which fill the 2s and 2p orbitals are in the ground state. However, in the presence of other atoms such as H, O, or C, one electron from 2s orbital excites and fills the third 2p orbital. So,

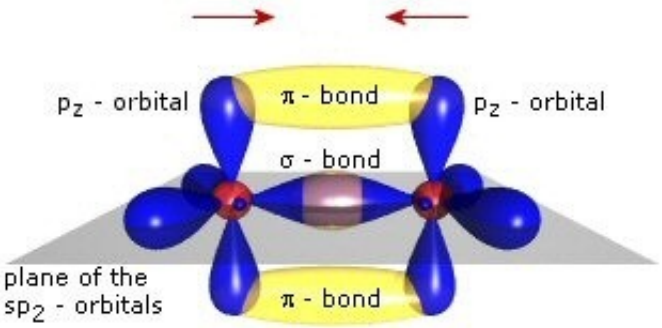

FIGURE 3.1: Schematic view of the sp^2 hybridization. The orbitals form angles of 120° in the horizontal xy-plane. The remaining unhybridized $2p_z$ orbital is perpendicular to the plane.

the carbon atoms form covalent σ bonds between each other which is energetically favorable. This excitation is called sp^2 hybridization, see Fig. (3.1). The remained electron fills the unhybridized $2p_z$ orbital which is perpendicular to the plane and yields the π bonds. Since each carbon atom contributes one electron to the π-band, this π-band is half-filled for clean graphene. These electrons are responsible for the electronic properties at low energies, while the electrons participating in the strong σ bonds form energy bands far away from the Fermi energy.

The graphene's honeycomb lattice is not a Bravais lattice, rather it consists of two sublattices A and B, as depicted in Fig. (3.2). Thus, we may consider it as a triangular Bravais lattice with a two-atom basis (A and B). The distance between nearest neighbor carbon atoms is $a_{CC} = 0.142$ nm. The triangular Bravais lattice is spanned by the basis vector

$$\mathbf{a_1} = a(1,0)\,, \qquad \mathbf{a_2} = \frac{a}{2}(1,\sqrt{3}). \tag{3.1}$$

The reciprocal lattice, Fig. (3.2) is spanned by the vectors

$$\mathbf{b_1} = \frac{2\pi}{a}(1,\frac{-1}{\sqrt{3}})\,, \qquad \mathbf{b_2} = \frac{4\pi}{\sqrt{3}a}(0,1). \tag{3.2}$$

The direct and reciprocal lattice vectors satisfy the following relation

$$\mathbf{a_i}.\mathbf{b_j} = 2\pi\,\delta_{i,j} \quad , \; (i,j=1,2)\,. \tag{3.3}$$

The first Brillouin zone represents a set of inequivalent points in the reciprocal

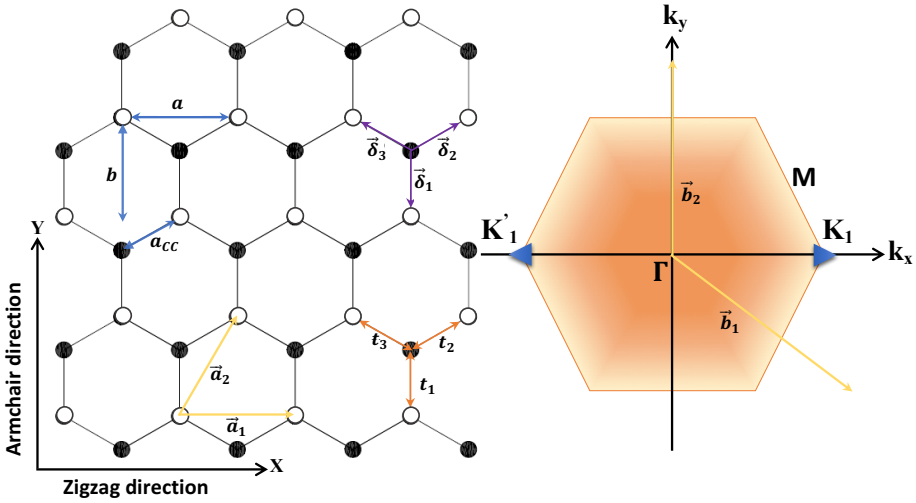

FIGURE 3.2: Left: Graphene lattice. Lengths along the x and y directions are measured in units of a = $\sqrt{3}\,a_{CC}$ and b = $\sqrt{3}/2\,a$, respectively. The distance between Carbon atoms is a_{CC} = 0.142 nanometers. The vectors $\mathbf{a}_1$ and $\mathbf{a}_2$ are basis vectors of the triangular Bravais lattice. The vectors $\boldsymbol{\delta}_1$, $\boldsymbol{\delta}_2$, and $\boldsymbol{\delta}_3$ connect a site on the A sublattice to the nearest neighbors on the B sublattice with hopping parameters denoted by t_1, t_2 and t_3. Right: First Brillouin zone (BZ). Reciprocal lattice primitive vectors are $\mathbf{b}_1$ and $\mathbf{b}_2$. $\mathbf{K_1}$ = $(4\pi/3a, 0)$ and $\mathbf{K'_1}$ = $(-4\pi/3a, 0)$ are two inequivalent Dirac points.

space. Inequivalent points refer to the points which may not be connected to one another by a reciprocal lattice vector. Two inequivalent points K_1 and K'_1 are represented by the vectors

$$\mathbf{K_1} = (\frac{4\pi}{3\,a}, 0)\,, \qquad \mathbf{K'_1} = (-\frac{4\pi}{3\,a}, 0). \tag{3.4}$$

At these points, the conduction and valence bands meet, as discussed in the next section.

3.3 Band structure of graphene

Since the energy regions accessible experimentally are close to the Fermi energy, we are interested in the energy bands of π electrons which were calculated using the tight-binding model for the first time [7]. The p_z-orbitals of different atoms are only weakly overlapping, thus rendering a description in terms of the "tight-binding approximation" is appropriate. In the Hamiltonian of the tight-binding model in the nearest neighbor approximation, the coupling of electrons that are more than one atom apart is neglected.

Generally, the band structure of a solid is obtained by solving the time-independent Schrödinger's equation

$$\hat{H}\psi(k, \mathbf{r}) = E(k)\psi(k, \mathbf{r}), \tag{3.5}$$

where $\hat{H}$ is the Hamiltonian operator that operates on the wavefunction ψ to produce the allowed energies E(k). The Hamiltonian for an independent electron in a periodic solid is given by

$$\hat{H} = \frac{\hbar^2}{2\,m}\nabla^2 + \sum_{i}^{N} U(\mathbf{r} - \mathbf{R_i}), \tag{3.6}$$

where the former term in the Hamiltonian is the kinetic energy operator and the latter term is the potential energy operator. $\mathbf{R_i}$ is the i-th Bravais lattice vector, N is the number of primitive unit cells, and $U(\mathbf{r} - \mathbf{R_i})$ is the potential energy contribution from the atom-centered in the i-th primitive unit cell.

The acceptable wavefunctions in a crystalline solid must satisfy Bloch's theorem,

$$\psi(\mathbf{r} + \mathbf{R}) = e^{ik.\mathbf{R}}\,\psi(\mathbf{r}), \tag{3.7}$$

where $\mathbf{R}$ is a Bravais lattice vector. In addition, periodic boundary conditions are imposed on the wave functions to determine the allowed values of the wave-vector that leads to running waves

$$\psi(\mathbf{r}) = \psi(\mathbf{r} + \mathbf{S}) = e^{ik.\mathbf{S}}\,\psi(\mathbf{r}), \rightarrow \quad e^{ik.\mathbf{S}} = 1, \tag{3.8}$$

where $\mathbf{S}$ is the size vector whose lengths in all the coordinates of space are the spatial dimensions of the lattice.

For graphene, with two sites A and B, the tight-binding wavefunction is a weighted sum of the two sublattice Bloch functions

$$\psi(k, \mathbf{r}) = C_A(k)\tilde{P}_z^A(k, \mathbf{r}) + C_B(k)\tilde{P}_z^B(k, \mathbf{r}), \tag{3.9}$$

where the subscripts A and B denote the two different atoms in the graphene unit cell, see Fig. (3.2). The weights (C_A, C_B) are in general, functions of wavenumber k but independent of $\mathbf{r}$. The ansatz expresses the Bloch functions as a linear combination

of the atomic orbitals or wave-functions which are assumed to be known

$$\tilde{P}_z^A(k,\mathbf{r}) = \frac{1}{\sqrt{N}} \sum_j^N e^{ik.\mathbf{R_{A_j}}}\, P_z(\mathbf{r}-\mathbf{R_{A_j}})\,, \tag{3.10}$$

$$\tilde{P}_z^B(k,\mathbf{r}) = \frac{1}{\sqrt{N}} \sum_j^N e^{ik.\mathbf{R_{B_j}}}\, P_z(\mathbf{r}-\mathbf{R_{B_j}})\,, \tag{3.11}$$

where N is the number of unit cells in the lattice and $\mathbf{R_A}$ $\mathbf{(R_B)}$ are the Bravais lattice vectors identifying the locations of all type A (B) atoms in the graphene lattice. The atomic orbitals P_z belong to a class of functions known as Wannier functions, which are orthonormal and sufficiently localized such that, at distances increasingly removed from the center point R_j , the functions decay to zero very rapidly. The sum is over all the lattice vectors, and $1/\sqrt{N}$ serves as the normalization constant for the Bloch functions in the strict limit when the Wannier function in cell j has zero overlaps with neighboring Wannier functions. [1] Therefore,

$$< \tilde{P}_z^{\alpha}(k)|\tilde{P}_z^{\beta}(k') >= \delta_{k,k'}\,\delta_{\alpha,\beta}. \tag{3.12}$$

Substituting the Eq. (3.9) into Eq. (3.5) we obtain

$$C_A(k)\,\hat{H}|\tilde{P}_z^A(k) > + C_B(k)\hat{H}|\tilde{P}_z^B(k) >= E(C_A(k)\,|\tilde{P}_z^A(k) > + C_B(k)|\tilde{P}_z^B(k) >). \tag{3.13}$$

Multiplying by the $< \tilde{P}_z^A(k)|$, and separately by the $< \tilde{P}_z^B(k)|$, generates two separate equations

$$C_A(k)\ < \tilde{P}_z^A(k)|\hat{H}|\tilde{P}_z^A(k) > + C_B(k) < \tilde{P}_z^A(k)|\hat{H}|\tilde{P}_z^B(k) >= E\,C_A(k) \quad , \tag{3.14}$$

$$C_B(k)\ < \tilde{P}_z^B(k)|\hat{H}|\tilde{P}_z^A(k) > + C_B(k) < \tilde{P}_z^B(k)|\hat{H}|\tilde{P}_z^B(k) >= E\,C_B(k) \quad . \tag{3.15}$$

We define,

$$H_{AB} = < \tilde{P}^A|\hat{H}|\tilde{P}^B >= \frac{1}{N_{cell}} \sum_{i,j} e^{ik.(\mathbf{R_j}-\mathbf{R_i})} < P^A(\mathbf{R_i})|\hat{H}|P^B(\mathbf{R_j}) > \quad , \tag{3.16}$$

$$H_{AA} = < \tilde{P}^A|\hat{H}|\tilde{P}^A >= \frac{1}{N_{cell}} \sum_{i,j} e^{ik.(\mathbf{R_j}-\mathbf{R_i})} < P^A(\mathbf{R_i})|\hat{H}|P^A(\mathbf{R_j}) >, \tag{3.17}$$

[1] The Bloch functions are not exact wavefunctions because they are not normalized when we include some finite overlap. However, they are the best tight-binding ansatz we have that is not overly complicated and is still suitable for analysis with useful accuracy.

where for simplicity we ignore the subscript z in our notation. Since the two atoms in the unit cell are identical, the overlap between all type-A atoms must be the same as the overlap between all type-B atoms

$$H_{AA} = H_{BB}, \quad H^{*}_{BA} = H_{AB}. \tag{3.18}$$

Then, the Schrödinger's equation can be written as a matrix equation

$$\begin{pmatrix} H_{AA} & H_{AB} \\ H_{BA} & H_{BB} \end{pmatrix} \begin{pmatrix} C_A \\ C_B \end{pmatrix} = E(k) \begin{pmatrix} C_A \\ C_B \end{pmatrix}. \tag{3.19}$$

The diagonal elements H_{AA} and H_{BB} give the onsite energies which are assumed to be zero as the reference point of energy. By assuming the nearest-neighbor approximation in tight binding model, the off-diagonal matrix element of the Hamiltonian can be written as

$$\begin{aligned} H_{AB} &= \frac{1}{N_{cell}} \sum_{<i} \sum_{j>} e^{ik.(\mathbf{R_i}-\mathbf{R_j})} < P^{A}(\mathbf{R_i})|\hat{H}|P^{B}(\mathbf{R_j}) > \\ &= \frac{1}{N_{cell}} \sum_{i=1}^{N} \sum_{j=1}^{3} e^{ik.(\mathbf{R_i}-\mathbf{R_j})} < P^{A}(\mathbf{R_i})|\hat{H}|P^{B}(\mathbf{R_j}) > \ . \end{aligned} \tag{3.20}$$

It is clear from Fig. (3.2) that any A atom interacts with 3-nearest neighbor B atoms connected to A using the $\boldsymbol{\delta}_1$, $\boldsymbol{\delta}_2$, and $\boldsymbol{\delta}_3$ vectors

$$\boldsymbol{\delta}_1 = (0\,, -a_{CC}) = a\,(0\,, -\frac{1}{\sqrt{3}})\,, \tag{3.21}$$

$$\boldsymbol{\delta}_2 = (\frac{a}{2}\,, \frac{a_{CC}}{2}) = a\,(\frac{1}{2}\,, \frac{1}{2\sqrt{3}})\,, \tag{3.22}$$

$$\boldsymbol{\delta}_3 = (\frac{-a}{2}\,, \frac{a_{CC}}{2}) = a\,(-\frac{1}{2}\,, \frac{1}{2\sqrt{3}})\,, \tag{3.23}$$

where $a = \sqrt{3}\,a_{CC}$ and $b = \frac{3}{2}\,a_{CC} = \frac{\sqrt{3}}{2}a$. Substituting the Eqs. (3.21) - (3.23) into Eq. (3.20) one can rewrite the H_{AB} as

$$\begin{aligned} H_{AB} &= e^{ik.\boldsymbol{\delta}_1} < P^{A}(\mathbf{R_A})|\,\hat{H}\,|P^{B}(\mathbf{R_{B_1}}) > \\ &+ e^{ik.\boldsymbol{\delta}_2} < P^{A}(\mathbf{R_A})|\,\hat{H}\,|P^{B}(\mathbf{R_{B_2}}) > \\ &+ e^{ik.\boldsymbol{\delta}_3} < P^{A}(\mathbf{R_A})|\,\hat{H}\,|P^{B}(\mathbf{R_{B_3}}) > \ . \end{aligned} \tag{3.24}$$

By defining the hopping parameter as $t =< P^{A}(R_A)|\,\hat{H}\,|P^{B}(R_B) >$, the H_{AB} can be written as

$$H_{AB} \equiv \varphi_0(k_x, k_y) = t\left[e^{-ik_y\,2\,b/3} + 2\,\cos(\frac{k_x\,a}{2})\,e^{ik_y\,b/3}\right]. \tag{3.25}$$

The $H_{BA} \equiv \bar{\varphi}_0(k_x, k_y)$ which is the complex conjugate of $\varphi_0(k_x, k_y)$. It is clear from Eq. (3.25) that $\bar{\varphi}_0(k_x, k_y) = \varphi_0(k_x, -k_y)$.

In the absence of spin-orbit interactions, spin-up and spin-down electrons are degenerate. The SU(2) symmetric Hamiltonian and four-component spinor wave-function in momentum space is given by

$$H = \begin{pmatrix} 0 & \varphi_0 & 0 & 0 \\ \bar{\varphi}_0 & 0 & 0 & 0 \\ 0 & 0 & 0 & \varphi_0 \\ 0 & 0 & \bar{\varphi}_0 & 0 \end{pmatrix} \quad , \quad \Psi = \begin{pmatrix} u_{A\uparrow} \\ u_{B\uparrow} \\ u_{A\downarrow} \\ u_{B\downarrow} \end{pmatrix}. \tag{3.26}$$

The eigenenergies can be obtained by diagonalizing the Hamiltonian of Eq. (3.26) as

$$E_{\pm} = \pm\sqrt{\varphi_0\,\bar{\varphi}_0} = \pm\,t\sqrt{3 + 2\,\cos(k_x\,a) + 4\,\cos(\frac{k_x\,a}{2})\cos(k_y b)}\,, \tag{3.27}$$

where E_+ gives the energy of the conduction band, and E_- gives the energy of the valence band. Two inequivalent Dirac point in k space can be obtained from Eq. (3.27) in which $E = 0$ as illustrated in Fig. (3.2).

Since the spin-up and down subspace are decoupled from each other, we write the Schrödinger's equation just in the spin-up subspace as

$$\begin{pmatrix} 0 & |\varphi|\,e^{i\,\alpha} \\ |\varphi|\,e^{-i\,\alpha} & 0 \end{pmatrix}\begin{pmatrix} u_{A\uparrow} \\ u_{B\uparrow} \end{pmatrix} = \pm|\varphi_0|\begin{pmatrix} u_{A\uparrow} \\ u_{B\uparrow} \end{pmatrix}, \tag{3.28}$$

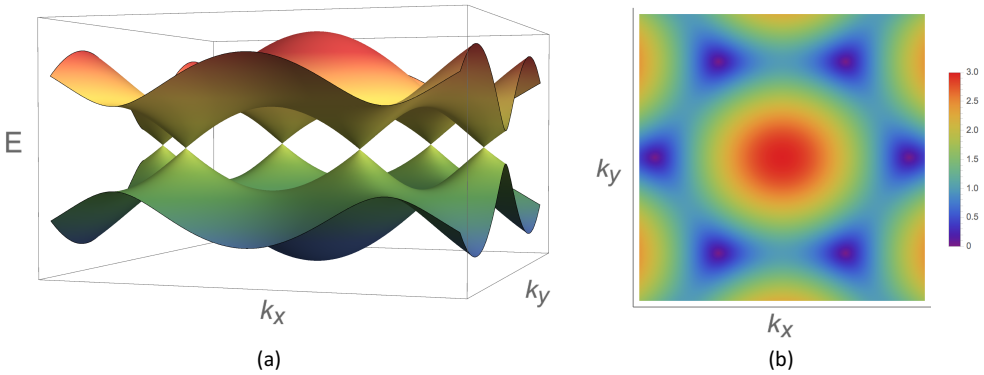

FIGURE 3.3: (a) The band structure $E(k_x, k_y)$, of monolayer graphene around the first Brillouin Zone. The conduction band and valence band meet at 6 Dirac points where E = 0. Around the touching points, the spectrum has a conical shape. (b) contour plot of the conduction band of graphene. The Dirac points are at E = 0.

in which we defined $\varphi_0 = |\varphi_0| e^{i\alpha}$. Four spinor are obtained as follows

$$\Psi_1 = \Psi_+, \uparrow = \begin{pmatrix} e^{i\alpha_0/2} \\ e^{-i\alpha_0/2} \\ 0 \\ 0 \end{pmatrix} e^{ik_x x} e^{ik_y y} \quad , \Psi_2 = \Psi_-, \uparrow = \begin{pmatrix} e^{i\alpha_0/2} \\ -e^{-i\alpha_0/2} \\ 0 \\ 0 \end{pmatrix} e^{ik_x x} e^{ik_y y},$$
$$\Psi_3 = \Psi_+, \downarrow = \begin{pmatrix} 0 \\ 0 \\ e^{i\alpha_0/2} \\ e^{-i\alpha_0/2} \end{pmatrix} e^{ik_x x} e^{ik_y y} \quad , \Psi_4 = \Psi_-, \downarrow = \begin{pmatrix} 0 \\ 0 \\ e^{i\alpha_0/2} \\ -e^{-i\alpha_0/2} \end{pmatrix} e^{ik_x x} e^{ik_y y}, \tag{3.29}$$

where ± indicates the sign of energy and ↑ and ↓ are spin's degree of freedom.

The conduction and valence band of a monolayer graphene is plotted in Fig. (3.3). In this plot, the value of t is assumed to be 2.7 eV . Each band is double degenerate. In the first Brillouin zone, six double cones meet at E = 0 eV, which are called the Dirac points or neutrality points. The band gap which is defined as the energy range between the valence band and the conduction band is zero for graphene. For an undoped sample of graphene, the Fermi level is situated at this Dirac point. Therefore, the valence band is completely filled with electrons and the conductance band is empty. Due to its zero band gap, graphene is considered as a semi-metal or zero-bandgap semiconductor, in contrast to a regular metal where Fermi energy is typically in the conduction band,

or a regular semiconductor where E_F is located inside a finite bandgap.

3.3.1 Low energy dispersion

The band structure of graphene near the Fermi energy has a linear dispersion and electrons near these points can be described by a Dirac-like Hamiltonian [36]. We expand the Hamiltonian of graphene, Eq. (3.26) around the K and K′ points by replacing $k \longrightarrow K(K') + k$. Therefore, the effective low energy Hamiltonian is obtained as

$$H_K = \hbar v_F \begin{pmatrix} 0 & k_x - i k_y \\ k_x + i k_y & 0 \end{pmatrix} = \hbar v_F k.s, \tag{3.30}$$

where v_F is called the Fermi velocity and is approximately $v_F \simeq 10^6 m/s$. The Pauli matrices $s = (\sigma_x, \sigma_y)$ operate on the sublattice degrees of freedom instead of spin, which is called pseudospin. Also, for the inequivalent K′ point one has the transposed Hamiltonian

$$H_{K'} = H_K^{\dagger}. \tag{3.31}$$

The spectrum around the Dirac points is linear

$$E_{\pm}^{linear} = \pm \eta \hbar v_F \sqrt{k_x^2 + k_y^2} = \pm \eta \hbar v_F |k| \tag{3.32}$$

$$\psi_{\pm}^{linear} = \frac{1}{\sqrt{2}} \begin{pmatrix} 1 \\ \pm \eta e^{i\eta\varphi} \end{pmatrix} e^{ik.r} \tag{3.33}$$

where ± refers to the conduction and valence band, respectively. Also, $\eta = \pm$ for K or K′ valley.

Graphene is very peculiar for this linear dispersion relation and electron-hole symmetry. The low energy description of graphene is equivalent to the massless Dirac equation in $2+1$ dimensions, with an effective speed of light, that is roughly 300 times smaller than the real speed of light. One of the direct results of this linear relation is the chiral nature of the states. The helicity or chirality operator is the projection of the sublattice pseudospin operator σ on the momentum direction

$$h = s.\frac{p}{|p|}. \tag{3.34}$$

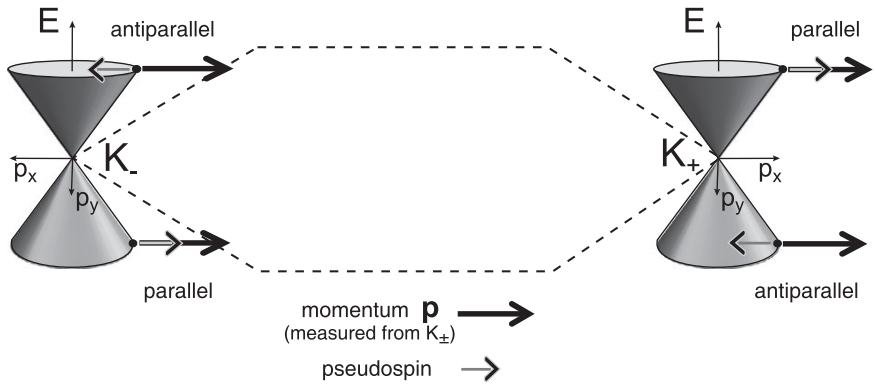

FIGURE 3.4: The direction of the pseudospin parallel or antiparallel to the momentum p of selected energies in conduction and valence bands. Figure is taken from [38].

Since the low energy effective Hamiltonian commutes with the helicity operator, the projection of the pseudospin is a well-defined conserved quantity. It is positive or negative if the pseudospin and momentum are parallel or anti-parallel, respectively (see Fig. (3.4)).

Around K, the pseudospin of eigenstates is parallel to the momentum in the conduction band and antiparallel in the valence band. The chirality, in this case, is simply the band index. The chirality around K′ is reversed as indicated in Fig. (3.4). This feature plays an important role in the properties of graphene. For example, the backscattering of electron is not possible in the pure graphene, because it needs the change of p $\longrightarrow$ –p. Since pseudospin direction is locked to the momentum, backscattering is not possible if the Hamiltonian is not perturbed by a term which flips the pseudospin [37].

3.3.2 Graphene's density of state

Since the energy dispersion, Eq. (3.32) is linear around the Dirac points, the total density of states is proportional to energy and carrier density is proportional to energy squared.

The density of states is the number of states per unit energy per unit volume

$$\rho(E) = \frac{1}{L^2}\sum_k \delta(E - E(k)) = \int g_s\, g_v \frac{2\pi\, k\, dk}{(2\pi)^2}\, \delta(E - E(k)) = \frac{2|E|}{\pi\, \hbar^2\, v_F^2}\,, \tag{3.35}$$

where $g_s = 2$ and $g_v = 2$ are the spin and valley degeneracies, respectively. So, the density of states (DoS) varies linearly with E for all E up to E ~ 1eV. The carrier

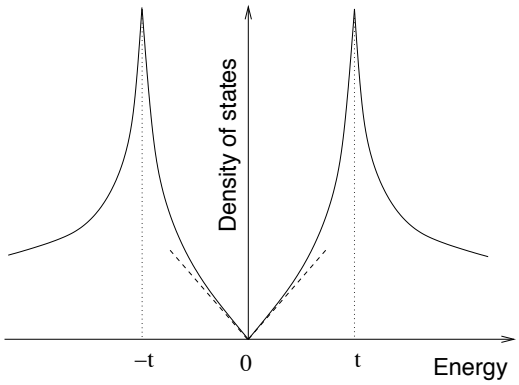

FIGURE 3.5: Schematic plot of the density of states for electrons in graphene by considering the nearest neighbor tight-binding model. The dashed line indicates that the density of states is linear near the Dirac point (Fermi energy) [39].

density is given by

$$n(E) = g_s\, g_v\, \frac{k_F^2}{4\pi} = \frac{E^2}{\pi\, \hbar^2\, v_F^2} \tag{3.36}$$

The full density of states is schematically shown in Fig. (3.5). The dashed line indicates that the density of the state is linear near the Dirac points as it is shown in Eq. (3.35). There are some saddle points in the energy dispersion at the M points at the border of first Brillouin zone which causes the divergencies in the density of state at $E = \pm t$, called van-Hove singularities [39](see Fig. (3.3)).

3.4 Graphene nanoribbons

Graphene nanoribbons, GNR, are quasi 1-D structures cut from graphene sheet in particular orientations. The GNR's electronic properties depend strongly on the shape of the edges and width of the nanoribbons. Here, we will focus on two types of ideal GNRs: Armchair GNR (AGNR) and Zigzag GNR (ZGNR) which are illustrated in Fig. (3.6). The GNRs are labeled by the number of armchair or zigzag chains present in the width direction of the AGNR and ZGNR, respectively. Let N_a be the number of armchair chains and N_z is the number of zigzag chains, so the nanoribbon can be denoted by N_a-AGNR and N_z-ZGNR, respectively. In Fig. (3.6), it has shown how to count the number of chains for example for a 9-AGNR and a 6-ZGNR. The width of GNR can be expressed in terms of the number of lateral chains as

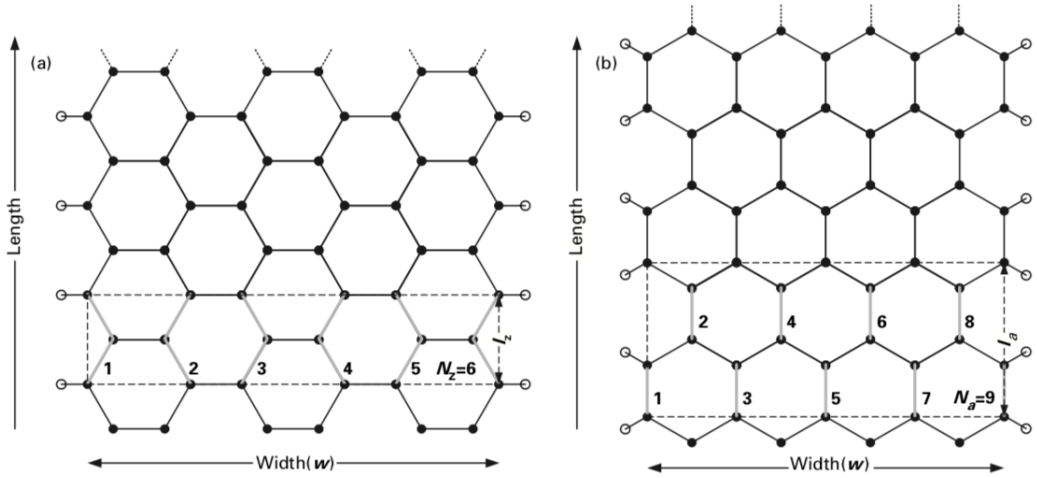

FIGURE 3.6: The honeycomb structure of GNRs. a) The lattice of a 6-ZGNR and (b) the lattice of a 9-AGNR. The dashed box represent the primitive unit cell. the bold gray lines are the armchair or zigzag chains that are used to determine N_a or N_z, respectively [40].

$$\text{AGNR, W} = \frac{\text{N}_\text{a} - 1}{2}\text{a}\,, \tag{3.37}$$

$$\text{ZGNR, W} = \frac{3\text{N}_\text{z} - 2}{2\sqrt{3}}\,\text{a}\,, \tag{3.38}$$

where a is the graphene lattice constant depicted in Fig. (3.2). The length of the primitive unit cells is $l_a = 2\,b$ and $l_z = a$ for AGNR and ZGNR, respectively. The small width of GNRs can lead to quantum confinement of electrons which restricts their motion to one dimension along the length of the nanoribbon, in contrast to a large graphene sheet where electrons are free to move in a 2-D sheet. As a result of several factors, including the quantum confinement, particular boundary conditions at the edges, and the effect of states arising from carbon atoms at the edges (known as edge states), the band structure of GNRs is generally complex and departs significantly from that of the 2-D graphene sheet. The numerical computations reveal that armchair and zigzag GNRs show metallic or semiconducting electronic properties depending on the nanoribbons width. The semiconducting property in armchair GNRs occurs when $N = 3p$ or $N = 3p + 1$ while metallic property occurs when $N = 3p + 2$, where N is the number of dimer lines and p is an integer. The energy bands for a graphene nanoribbon with periodic boundary conditions in one direction are illustrated in Fig. (3.7). The band structures of insulating and metallic armchair nanoribbon are also

shown in Fig. (3.7b, and (c)), respectively [40, 41].

3.5 Uniaxial strain

When graphene is grown on top of the substrate, deformations can be observed naturally lead to change the electronic properties of graphene. Some theoretical calculations [43] have predicted that these deformations can change the interatomic distance up to 20% without permanently deform the graphene which is observed experimentally as well [44].

Consider a graphene lattice under a uniform tension $\mathbf{T}$, with angle ϑ with respect to the Ox axis which is always in the zigzag direction of the lattice. With this chosen coordinates, the tension is $\mathbf{T} = (\mathrm{T}\cos(\vartheta), \mathrm{T}\sin(\vartheta))$. According to the generalized Hooke's law for solids, the stress is related to the tension as

$$\tau_{ij} = C_{ijkl}\,\varepsilon_{kl}\,, \quad \varepsilon_{ij} = S_{ijkl}\,\tau_{kl}\,, \tag{3.39}$$

where C_{ijkl} and S_{ijkl} are the stiffness and compliance tensor components respectively. For the planar tension, the stress and strain tensors reduce to two dimensions. On the other hand, graphene is elastically isotropic [45], means that the elastic components of these tensors are coordinate independent. In the principal coordinate system Ox′y′, the strain is simply $\varepsilon'_{ij} = S_{ijkl}\tau'_{kl}$. By substituting the tension $\mathbf{T} = \mathrm{T}\mathbf{e}_{x'}$, we have

$$\varepsilon'_{ij} = \mathrm{T}\,S_{ijkl}\delta_{kx}\delta_{lx} = \mathrm{T}\,S_{ijxx}. \tag{3.40}$$

The compliance tensor has only five independent components for graphite [46]

$$S_{xxyy},\ S_{zzyy},\ S_{xxzz},\ S_{zzzz},\ S_{yzyz}. \tag{3.41}$$

Therefore, the non-zero components of the strain tensor are

$$\varepsilon'_{xx} = \mathrm{T}\,S_{xxxx}\,,\ \varepsilon'_{yy} = \mathrm{T}\,S_{xxyy}\,, \tag{3.42}$$

which represent the longitudinal deformation and Poisson's transverse contraction. By defining the Poisson's ratio as $\sigma = -S_{xxxy}/S_{xxxx}$, the strain in the Ox′y′ coordinate is

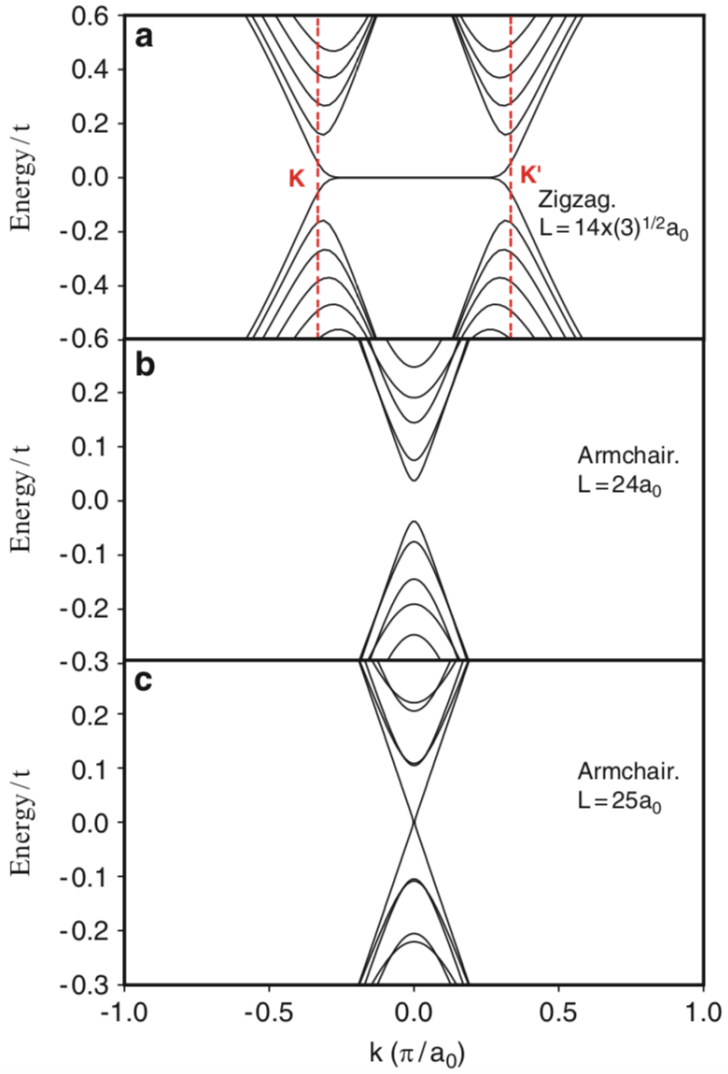

FIGURE 3.7: Examples of energy bands for a graphene nanoribbon with periodic boundary conditions in one direction. k is the wavevector parallel to the nanoribbon edge, measured with respect the center of the Brillouin center. (a) Ribbon terminated in zigzag edges with 56 atoms in the unit cell. The dispersionless states correspond to confined surface states. The band structures of insulating and metallic armchair nanoribbons are shown in (b) and (c) respectively [41].

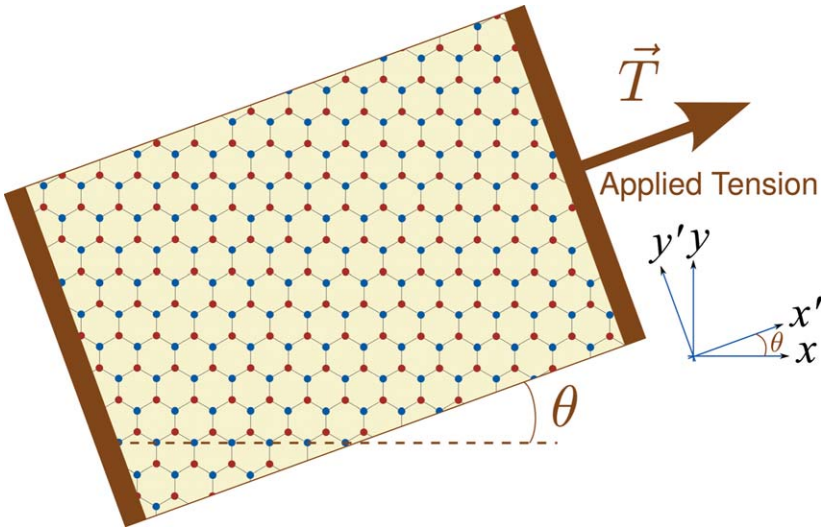

FIGURE 3.8: A planar tension is applied to a graphene lattice. The zigzag direction of the honeycomb lattice is always parallel to the axis Ox. Figure is taken from [42]

written as

$$\boldsymbol{\varepsilon}' = \varepsilon_0 \begin{pmatrix} 1 & 0 \\ 0 & -\sigma \end{pmatrix}, \tag{3.43}$$

which means that graphene responds to the tension as an isotropic elastic medium. The known value for the Poisson's ratio of graphene is $\sigma = 0.165$ [46].

By transforming the strain in the original Oxy coordinate, the strain tensor is

$$\boldsymbol{\varepsilon} = \varepsilon_0 \begin{pmatrix} \cos^2\vartheta - \sigma\sin^2\vartheta & (1+\sigma)\cos\vartheta\sin\vartheta \\ (1+\sigma)\cos\vartheta\sin\vartheta & \sin^2\vartheta - \sigma\cos^2\vartheta \end{pmatrix}. \tag{3.44}$$

In this thesis, we are interested in cases where the graphene is adhering to the top of a substrate and strain is induced in graphene by mechanically put the substrate under the stress. So, here we consider ε_0 as a tunable parameter determining the strength of strain.

3.5.1 Bond deformation

When graphene lattice is under strain, the interatomic distance of lattice change according to

$$\boldsymbol{\delta}_i^s = (\mathbf{1} + \boldsymbol{\varepsilon}) \cdot \boldsymbol{\delta}_i \,, \tag{3.45}$$

where $\boldsymbol{\delta_i}$ and $\boldsymbol{\delta_i^s}$ are the vectors that define the nearest neighbor in the graphene without and with applied strain, $\mathbf{1}$ is the identity matrix and $\boldsymbol{\varepsilon}$ is the strain matrix.

In this thesis, we consider only two types of uniaxial strain: $\vartheta = 0$ and $\vartheta = \pi/2$ corresponding to tension along the zigzag ($\mathcal{Z}$) and armchair ($\mathcal{A}$) directions, respectively. According to the Eq. (3.45), the $\boldsymbol{\delta_i^s}$ vectors along the zigzag and armchair directions are given by

$\mathcal{Z}$ direction	$\mathcal{A}$ direction
$\boldsymbol{\delta_1^s} = a\left(0\,,\,\frac{-1+\varepsilon_0\,\sigma}{\sqrt{3}}\right)$	$\boldsymbol{\delta_1^s} = a\left(0\,,\,\frac{-1-\varepsilon_0}{\sqrt{3}}\right)$
$\boldsymbol{\delta_2^s} = a\left(\frac{1+\varepsilon_0}{2}\,,\,\frac{1-\varepsilon_0\,\sigma}{2\sqrt{3}}\right)$	$\boldsymbol{\delta_2^s} = a\left(\frac{1-\varepsilon_0\,\sigma}{2}\,,\,\frac{1+\varepsilon_0}{2\sqrt{3}}\right)$
$\boldsymbol{\delta_3^s} = a\left(\frac{-1-\varepsilon_0}{2}\,,\,\frac{1-\varepsilon_0\,\sigma}{2\sqrt{3}}\right)$	$\boldsymbol{\delta_3^s} = a\left(\frac{-1+\varepsilon_0\,\sigma}{2}\,,\,\frac{1+\varepsilon_0}{2\sqrt{3}}\right)$

Therefore, the bond lengths deform differently along the $\mathcal{Z}$ and $\mathcal{A}$. By assuming the small strain, these bond lengths are given by

$$\mathcal{Z}: \quad |\boldsymbol{\delta}_2^s| = |\boldsymbol{\delta}_3^s| = a_{CC}\left(1 + \tfrac{3}{4}\varepsilon_0 - \tfrac{1}{4}\varepsilon_0\,\sigma\right)\,,\ |\boldsymbol{\delta}_1^s| = a_{CC}\,(1 - \varepsilon_0\sigma)\,, \tag{3.46a}$$

$$\mathcal{A}: \quad |\boldsymbol{\delta}_2^s| = |\boldsymbol{\delta}_3^s| = a_{CC}\left(1 + \tfrac{1}{4}\varepsilon_0 - \tfrac{3}{4}\varepsilon_0\,\sigma\right)\,,\ |\boldsymbol{\delta}_1^s| = a_{CC}\,(1 + \varepsilon_0)\,. \tag{3.46b}$$

Changing the the bond lengths Eq. (3.46) leads to different hopping amplitudes among neighboring sites. One of most used methods to obtain the new hopping parameters suggests that $t^s(\boldsymbol{\delta_i}) \propto 1/(|\boldsymbol{\delta_i}|)^2$ [47]. Although, this dependency comes from matching the tight-binding and free electron dispersions of simple systems in equilibrium and fails away from the equilibrium distance [48]. A more reasonable assumption is an exponential decay [49]

$$t^s = t_0 e^{-3.37(|\boldsymbol{\delta_i^s}|/|\boldsymbol{\delta_i}|-1)}\,, \tag{3.47}$$

where t^s is the hopping parameter for a bond of length $|\boldsymbol{\delta_i^s}|$ and t_0 is the hopping parameter for the bond with length $|\boldsymbol{\delta_i}|$. The rate of decay is extracted from the experimental result [50]. According to Eq. (3.47), the next nearest neighbor hopping (t') in graphene would have the value $t'(a) = 0.23$ eV, which is in consistence with the existing estimates of t' in graphene [51].

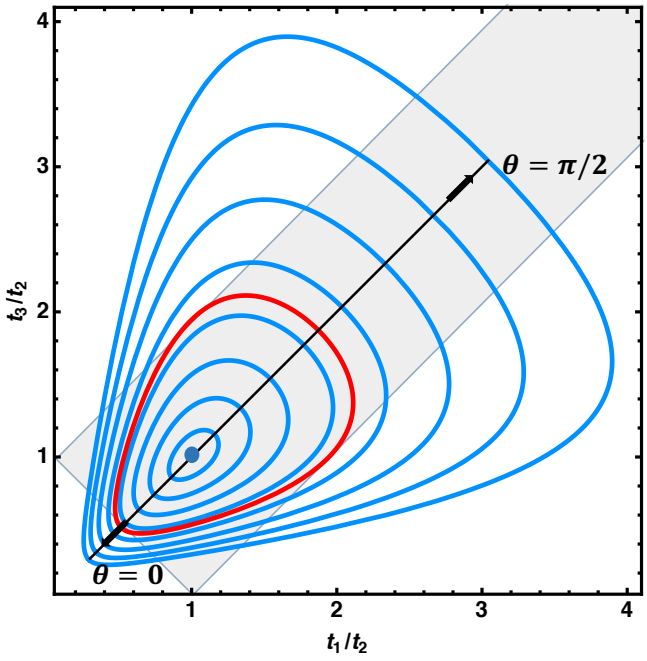

FIGURE 3.9: The ratio of t_1/t_2 vs t_3/t_2 as a function of strain modulus, ε_0, and strain direction ϑ. Each closed line is plotted for the constant ε_0 in the region of $(0, 0.4)$ for different value of ϑ ranges from 0 to π. The zigzag direction is along $\vartheta = 0$, and the armchair direction is at $\vartheta = \pi/2$. The red closed curve is plotted for the value of $\varepsilon_0 \approx 0.23$ corresponds to the gap threshold. Inside the gray area the spectrum is gapless.

The general form of the Hamiltonian matrix element in Eq. (3.24) with arbitrary hoppings t_1, t_2, and t_3 is

$$H_{AB} = t_1\, e^{ik.\boldsymbol{\delta}_1^s} + t_2\, e^{ik.\boldsymbol{\delta}_2^s} + t_3\, e^{ik.\boldsymbol{\delta}_3^s}\,, \tag{3.48}$$

and the band energies are given by

$$E(k_x, k_y) = \pm \left| t_1\, e^{ik.\boldsymbol{\delta}_1^s} + t_2\, e^{ik.\boldsymbol{\delta}_2^s} + t_3\, e^{ik.\boldsymbol{\delta}_3^s} \right|. \tag{3.49}$$

It is shown that the spectrum remains gapless as long as the condition

$$\left| \frac{|t_1|}{|t_2|} - 1 \right| \leq \frac{|t_3|}{|t_2|} \leq \left| \frac{|t_1|}{|t_2|} + 1 \right| \tag{3.50}$$

is satisfied [42]. The gray area in Fig. (3.9) shows the region of validity of this condition. In this figure, we have plotted the evolution of hopping ratios with ε_0 and ϑ. The red close curve is plotted for the value of $\varepsilon_0 \approx 0.23$ corresponds to the gap threshold. The figure shows that for the values of ε_0 less than 0.23, there is no band gap. The general results of this figure can be expressed as:

- The gap threshold is $\sim 20\%$ at $\varepsilon_0 \approx 0.23$.
- The behavior of the system is periodic in ϑ with period $\pi/3$, in consistence with the symmetry of the lattice.
- Tension along the zigzag direction ($\vartheta = 0, \pi/3, \dots$) is more effective in opening the gap.
- Tension along the armchair direction never open a gap.

The isotropic point $(1, 1)$ in Fig. (3.9) is where there is no strain. The fact that there is a gray area around this point means that gapless structure of the energy dispersion is robust and in order to generate a gap in the band structure, a critical strain is needed. So, while the applied strain is inside this region, there is no band gap.

In Fig. (3.10), we plot the ratio of t_α^s/t_0 , ($\alpha = 1, 2, 3$), versus ϑ for different values ε_0 . The strain modulus is $\varepsilon_0 = 0.05, 0.15, 0.23$ in Fig. (3.10a), (b) and (c) respectively. The blue curve shows the armchair bond, while the red and green curves indicating the zigzag bonds. The relative change in the bond hopping strongly

depends on the direction of strain ϑ . For instance, when tension is applied along the zigzag direction, see Fig. (3.2), the hopping parameter of zigzag bonds ($t_{2,3}$) show the highest relative change. While the hopping t_1 changes more strongly when tension is applied along the armchair direction $\vartheta = \pi/2$.

Changing the hopping parameters distort the dispersion relation. In Fig. (3.11a) we plot the conduction and valence band of graphene versus k_x under the strain in zigzag direction with different strain modulus. We have renormalized the k_x by the lattice constant in each case and $k_y = 0$ for all of them. The blue curves, show the bands without strain $\varepsilon_0 = 0$. We see that by increasing the strain modulus, two Dirac points get closer to each other and finally at $\varepsilon_0 = 0.23$ they merge (red curves). This is the critical value for the gap threshold. By increasing ε_0 from this critical value, a gap has emerged. The black curves show a relatively large band gap at $\varepsilon_0 = 0.4$. The same strain is applied in the armchair direction and the resultant bands are plotted in Fig. (3.11b). As we expected, by applying strain in the armchair direction two nonequivalent Dirac cones move in opposite directions and never meet. So, the dispersion relation remains gapless.

In order to see how the whole first Brillouin zone change under the strain, we show the contour plot the conduction band of graphene under the same strain modulus applied in the zigzag direction in Fig. (3.12). It can be seen that the cones always approach each other and will eventually merge, as we see in Fig. (3.11a) before. The Fig. (3.13) show the conduction band under the strain in armchair direction. Despite the zigzag direction, two Dirac coins move opposite each other and never meet.

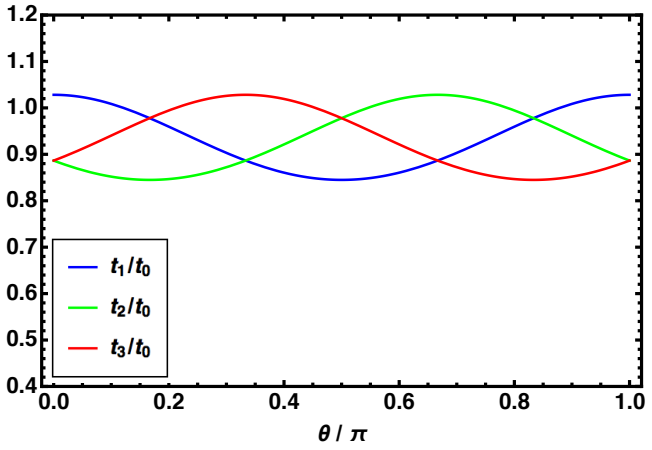

(a)

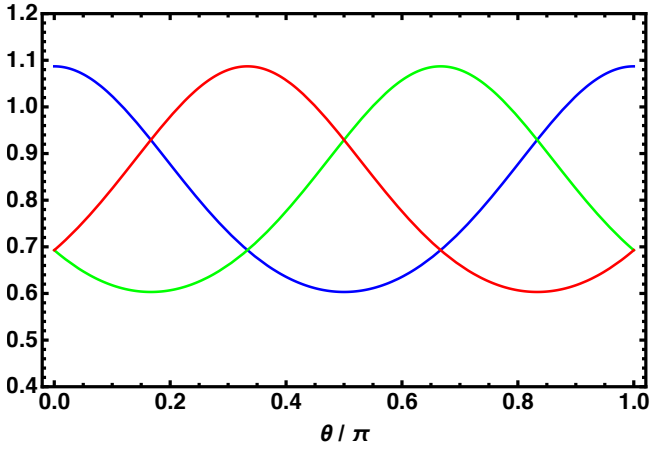

(b)

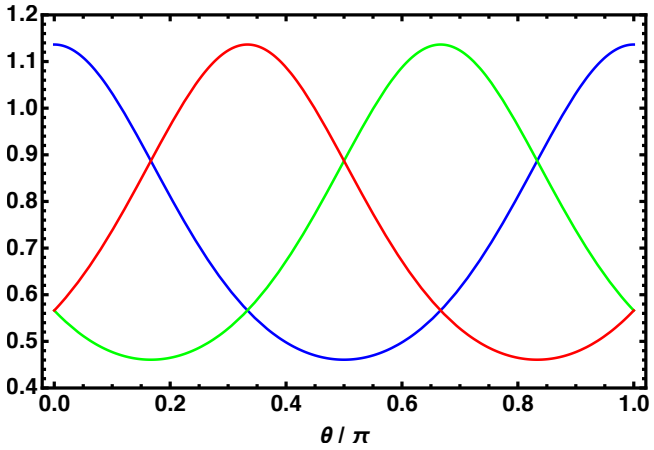

(c)

FIGURE 3.10: (Color online) Plot of t_1/t_0, t_2/t_0 and t_3/t_0 as a function of ϑ for different values of strain modulus a) $\varepsilon_0 = 0.05$, b) $\varepsilon_0 = 0.15$, and c) $\varepsilon_0 = 0.23$ which is the gap threshold. When tension is applied along the zigzag direction, the hopping parameter of zigzag bonds ($t_{2,3}$) show the highest relative change. While the hopping t_1 changes more strongly when tension is applied along the armchair direction $\vartheta = \pi/2$.

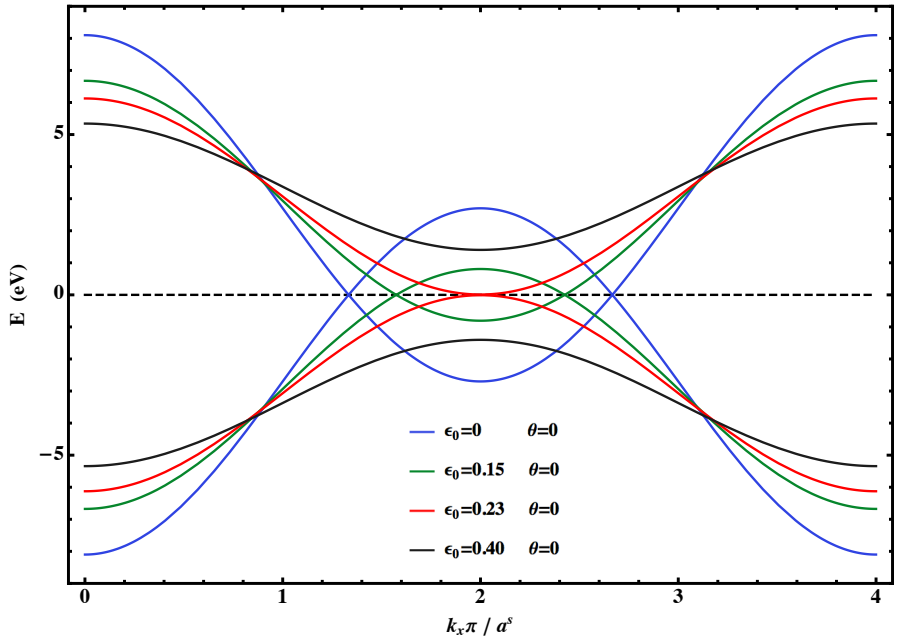

(a)

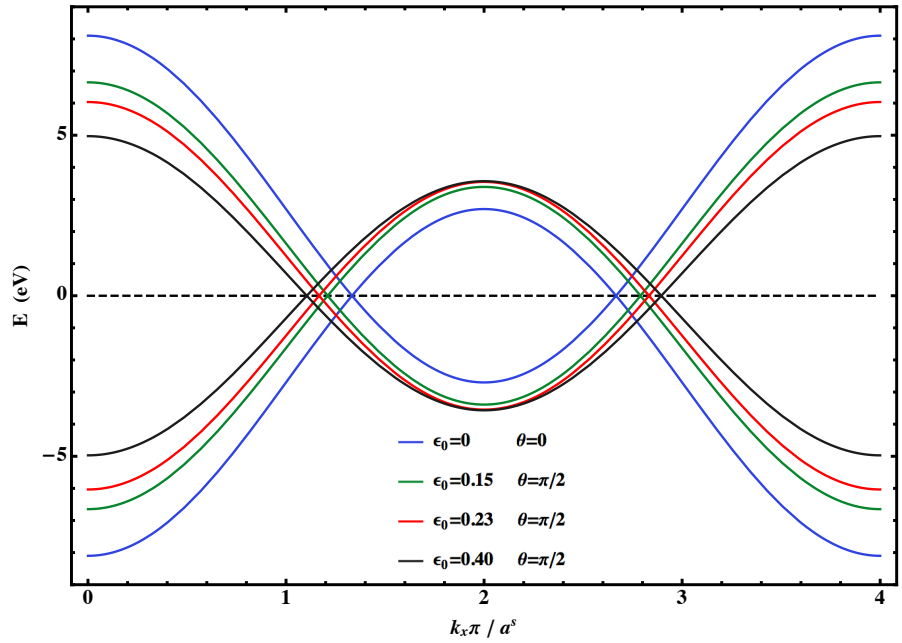

(b)

FIGURE 3.11: (Color online) The conduction and valence band of graphene versus k_x under the strain in a) zigzag direction and b) armchair direction with different strain modulus. Applying strain larger than ≈ 0.23 in zigzag direction, eventually open a gap in the band structure, while strain in the armchair direction never opens a gap.

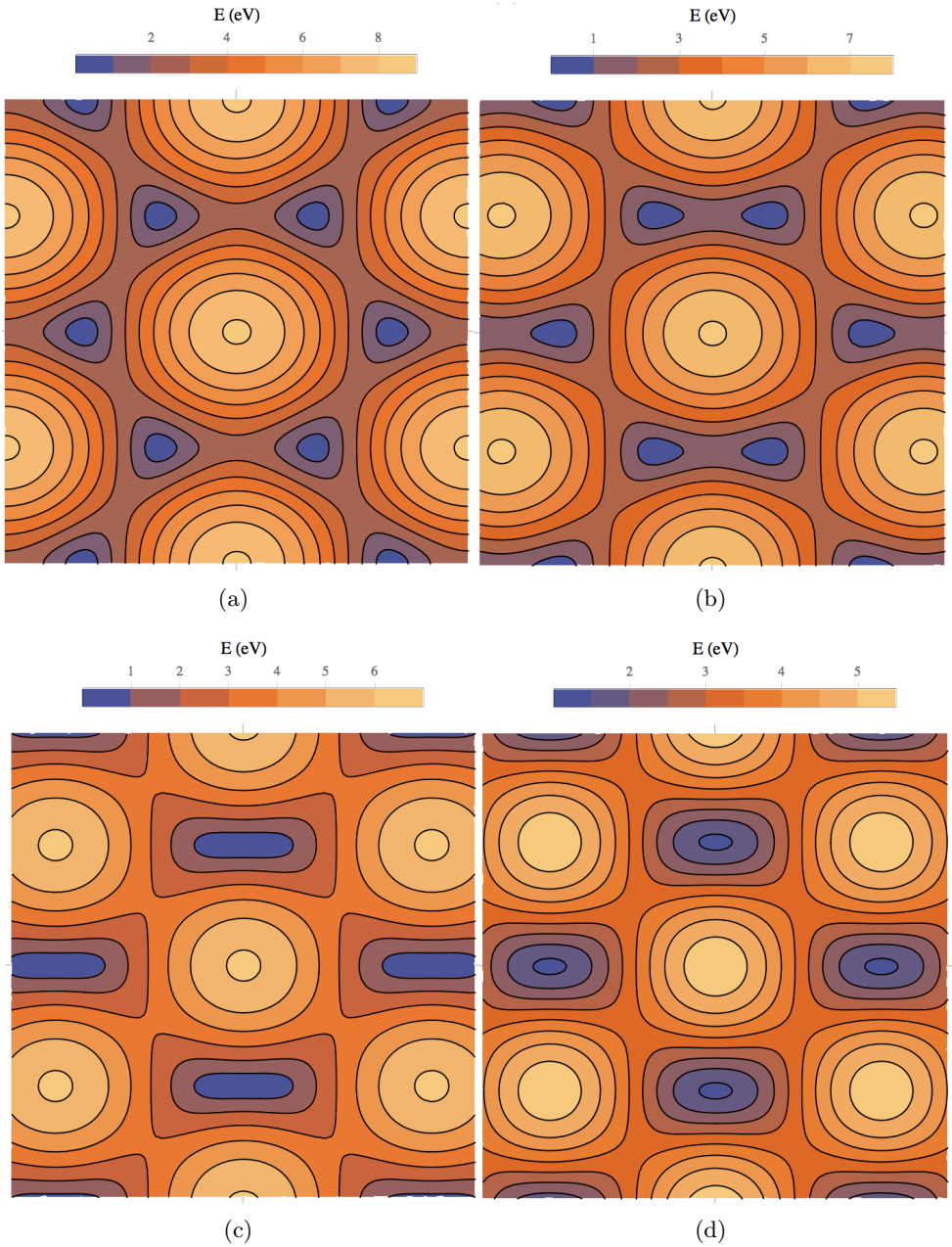

FIGURE 3.12: (Color online) The density plots of the energy dispersion, $E(k_x, k_y)$, for a) $\{\varepsilon_0 = 0, \vartheta = 0\}$, b) $\{\varepsilon_0 = 0.15, \vartheta = 0\}$, c) $\{\varepsilon_0 = 0.23, \vartheta = 0\}$, d) $\{\varepsilon_0 = 0.4, \vartheta = 0\}$. As we see from the plots, two nonequivalent Dirac cone approach each other and eventually merge at $\varepsilon_0 = 0.23$.

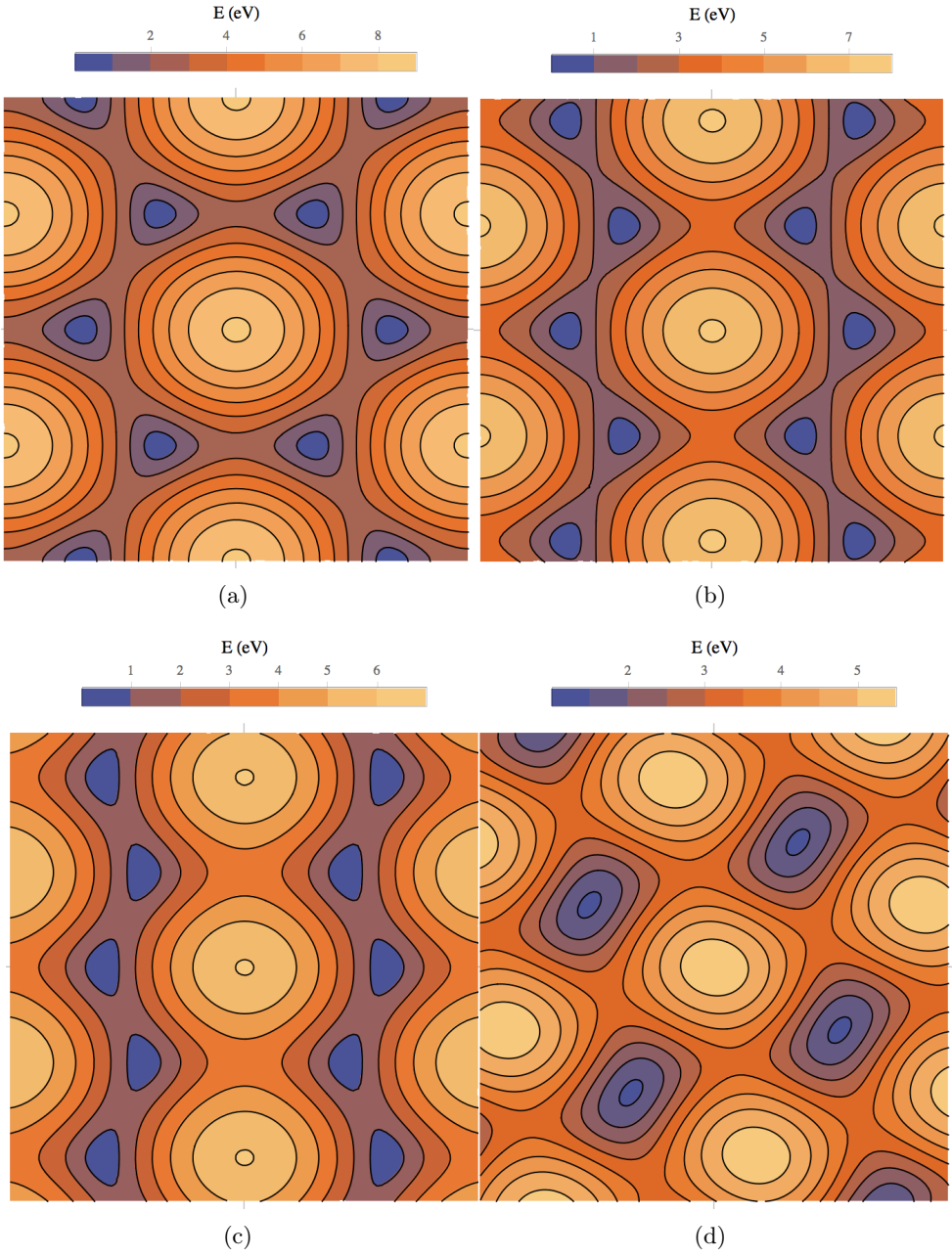

FIGURE 3.13: (Color online) The density plots of the energy dispersion, $E(k_x, k_y)$, for a) $\{\varepsilon_0 = 0, \vartheta = \pi/2\}$, b) $\{\varepsilon_0 = 0.15, \vartheta = \pi/2\}$, c) $\{\varepsilon_0 = 0.23, \vartheta = \pi/2\}$, d) $\{\varepsilon_0 = 0.4, \vartheta = \pi/2\}$. As we see from the plots, two nonequivalent Dirac cone move away from each other and never meet.

Chapter 4

Modeling procedure of graphene nanoribbon resonant-tunneling transistor

4.1 Introduction

Van der Waals heterostructures, composed of individual two-dimensional material have been developing very fast. Recently, multilayer stacks of graphene [52, 53] and other two dimensional atomic layers, such as hexagonal boron-nitride (hBN), Molybdenum disulfide, black phosphorus, etc., has attracted immense attentions [54, 55, 16]. Graphene, exhibiting outstanding electronic and mechanical properties, such as high mobility of carriers, linear dispersion, perfect 2-D confinement and symmetric electronic band structure have sparked many interest [56, 57]. While hexagonal boron-nitride is an insulator with a large energy bandgap and has a great potential to use as the dielectric layer in functional heterostructure devices. Graphene and hBN share the same crystal structure and have very similar lattice constant (There is 1.8 % mismatch in the lattice constant between hBN and graphene which is ignored) [58, 59, 60].

In this chapter, we consider a resonant tunneling device in which carriers tunnel through thin hBN layers sandwiched between two graphene layers across which a bias voltage is applied. These devices have potential for future high-frequency and logic applications [61, 62, 63]. In the present study, we investigate the effect of uniaxial strain on the layers of a resonant tunneling transistor.

We use the nonequilibrium Green's function (NEGF) formalism, combined with

a nearest-neighbor tight-binding method to calculate the electronic transport characteristics of a resonant tunneling transistor which consist of two metallic armchair graphene nanoribbon (GNR) electrodes and a thin hBN tunnel barrier [64, 65, 66, 67]. We focus on how applied strain can affect the current-voltage characteristics of GNR/hBN resonant tunneling transistors.

4.2 Modeling

4.2.1 Structure of the device

We consider a resonant tunneling transistor which is schematically shown in Fig. (4.1). The active part is placed on a thick hBN substrate on top of a silicon oxide substrate. A few layers of hBN sandwiched between two metallic armchair graphene nanoribbon electrodes, which the bottom graphene electrode acts as the source and the top one acts as the drain. The doped Si substrate act as a gate electrode of the device.

A tunnel current can be generated when we apply a bias voltage V_b, between the bottom and the top graphene nanoribbon electrodes, and the gate voltage V_g, is applied between the doped Si and the bottom electrode. We will have resonant tunneling current (see Appendix. A) when the Dirac points of two GNR electrodes are aligned and this alignment can be tuned by adjusting V_g [65, 68].

The width of nanoribbon can be obtained from the below relation

$$W = \frac{1}{2}(N-1)a, \tag{4.1}$$

where N is the number of dimer lines ($N = 6p + 2$ where $p = 1, 2, 3, ...$) and a is the lattice constant of graphene, see Fig. (3.2). We consider undoped metallic armchair GNR (AGNR) electrodes and assume that AGNR/$(hBN)_q$/AGNR has AB stacking (Bernal Order) shown in Fig. (4.2a) and also the lattice constant of hBN is equal to the GNR (shown in Fig. (4.2b)).

4.2.2 Non-equilibrium Green's function simulation

We use nearest neighbor tight-binding method to obtain tunneling current for the device [65, 4, 68], which composed of N_L layers ($N_L = 2 + q$).

We assign below indices to specify each lattice point:

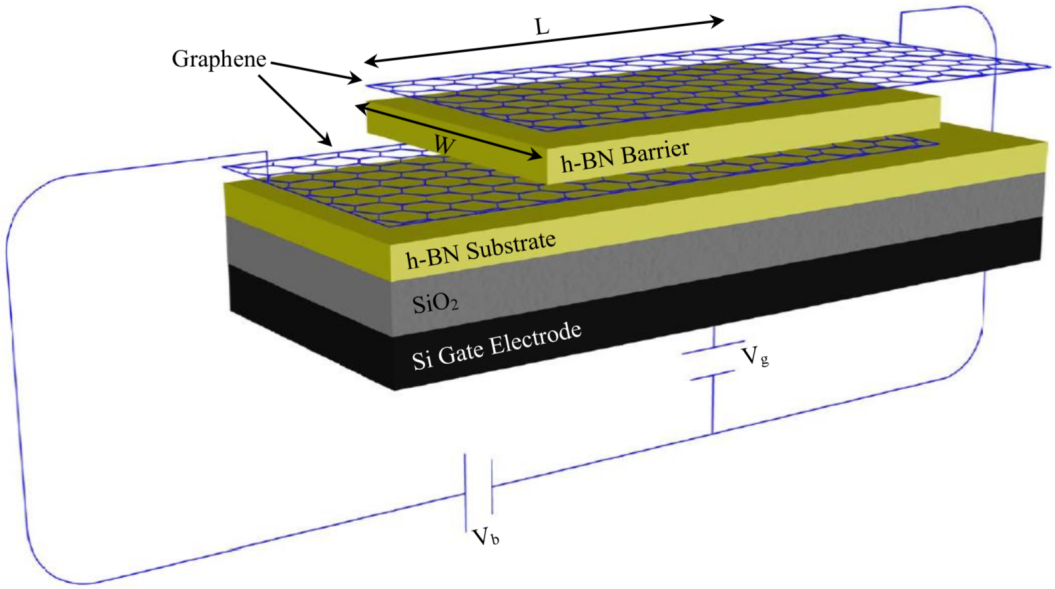

FIGURE 4.1: The active part of resonant tunneling transistor in length L and width W , which consists of two GNR electrodes and a few hBN layers between them, is placed on a thick hBN substrate on an oxidized Si substrate.

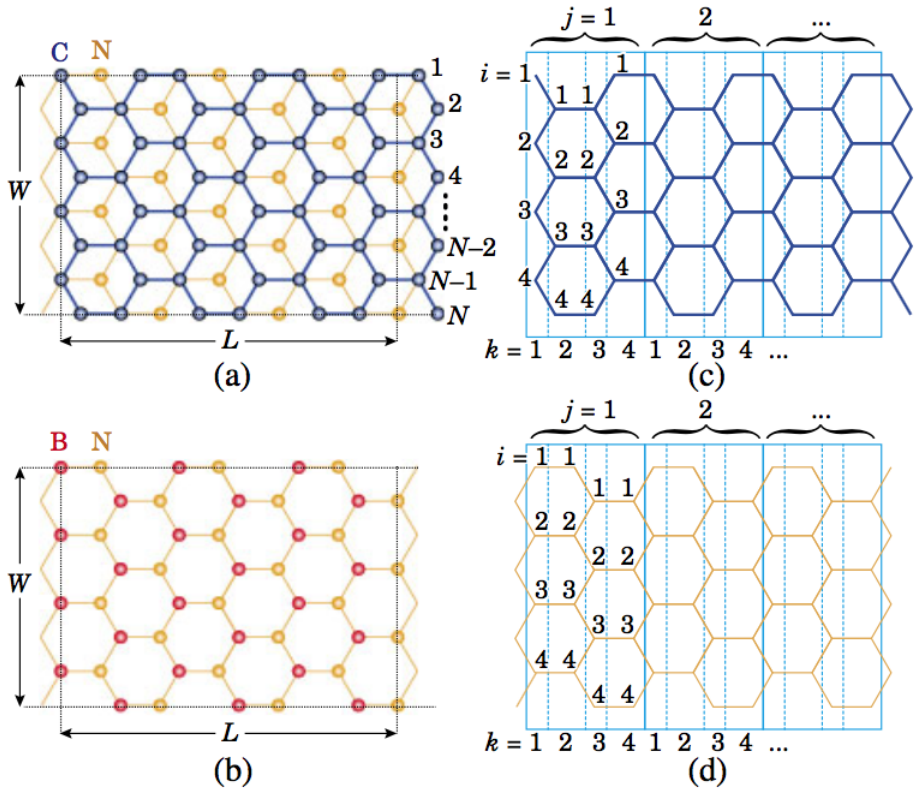

FIGURE 4.2: Stacking arrangement of the device from top view[65].

- Index l is for each layer, i.e., $l = 1$ for the bottom AGNR layer, $l = 2, 3, ..., N_L - 1$ for the hBN layers and $l = L$ for the top AGNR layer.
- Index j is for each unit cell, while it can be decomposed into four slices with index k, i.e., $k = 1, 2, 3, 4$(shown in Fig. 4.2 (c and d)).
- In a single layer of a slice, there are $N_W (= \frac{N}{2} = 4)$ atoms and we assign index i for each atom, i.e., $i = 1, 2, 3, 4$.

So, a lattice point can be specified by a combination of a unit cell index j, a slice index k, a layer index l and an atom index i. The tight-binding parameters which are needed to build the Hamiltonian matrices are on-site energies (E_C, E_B and E_N), intra-layer transfer energies (T_{C-C} and T_{B-N}) and inter-layer transfer energies (t_{C-B}, t_{B-N} and t_{C-N}).

In order to obtain the number of unit cells, M in a device, we use this relation

$$L = (M - \frac{1}{6})\sqrt{3}a, \tag{4.2}$$

where, L is the device length and a is the lattice constant.

One can write the Hamiltonian of the device as a $(4MN_WN_L)\times(4MN_WN_L)$ matrix

$$\hat{\mathcal{H}}_{dev} = \begin{pmatrix} \mathcal{H}_1 & \mathcal{S} & & \\ \mathcal{S}^\dagger & \mathcal{H}_2 & \mathcal{S} & \\ & & \ddots & \\ & & \mathcal{S}^\dagger & \mathcal{H}_M \end{pmatrix}, \tag{4.3}$$

where $\mathcal{H}_j, (j = 1, 2, ..., M)$ is the Hamiltonian matrix of size $(4N_WN_L) \times (4N_WN_L)$ describing an isolated unit cell and $\mathcal{S}$ is the transfer matrix between the neighboring unit cells. $\mathcal{H}_j$ and $\mathcal{S}$ can be written as

$$\mathcal{H}_j = \begin{pmatrix} H_1 & S_{12} & & \\ S_{12}^\dagger & H_2 & S_{23} & \\ & S_{23}^\dagger & H_3 & S_{34} \\ & & S_{34}^\dagger & H_4 \end{pmatrix}, \tag{4.4}$$

$$\mathcal{S} = \begin{pmatrix} 0 & 0 & 0 & 0 \\ 0 & 0 & 0 & 0 \\ 0 & 0 & 0 & 0 \\ S_{41} & 0 & 0 & 0 \end{pmatrix}. \tag{4.5}$$

In Eqs. (4.4) and (4.5) , H_k is the Hamiltonian matrix of the size $(N_W N_L)\times(N_W N_L)$ for an isolated slice k and $S_{kk'}$ represents the transfer matrix between the slices k and k′. H_k and $S_{kk'}$ are given by

$$H_k = \begin{pmatrix} h_1^k & s_{12}^k & & \\ s_{12}^{k\dagger} & h_2^k & s_{23}^k & \\ & & \ddots & \\ & & s_{N_L-1,N_L}^{k\dagger} & h_{N_L}^k \end{pmatrix}, \tag{4.6}$$

$$S_{kk'} = \begin{pmatrix} t_{11}^{kk'} & & & \\ & t_{22}^{kk'} & & \\ & & \ddots & \\ & & & t_{LL}^{kk'} \end{pmatrix}, \tag{4.7}$$

where $s_{ll'}^k$ is the inter-layer transfer matrix between the layers l and l′, $t_{ll'}^{kk'}$ is the transfer matrix between corresponding layers in slice k and k′ and h_l^k is the Hamiltonian matrix of the size $(N_W \times N_W)$ for a layer l in a slice k. The h_l^k matrices can be written as

$$h_l^k = \begin{pmatrix} E_1^\alpha + V_l & & & \\ & E_2^\alpha + V_l & & \\ & & E_3^\alpha + V_l & \\ & & & \ddots \end{pmatrix}, \tag{4.8}$$

where E_i^α, (α = C, B and N) is the on-site energy for each atom, i in a layer l and a slice k. The potential has been taken uniform in a single layer. Therefore, the potential energy for a layer l, denoted by V_l, is included into the diagonal part of h_l^k in the Eq. (4.8). Evaluating These potential energies are discussed in the next subsection.

As depicted in Fig. (4.1), there are two semi-infinite leads connected to the device. The bottom-left and top-right electrodes act as a source and drain, respectively. We obtain the influence of each lead on the device as a self-energy matrix of size $(N_W \times N_W)$

by the method which will be explained in the Section 4.2.4. In the following, the the self-energies for the bottom-left and top-right leads are denoted by $\sigma_L(E)$ and $\sigma_R(E)$, respectively.

For consistency in the calculation, we have to build the left and right electrode self-energy matrices of size $(N_W N_L) \times (N_W N_L)$ as

$$\Sigma_L(E) = \begin{pmatrix} \sigma_L(E) & & & \\ & 0 & & \\ & & \ddots & \\ & & & 0 \end{pmatrix}, \tag{4.9}$$

and

$$\Sigma_R(E) = \begin{pmatrix} 0 & & & \\ & 0 & & \\ & & \ddots & \\ & & & \sigma_R(E) \end{pmatrix}. \tag{4.10}$$

Then, the total self-energy matrix of size $(4MN_W N_L) \times (4MN_W N_L)$ can be written as

$$\hat{\Sigma}(E) = \begin{pmatrix} \Sigma_L(E) & & & \\ & 0 & & \\ & & \ddots & \\ & & & \Sigma_R(E) \end{pmatrix}. \tag{4.11}$$

The tunneling current, I in the ballistic limit can be obtained from

$$I = \frac{2e}{h} \int T(E)[f_s(E) - f_d(E)]dE, \tag{4.12}$$

where, f(E) is the Fermi-Dirac distribution function and $\mu_{L/R}$ represents the Fermi level of the left (top) and right (bottom) graphene layers. T(E) is the transmission function given by [65, 4, 68]

$$T(E) = \text{trace}[\Gamma_L(E)\, G(E)\, \Gamma_R(E)\, G^{\dagger}(E)], \tag{4.13}$$

where $G(E) = [E - \hat{\mathcal{H}}_{dev} - \hat{\Sigma}(E)]^{-1}$ is the Green's function of the device, $\Gamma_L(E) = i[\hat{\Sigma}_L(E) - \hat{\Sigma}_L^{\dagger}(E)]$ and $\Gamma_R(E) = i[\hat{\Sigma}_R(E) - \hat{\Sigma}_R^{\dagger}(E)]$ are the broadening functions.

Matrices $\hat{\Sigma}_L(E)$ and $\hat{\Sigma}_R(E)$ of size $(4MN_WN_L) \times (4MN_WN_L)$ can be written as

$$\hat{\Sigma}_L(E) = \begin{pmatrix} \sigma_L(E) & & & \\ & 0 & & \\ & & \ddots & \\ & & & 0 \end{pmatrix}, \tag{4.14}$$

$$\hat{\Sigma}_R(E) = \begin{pmatrix} 0 & & & \\ & \ddots & & \\ & & 0 & \\ & & & \sigma_R(E) \end{pmatrix}. \tag{4.15}$$

We have used the recursive method discussed in Chapter 2 to calculate the Green's function G(E).

4.2.3 Evaluation of potential energies of layers

As depicted in Fig. (4.1), two voltages have been applied to the device; a gate voltage, V_g and a bias voltage, V_b. These voltages can control induced carrier densities in the bottom,n_B and the top,n_T AGNR electrodes, respectively. We evaluate the internal potential energies of layers, V_l ($l = 1, ..., N_L$) by converting the external applied voltages (V_g, and V_b) within a capacitance model which compromises the quantum capacitance [69].

We assume the electronic charge is defined as $e > 0$ and $n_{B,T} > 0$ for holes and $n_{B,T} < 0$ for electrons. When $V_g = V_b = 0$, then $n_B = n_T = 0$ and chemical potentials (Fermi energies) for the bottom and top AGNR layers are at the Dirac point. One can obtain the potential energies, V_1 and V_L, of the source and the drain electrodes by self- consistently solving the following two equations

$$\frac{e^2\, n_T}{\varepsilon_{BN}}\, d_{BN} + \mu_T - \mu_B = e\, V_b \tag{4.16}$$

$$\frac{e^2\, (n_T + n_B)}{\varepsilon_g}\, d_g + \mu_B = e\, V_g, \tag{4.17}$$

where $\varepsilon_{BN} = \varepsilon_g = 3.9$ are the permittivity constants, d_g is the oxide thickness, d_{BN} is the hBN thickness, μ_T and μ_B are the chemical potentials of graphene electrodes defined as $\mu_{T(B)} = \pm\hbar v_F \sqrt{\pi\, |n_{T(B)}|}$ with v_F being the Fermi velocity of graphene. Note

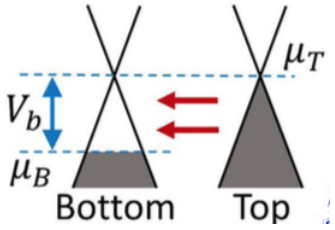

FIGURE 4.3: An explanation of the resonant tunneling in the presence of external voltages[57].

that in this letter, the chemical potential is defined as the Fermi energy of graphene electrodes minus their respective Dirac points [70].

In this study, we use a theoretical prediction ($V_b = -0.01\,V_g$) which is derived from the physical model of the device [57] to evaluate of potential energy of layers. Since the metallic graphene layers have much higher conductivity than hBN, the applied bias voltage rigidly shifting the electrostatic potential of the bottom graphene electrode by the amount equals to $U = -e\,V_b$, while the electrostatic potential of the top graphene layer remains zero. The electrostatic potential at each of the sandwiched hBN layers is obtained by assuming a linear potential profile between the bottom and the top electrodes. The bias voltage controls the chemical potential of contacts $\mu_B = -e\,V_b$ and $\mu_T = 0$ for bottom and top graphene layers, respectively (See Fig. 4.3). The gate voltage shift the electrostatic potential at the bottom electrode by $\Delta U = -0.01e\,V_g$ [57].

4.2.4 Evaluation of self-energy

In order to calculate the self-energy of the leads attached to the device, it is essential to evaluate the surface Green's function of the isolated leads, g_l^i as

$$g_l^i = [E + i\eta - H_l^i]^{-1}, \tag{4.18}$$

where H_l^i is the Hamiltonian of the isolated lead.

By using the nearest neighbor tight-binding model, we will only need the Green's function between sites in the first column of the lead that attaches to the central device.

In this subsection, we focus on the comparison of three methods to calculate the self energy of lead.

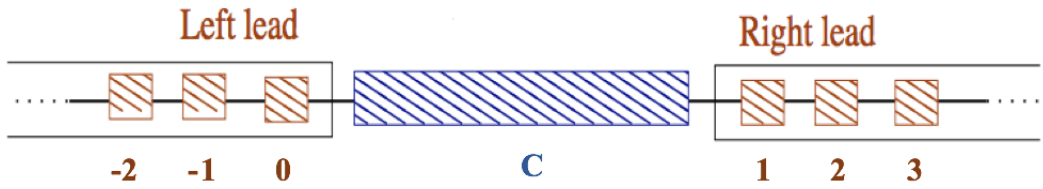

FIGURE 4.4: A schematic view of the model where AGNR and leads are sketched with discrete unit cells specified by integer numbers.

First method

Here, we follow the method introduced by [31] where two leads (left and right) and AGNR are sketched with discrete unit cells depicted in Fig. (4.4). We label the unit cells in the left lead as 0, -1, -2, ... and in the right lead as 1, 2, 3, ... and so on. The central device between two leads is labeled by C.

In the following description, we evaluate the self-energy corresponding to the right leads and then we could determine the self-energy for the left lead in the same way.

Using Eq. (4.18), we write the matrix representation of $E + i\eta - H_l$ in a block tridiagonal form as

$$\begin{pmatrix} (E+i\eta)I - H_{1,1} & H_{1,2} & 0 & 0 & \cdots \\ H_{1,2}^{\dagger} & (E+i\eta)I - H_{2,2} & H_{2,3} & 0 & \cdots \\ 0 & H_{2,3}^{\dagger} & (E+i\eta)I - H_{3,3} & H_{3,4} & \cdots \\ \vdots & 0 & H_{3,4}^{\dagger} & (E+i\eta)I - H_{4,4} & \ddots \\ & \vdots & \vdots & \ddots & \ddots \end{pmatrix}, \quad (4.19)$$

where, $H_{i,i}$ are the Hamiltonian elements of the unit cells and $H_{i,j}$ describe the transfer matrix between nearest neighbor unit cells.

By partitioning the total Green's function matrix, g in a similar way we write Eq. (4.18) as

$$(E+i\eta)I - \begin{pmatrix} H_{1,1} & H_{1,2} & 0 & 0 & \cdots \\ H_{1,2}^{\dagger} & H_{2,2} & H_{2,3} & 0 & \cdots \\ 0 & H_{2,3}^{\dagger} & H_{3,3} & H_{3,4} & \cdots \\ \vdots & 0 & H_{3,4}^{\dagger} & H_{4,4} & \ddots \\ & \vdots & \vdots & \ddots & \ddots \end{pmatrix} \cdot \begin{pmatrix} g_{1,1} & g_{1,2} & g_{1,3} & g_{1,4} & \cdots \\ g_{2,1} & g_{2,2} & g_{2,3} & g_{2,4} & \cdots \\ g_{3,1} & g_{3,2} & g_{3,3} & g_{3,4} & \cdots \\ g_{4,1} & g_{4,2} & g_{4,3} & g_{4,4} & \cdots \\ \vdots & \vdots & \vdots & \vdots & \ddots \end{pmatrix} = I, \quad (4.20)$$

where, we assume $H_{1,1} = H_{2,2} = H_{3,3} = \cdots$, and $H_{1,2} = H_{2,3} = H_{3,4} = \cdots$.

From Eq. (4.20), we write a set of equations for the unit cells as

$$\begin{aligned}
[(E + i\eta)I - H_{1,1}]\, g_{1,1} &= I + H_{1,2}\, g_{2,1}\,, \\
[(E + i\eta)I - H_{1,1}]\, g_{2,1} &= H_{1,2}^{\dagger}\, g_{1,1} + H_{1,2}\, g_{3,1}\,, \\
[(E + i\eta)I - H_{1,1}]\, g_{3,1} &= H_{1,2}^{\dagger}\, g_{2,1} + H_{1,2}\, g_{4,1}\,, \\
&\vdots \\
[(E + i\eta)I - H_{1,1}]\, g_{n,1} &= H_{1,2}^{\dagger}\, g_{n-1,1} + H_{1,2}\, g_{n+1,1}, \quad (n \geq 2).
\end{aligned} \tag{4.21}$$

By defining

$$\begin{aligned}
t_0 &= [(E + i\eta)I - H_{1,1}]^{-1}\, H_{1,2}^{\dagger}\,, \\
\tilde{t}_0 &= [(E + i\eta)I - H_{1,1}]^{-1}\, H_{1,2}\,,
\end{aligned} \tag{4.22}$$

the general expression for $g_{n,1}$ is

$$g_{n,1} = t_0\, g_{n-1,1} + \tilde{t}_0\, g_{n+1,1}. \tag{4.23}$$

Substituting $g_{n,1}$ into the expression of $g_{n-1,1}$ and $g_{n+1,1}$, we rewrite

$$g_{n,1} = t_1\, g_{n-2,1} + \tilde{t}_1\, g_{n+2,1} \quad (n \geq 3). \tag{4.24}$$

This process can be continued and repeated iteratively. After ith-iteration, we will have

$$g_{n,1} = t_i\, g_{n-2^i,1} + \tilde{t}_i\, g_{n+2^i,1} \quad (n \geq 3^i), \tag{4.25}$$

where

$$\begin{aligned}
t_i &= (I - t_{i-1}\, \tilde{t}_{i-1} - \tilde{t}_{i-1}\, t_{i-1})^{-1} t_{i-1}^2\,, \\
\tilde{t}_i &= (I - t_{i-1}\, \tilde{t}_{i-1} - \tilde{t}_{i-1}\, t_{i-1})^{-1} \tilde{t}_{i-1}^2\,.
\end{aligned} \tag{4.26}$$

The iteration continues until $t_i, \tilde{t}_i \leq \delta$ where δ is an arbitrary small number. Then, we determine the Green's function of a unit cell in terms of the Green's function of

the following or preceding unit cell by using Eq. (4.25) as

$$g_{2,1} = T\, g_{1,1}\,, \tag{4.27}$$

and

$$g_{1,1} = \tilde{T}\, g_{2,1}. \tag{4.28}$$

Here, T is defined as the transfer matrix

$$\begin{aligned} T &= (t_0 + \tilde{t}_0\, t_1 + \tilde{t}_0\, \tilde{t}_1\, t_2 + \cdots + \tilde{t}_0\, \tilde{t}_1\, t_2 \cdots t_n)\,, \\ \tilde{T} &= (\tilde{t}_0 + t_0\, \tilde{t}_1 + t_0\, t_1\, \tilde{t}_2 + \cdots + t_0\, t_1\, \tilde{t}_2 \cdots \tilde{t}_n)\,. \end{aligned} \tag{4.29}$$

After some algebraic calculations, the surface Green's function of the right lead, $g_{1,1}$ can be obtained from Eq. (4.21) as

$$g_{1,1} = [(E + i\eta)I - H_{1,1} - H_{1,2}T]^{-1}. \tag{4.30}$$

The surface Green's function of the left lead can be calculated in the same manner. Finally, the surface Green's function of left and right lead can be written as

$$g^{L}_{0,0} = [(E + i\eta)I - H_{1,1} - H^{\dagger}_{-1,0}\, \tilde{T}]^{-1}\,, \tag{4.31}$$

$$g^{R}_{1,1} = [(E + i\eta)I - H_{1,1} - H_{1,2}T]^{-1}. \tag{4.32}$$

Finally, we express the self-energies of two leads as

$$\begin{aligned} \Sigma_L &= H^{\dagger}_{0,C}\, g^{L}_{0,0}\, H_{0,C} \\ \Sigma_R &= H_{C,1}\, g^{R}_{1,1}\, H^{\dagger}_{C,1}, \end{aligned} \tag{4.33}$$

where $H_{C,1}$ is the central device to the right lead and $H_{0,C}$ is left lead to the central device transfer matrices, respectively [71].

Second method

We will briefly explain the method which was first derived in Ref. [72] to obtain the surface Green's function [25, 73]. From Eq. (4.19), we write the matrix representation of $E + i\eta - H_l$ as

$$(E + i\eta)I - H_l = \begin{pmatrix} d & -A & 0 & 0 & \cdots \\ -B & D & -A & 0 & \cdots \\ 0 & -B & D & -A & \cdots \\ \vdots & 0 & -B & D & \ddots \\ & \vdots & \vdots & \ddots & \ddots \end{pmatrix}, \tag{4.34}$$

where d , D , A , B are all $4N_W \times 4N_W$ matrices. The matrix D describe an isolated unit cell in the lead, while matrices A and B represent the hopping parameters between neighboring unit cells. The matrix d is equal to matrix D, but it just represents the first unit cell at the lead's surface and therefore, is shown by a separate notation. Then we write the partitioned total Green's function g as

$$\begin{pmatrix} d & -A & 0 & 0 & \cdots \\ -B & D & -A & 0 & \cdots \\ 0 & -B & D & -A & \cdots \\ \vdots & 0 & -B & D & \ddots \\ & \vdots & \vdots & \ddots & \ddots \end{pmatrix} . \begin{pmatrix} g_{1,1} & g_{1,2} & g_{1,3} & g_{1,4} & \cdots \\ g_{2,1} & g_{2,2} & g_{2,3} & g_{2,4} & \cdots \\ g_{3,1} & g_{3,2} & g_{3,3} & g_{3,4} & \cdots \\ g_{4,1} & g_{4,2} & g_{4,3} & g_{4,4} & \cdots \\ \vdots & \vdots & \vdots & \vdots & \ddots \end{pmatrix} = I. \tag{4.35}$$

Here, we are interested in the surface Green's function which is given by $g_{1,1}$. By calculating the first column of the matrix product in Eq. (4.35), we obtain the following (infinite) set of equations for $g_{1,1}$ as

$$d\, g_{1,1} = 1 + A\, g_{2,1}, \tag{4.36}$$

and

$$D\, g_{p,1} = B\, g_{p-1,1} + A\, g_{p+1,1} \quad (p \geq 2). \tag{4.37}$$

In order to calculate the surface Green's function, $g_{1,1}$ we need to know all matrices $g_{p,1}$ with $p \geq 2$. By using Eq. (4.37), we express $g_{p,1}$ with even indices $p = 2r (r = 1, 2, ...)$, as a function of Green's function with odd indices

$$g_{2r,1} = D^{-1} B\, g_{2r-1,1} + D^{-1} A\, g_{2r+1,1}. \tag{4.38}$$

By inserting Eq. (4.38) into Eqs. (4.36) and (4.37), we obtain $g_{1,1}$ as a function of only $g_{p,1}$ with p odd

$$(d - AD^{-1}B)\, g_{1,1} = 1 + (AD^{-1}A)\, g_{3,1}, \tag{4.39}$$

$$(D - AD^{-1}B - BD^{-1}A)\, g_{2r+1,1} = (BD^{-1}B)\, g_{2r-1,1} + (AD^{-1}A)\, g_{2r+3,1}. \tag{4.40}$$

By comparing above equations with Eqs. (4.36) and (4.37), one can see that they have exactly the same form if we define the renormalized matrices as

$$d' = d - AD^{-1}B, \tag{4.41}$$

$$D' = D - AD^{-1}B - BD^{-1}A, \tag{4.42}$$

$$A' = AD^{-1}A, \tag{4.43}$$

$$B' = BD^{-1}B, \tag{4.44}$$

$$g'_{r,1} = g_{2r-1,1}, \;\; r = 2, 3, ... \tag{4.45}$$

We iterate the previous procedure on the renormalized equations over and over again. This procedure can be physically interpreted as: Each layer is composed of single unit cells and after the first iteration, the lead is seen as a two unit cell, with renormalized interaction matrices A' and B' between neighboring unit cells. By each iteration, the number of unit cells is doubled. After iteration n, we will find a relation for the surface Green's function as

$$d_n\, g_{1,1} = 1 + A_n\, g_{2^n+1,1}. \tag{4.46}$$

For a sufficiently large number of iteration, n the effective interaction A_n will become considerably small and then the surface Green's function can be written approximately by

$$g_{1,1} \approx d_n^{-1}. \tag{4.47}$$

Once we have the surface Green's function, the self-energy of leads can be obtained using the Eq. (4.33).

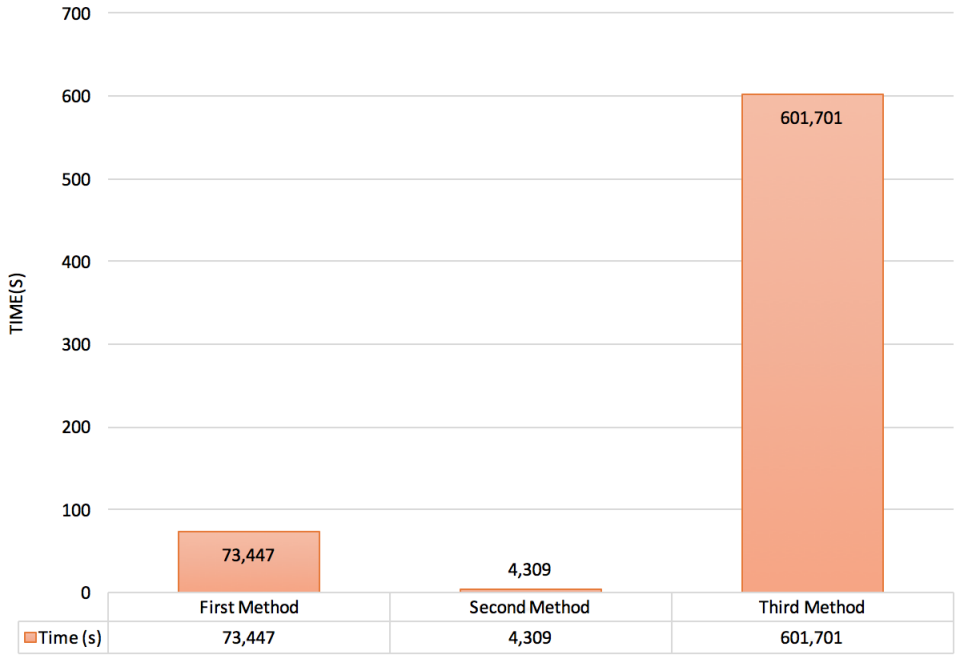

FIGURE 4.5: Time comparison of three methods to calculate the self-energy.The second method is more efficient and very faster than the two other methods.

Third method

In this method, we consider the first unit cell of the lead (for example unit cell 1 in the Fig. (4.4)) as an Identity matrix, $g^{L}_{1,1} = I$ and then by using the following relation

$$g^{L}_{j,j} = [(E + i\eta)I - H_{1,1} - H^{\dagger}_{1,2}.g^{L}_{j-1,j-1}.H_{1,2}]^{-1}, \quad (j, 2, ..., N). \tag{4.48}$$

the Green's function of the next unit cells can be calculated.

We iterate the procedure until it converges at, N (the iteration number). The final $g^{L}_{N,N}$ is considered as the surface Green's function of the left lead. The same procedure can be done by using the following iteration relation to obtain the surface Green's function of the right lead

$$g^{R}_{j,j} = [(E + i\eta)I - H_{1,1} - H_{1,2}.g^{R}_{j-1,j-1}.H^{\dagger}_{1,2}]^{-1}, \quad (j, 2, ..., N). \tag{4.49}$$

where again we assume that $g^{R}_{1,1} = I$. As such by having the surface Green's functions, the self-energy of leads can be obtained by Eq. (4.33).

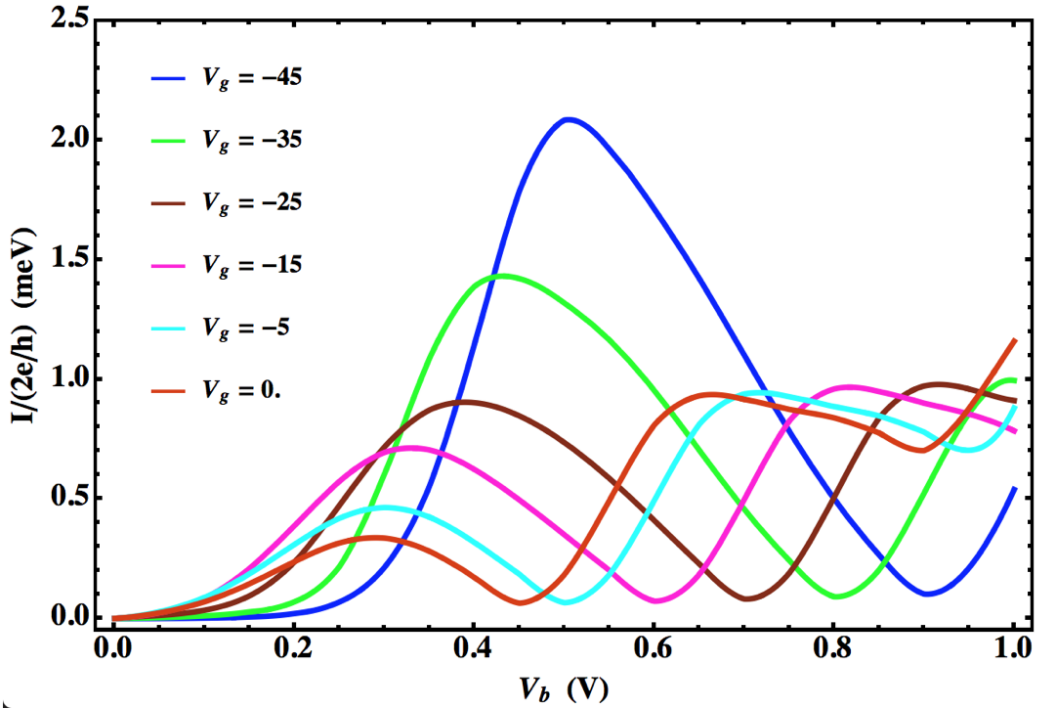

FIGURE 4.6: Current-Voltage characteristics as a function of bias voltage V_b at fixed gate voltages at T = 300K for AGNR/$(hBN)_3$/AGNR resonant tunneling transistor with W = 7.6nm and L = 6.8nm.

Comparison of methods

We have compared all three methods based on time of calculation of the self-energies for following fixed parameters: V_g = –45 V, V_b = 0.5 V, ε_C = 0 eV, T_{C-C} = 2.64 eV, N = 62, E = 0.2 eV and $\eta = 10^{-5}$. As the results shown in Fig. (4.5), the second method is more efficient and very faster than other two methods. Therefore, this method is used to simulate of the device in the Section 3.2.2.

4.3 Results

Figure (4.6) shows the I-V characteristics for the AGNR/$(hBN)_3$/AGNR resonant tunneling transistor with N = 62 (W = 7.6 nm) and M = 16 (L = 6.8 nm) at T = 300 K. The table. (4.1) represents the tight-binding parameters used in this simulation [74, 75]. The inter-layer distance between AGNR and hBN layers is 0.36 nm, the inter-layer distance between the hBN layers is 0.33 nm, and the relative dielectric constant of the insulator is taken to be 3.9.

In this study, we are interested in the effect of uniaxial strain on the current-voltage characteristics of the device. We assume that the uniaxial strain applied on

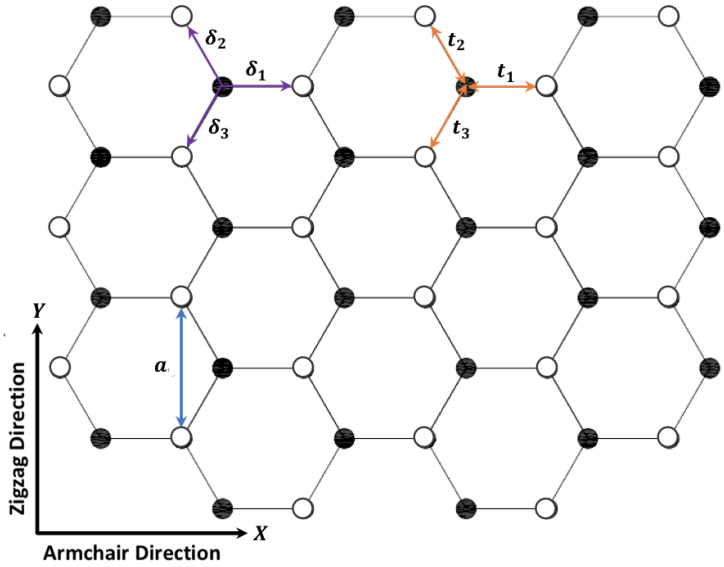

FIGURE 4.7: Schematic geometry of the armchair nanoribbon. The X direction is along the Armchair edge, while the Y-axes is along the zigzag edge. The distance between the nearest-neighbors are demonstrated by δ_i, while t_i show the hopping between nearest sites. By applying strain, these distances are changed depends on the direction of the strain which lead to change the hopping parameters. a is the lattice constant.

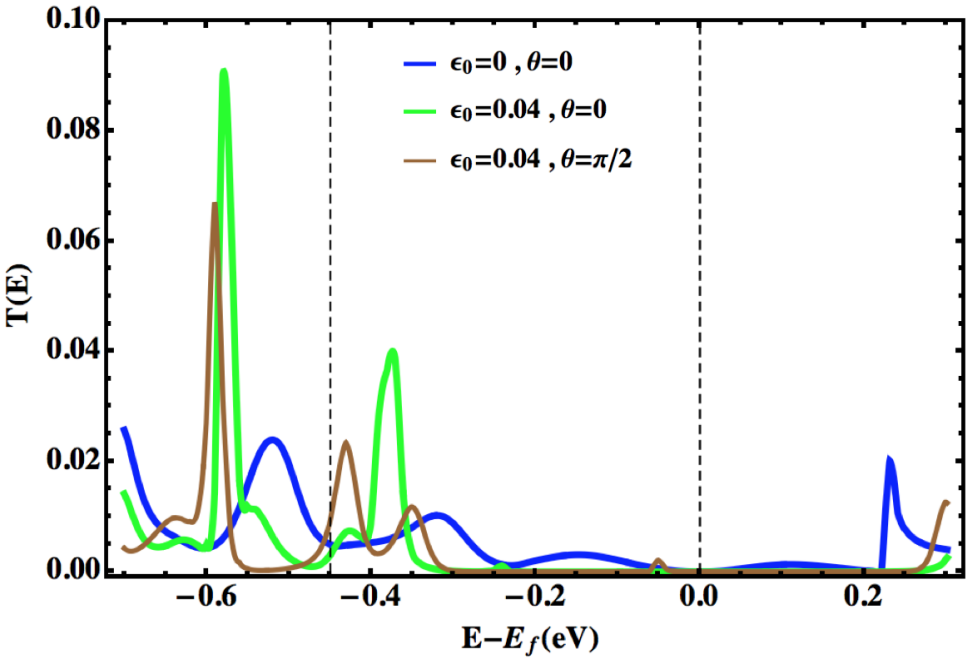

FIGURE 4.8: (Color online) The transmission function as a function of energy. The dashed black lines show the energy window determined by the Dirac points of two electrodes for $\varepsilon_0 = 0.04$ in armchair ($\vartheta = \pi/2$) and zigzag ($\vartheta = 0$) directions.

TABLE 4.1: The nearest-neighbor tight-binding parameters used in this paper [74, 75]

on-site energies	intra-layer hopping	inter-layer hopping
$E_C = 0\,eV$	$t_{C-C} = 2.64\,eV$	$t_{B-N} = 0.6\,eV$
$E_B = 3.34\,eV$	$t_{B-N} = 2.79\,eV$	$t_{C-B} = 0.43\,eV$
$E_N = -1.4\,eV$		$t_{C-N} = 0.43\,eV$

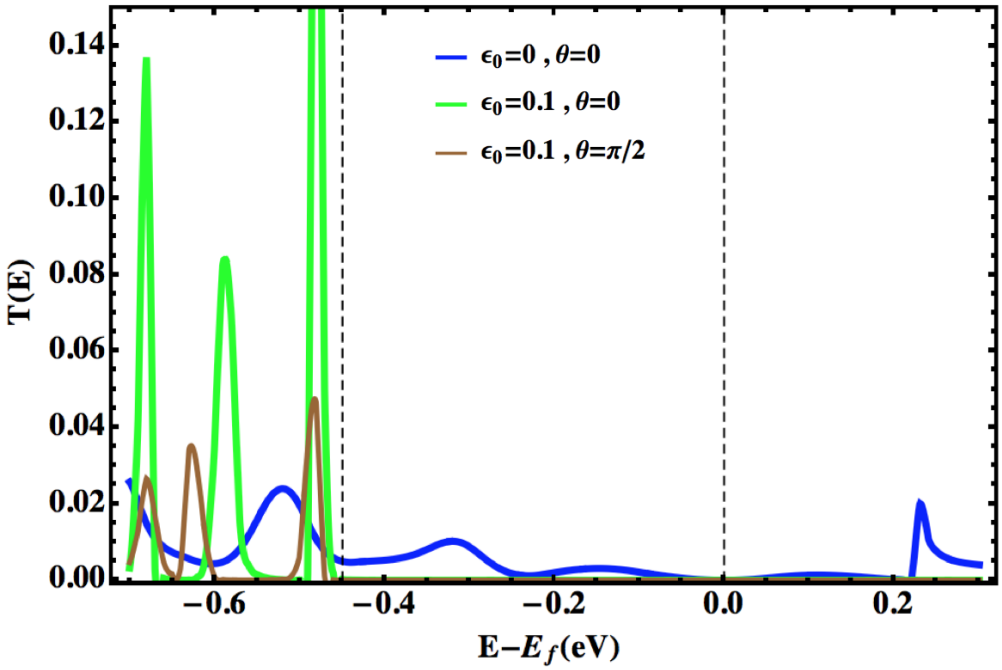

FIGURE 4.9: (Color online) The transmission function as a function of energy. The dashed black lines show the energy window determined by the Dirac points of two electrodes for $\varepsilon_0 = 0.1$ in armchair ($\vartheta = \pi/2$) and zigzag ($\vartheta = 0$) directions.

our multilayer device is the same in each layer. It means that all graphene and hBN layers are in the same tension and this tension does not affect the distance between inter-layer atoms and inter-layer hopping parameters. Fig. (4.7) shows a schematic geometry of armchair nanoribbon. The Y direction is along the zigzag edge, while the X -axes are along the armchair edge. The distance between the nearest-neighbors are demonstrated by $\boldsymbol{\delta_i}$, while t_i shows the hopping between nearest sites. By applying strain, these distances change depending on the direction of the tension which leads to change the hopping parameters, see Section 3.5 for more details. Using modified hopping parameters in our simulation yields to the new interesting results explained below.

In Fig. (4.8), the transmission function is plotted for different strain modulus applied in both zigzag and armchair directions for $V_g = -45(V)$ and $V_b = 0.45(V)$. The

current is calculated by integrating the transmission function in the energy window bounded by the electrode's Fermi levels, Eq. (4.12). The dashed black lines in Fig. (4.8) show the bounds of the energy window such that the main contribution to the current comes from the main peaks in this region. The transmission functions show the electrons at E = 0 eV see a stronger barrier when tunneling between AGNR layers. For the relatively small strain $\varepsilon_0 = 0.04$ in zigzag direction ($\vartheta = 0$) the main peak in Fig. (4.8) is enhancing but becoming sharper which leads to a smaller current. The behavior of the transmission function for the applied strain in the armchair direction ($\vartheta = \pi/2$) is generally the same: peaks are enhancing and becoming sharper. By increasing the strain modulus (See Fig. (4.9) for $\varepsilon_0 = 0.1$) the main peaks in the active energy regions in both directions collapse due to localizing the P_z orbitals of the atoms in the honeycomb lattice.

The resultant I-V characteristic of the device for different strain modulus applied in the zigzag direction, $\vartheta = 0$ and armchair direction, $\vartheta = \pi/2$ are plotted in Fig. (4.10) and Fig. (4.11), respectively. See Appendix B for the Mathematica code which is written to obtain I-V characteristics shown in Figs. (4.10) and (4.11). Our results show that the applied strain in the $\vartheta = 0$ results in narrowing the main peak of current simultaneously decrease the maximum amount of the current. Also, the next smaller peak becomes closer to the main peak and collapse to zero rapidly. While applying strain in the armchair direction yields widening the main peak of current over a bigger region in the bias voltage domain, although the maximum of the current still decreases. The current decreasing faster when the same strain applied in the armchair direction rather than the zigzag direction.

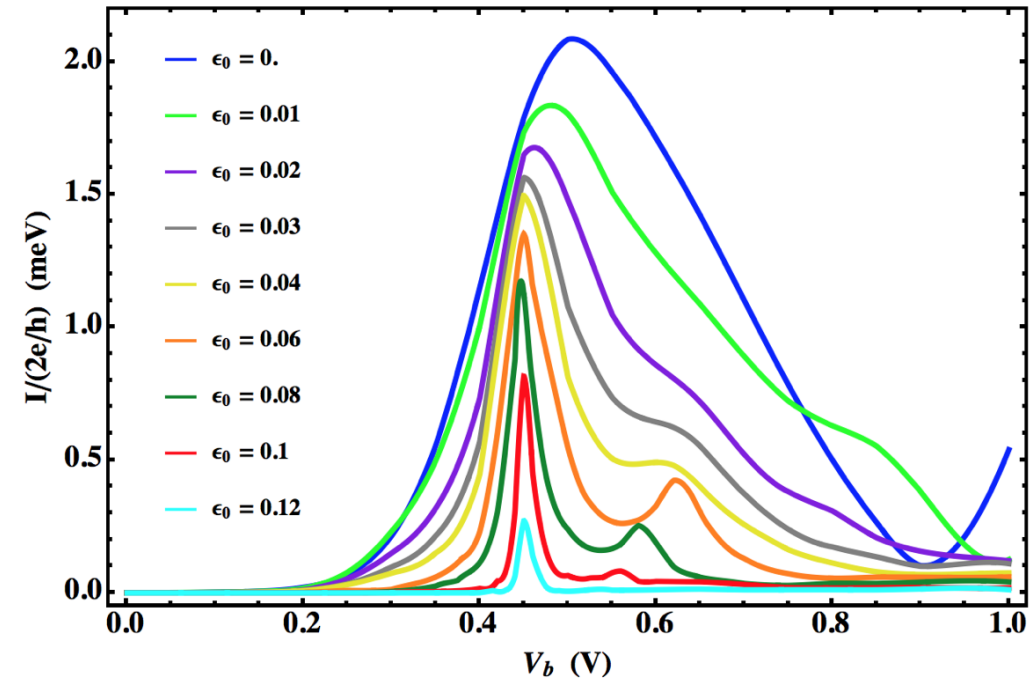

FIGURE 4.10: (Color online) The current-voltage characteristic of the device under the uniaxial strain in zigzag direction($\vartheta = 0$). The gate voltage is -45 V. Increasing the strain modulus causes decreasing the current.

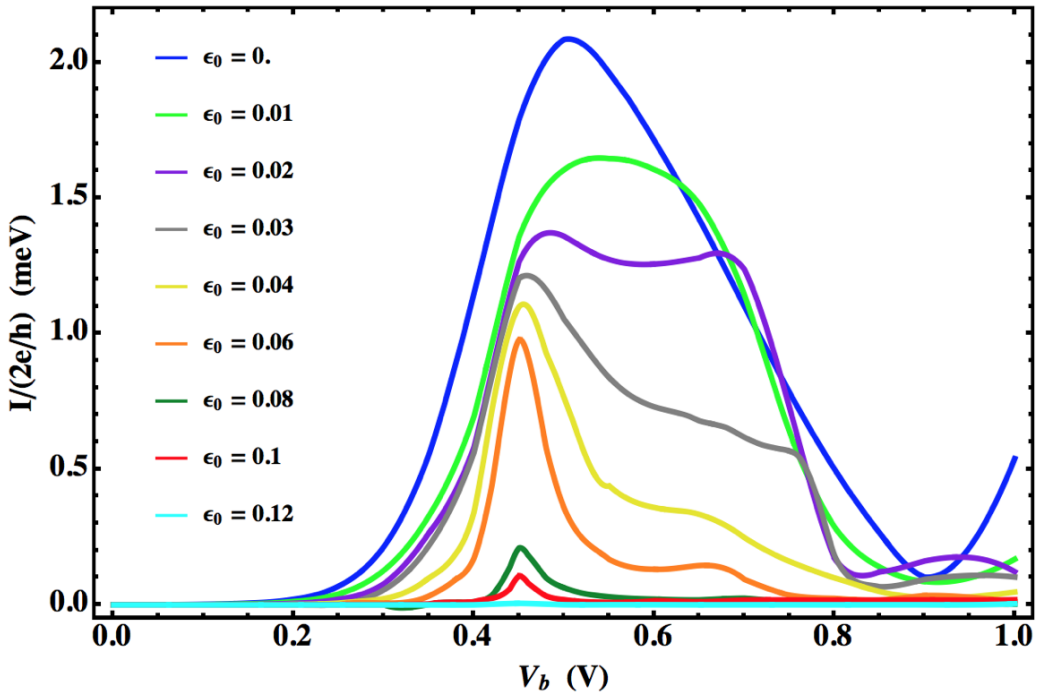

FIGURE 4.11: (Color online) The current-voltage characteristic of the device under the uniaxial strain in armchair direction($\vartheta = \pi/2$). The gate voltage is -45 V. Increasing the strain modulus causes decreasing the current.

Chapter 5

Conclusion

Although graphene was discovered only in 2004 experimentally, it has been theoretically investigated for over 60 years now. Today, graphene and its heterostructures are a rapidly growing field of theoretical and experimental physics. Due to its extremely high mobility of the charge carriers, graphene is a promising candidate for future technological applications, such as transistors.

The device considered in this thesis composed of a few layers of hBN sandwiched between two metallic armchair graphene nanoribbon (AGNR) electrodes, with the bottom and top graphene electrodes acting as the source and the drain, respectively. The hBN layers act as a barrier between two metallic electrodes and form a vertical tunneling transistor. In such devices, resonant tunneling occurs if the applied gate voltage aligns the Dirac points of the top and bottom graphene electrodes.

In order to simulate the I-V characteristic of such AGNR-hBN-AGNR multilayer heterostructure device, the nonequilibrium Green's function approach can be employed due to its favorable properties. In Chapter 2, relevant theoretical and numerical techniques required for the device simulation, e.g., Landauer-Büttiker formalism, tight-binding model, and Green's function formalism were explained. The recursive method has been used to calculate the device Green's function.

In Chapter 3, the graphene lattice and its peculiar properties in the context of the nearest-neighbor tight-binding model were described. Furthermore, it was investigated how the applied strain can modify the lattice structure and therefore distort the band structure of graphene. Studies reveals that strain larger than $\approx 20\%$ can open a gap in the graphene bands which is not favorable in our studies. Therefore, we considered the strain less than the gap threshold in this thesis.

In the course of this thesis, the effect of mechanically applied strain on the multilayer heterostructure transistor was investigated theoretically. Applying strain on the

device deforms the Dirac points of the graphene layers (electrodes) thus modifying the transport properties of the device.

In Chapter 4, the uniaxial strain was applied in the armchair and zigzag direction of the nanoribbons, changing the intra-layer atomic distances in all layers in the same form. For simplicity, it was assumed that inter-layer distances and consequently inter-layer hopping parameters are not all affected by the tension. By using the tight-binding model and nonequilibrium Green's function formalism the current-voltage characteristic of the device was calculated in the presence of the uniaxial strain. The results demonstrated that the strain decreased the amount of the current in both cases; however, the quantitative behavior of the I-V plot turned out to be different for the strain in different directions. The current collapsed more rapidly when the strain was applied in the armchair direction.

The uniaxial strain effect on the chosen device enables control the current by applying the relevant tension to the layers and obtaining (designing) the desired I-V characteristics. This property may offer attractive applications in NEMS devices.

The results obtained in this work suggest that by considering the effect of inter-layer hopping parameters changes in simulations, applying different tensions in different directions (by varying ϑ), and comparing them with the first principle calculations will provide deeper insights and valuable guidelines for future theoretical and experimental investigations of strain effect on heterostructure devices.

Appendix A

Resonant tunneling

A.1 Introduction

Recently, the increasing demand for electronic devices with higher computing power, smaller dimensions, and lower power consumption leads to down scale the semiconductor components to length scales in which the electrical device characteristics are dominated by quantum-mechanical effects. The quantum-mechanical tunneling of charge carriers through regions that are classically forbidden is one of the most interesting quantum effects. Specially, resonant tunneling in semiconductor structures have been advertised for both fundamental research and applications in high speed electronics. The typical semiconductors such as GaAs with their excellent crystalline quality and high mobility [76, 77] exhibit resonant tunneling. Recently, graphene has attracted many attention due to its higher mobility [5]. Resonant tunneling is exhibited in the new devices using the graphene-based van der Waals heterostructures.

In this appendix, we give a brief physical description of quantum mechanical tunneling and tunneling in semiconductor devices which is necessary to get deeper insight in the graphene based heterostructure devices.

A.2 Quantum tunneling

Consider an electron with energy E in the left side of a one dimensional potential barrier, E_B in Fig. (A.1a). Classically, if E is greater than E_B, the electron passes over the barrier. If E is less than E_B, then the electron will be reflected from the barrier.

However quantum mechanically, electrons are treated as wavefunctions which do not end abruptly at a wall or barrier, but decay quickly, as the wavefunction and its derivative must be continuous at the barrier boundary [78]. If the barrier is thin

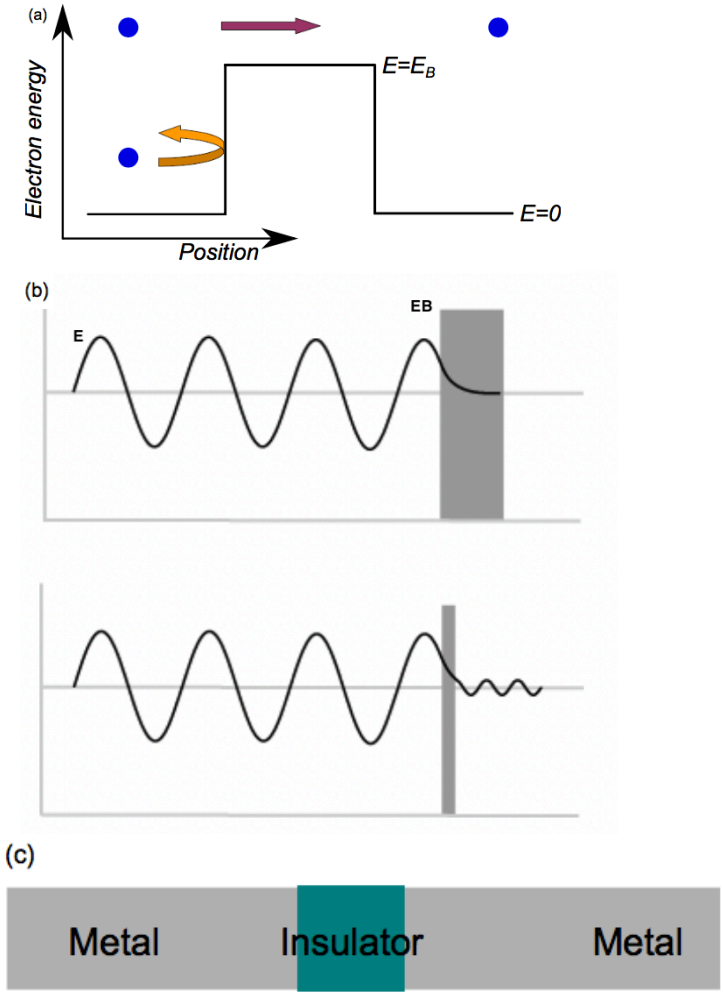

FIGURE A.1: (a) According to classical mechanics, an electron with the energy higher than the potential of barrier, E > E_B can passover the barrier, while the electrons with lower energy E < E_B will be reflected completely. (b) According to wave properties of particles in quantum mechanics, when an electron hits a barrier, the wavefunction of electron decays quickly. If the barrier is thin, then the electron can tunnel through the barrier and if the barrier is thick, the wave doesn't get past. (c) A metal-insulator-metal device can be considered as a tunneling barrier.

enough, then it is possible that an electron with energy less than the barrier's energy can tunnel through the barrier. This possibility goes to zero for wider barriers, Fig. (A.1b). These barriers can practically constructed by sandwiching an insulator with a large band gap between two metals, Fig. (A.1c).

According to the Schrödinger's equation, a free particle can be expressed as a plane wave of the form

$$\psi(x) = A\,e^{i\,k\,x} + B\,e^{-i\,k\,x}, \quad k = \sqrt{\frac{2\,m\,E}{\hbar^2}}, \tag{A.1}$$

where E is the energy of the free particle. Now, consider a potential barrier of height, V_0 which divides the space to three different regions illustrated in Fig. (A.2). The time-independent Schrödinger's equation is

$$H\,\psi = \left[-\frac{\hbar^2}{2m}\frac{d^2}{dx^2} + V(x)\right]\,\psi = E\,\psi, \tag{A.2}$$

where V(x) is V_0 at region II and it is zero at regions I and III. One can solve the Schrödinger's equation in each region independently. If the energy of the particle is larger than V_0, the solutions are

$$\psi_I(x) \;= A_R\,e^{i\,k_0\,x} + A_L\,e^{-i\,k_0\,x}, \qquad (x < 0)],, \tag{A.3}$$

$$\psi_{II}(x) \;= B_R\,e^{i\,k_1\,x} + B_L\,e^{-i\,k_1\,x}, \quad (0 < x < a), \tag{A.4}$$

$$\psi_{III}(x) = C_R\,e^{i\,k_0\,x} + C_L\,e^{-i\,k_0\,x}, \qquad (x > 0), \tag{A.5}$$

where the coefficients A_L, B_L, C_L are constants of the waves moving toward the left direction in different regions, while the A_R, B_R, C_R are coefficients of the waves moving to the right direction. The wavenumber in each region is

$$k_0 \;= \sqrt{\frac{2\,m\,E}{\hbar^2}}, \qquad (x < 0 \text{ or } x > a), \tag{A.6}$$

$$k_1 \;= \sqrt{\frac{2\,m\,(E - V_0)}{\hbar^2}}, \quad (0 < x < a). \tag{A.7}$$

Since the plane wave of incoming particle incident from the left side, then $A_R = 1$. Also, the $C_L = 0$ because there is no particle coming from the right. The boundary conditions require that the wavefunction and its derivative to be continuous at the

barrier edges (x = 0 and x = a) which give rise to

$$1 + A_L = B_R + B_L\,, \tag{A.8}$$

$$i\,k_0\,(1 - A_L) = i\,k_1(B_R - B_L)\,, \tag{A.9}$$

$$B_R\,e^{i\,a\,k_1} + B_L\,e^{-i\,a\,k_1} = C_R\,e^{i\,a\,k_0}\,, \tag{A.10}$$

$$i\,k_1(B_R\,e^{i\,a\,k_1} - B_L\,e^{-i\,a\,k_1}) = i\,k_0\,C_R\,e^{i\,a\,k_0}\,. \tag{A.11}$$

By solving the above equations, one may find the reflection (A_L) and transmission (C_R) coefficients as follows

$$t := C_R = \frac{4\,k_0\,k_1\,e^{-i\,(k_0-k_1)}}{(k_0+k_1)^2 - e^{2\,i\,a\,k_1}(k_0-k_1)^2}\,, \tag{A.12}$$

$$r := A_L = \frac{(k_0^2 - k_1^2)\sin(a\,k_1)}{2\,i\,k_0\,k_1\cos(a\,k_1) + (k_0^2+k_1^2)\sin(a\,k_1)}\,. \tag{A.13}$$

So the tunneling probability for an electron of $E > V_0$ is

$$T := |t|^2 = \frac{1}{1 + \frac{V_0^2\,\sin^2(a\,k_1)}{4\,E\,(E-V_0)}}\,. \tag{A.14}$$

Then, the reflection probability is $R := |r|^2 = 1 - T$ is not zero for an electron with the energy higher than the barrier. This probability goes to zero as $E >> V_0$.

Now, if the electron energy E is less than V_0, the solution of the Schrödinger's equation in the region II will be

$$\psi_{II}(x) = B_R\,e^{\varkappa\,x} + B_L\,e^{-\varkappa\,x}\,, \quad (0 < x < a)\,, \tag{A.15}$$

which leads to a non-zero transmission probability

$$T = \frac{1}{1 + \frac{V_0^2\,\sin^2(a\,k_1)}{4\,E\,(V_0-E)}}\,. \tag{A.16}$$

Therefore, as we see from the Eq. (A.16), the probability of quantum tunneling depends on the thickness and height of the barrier, as well as the energy of the electron.

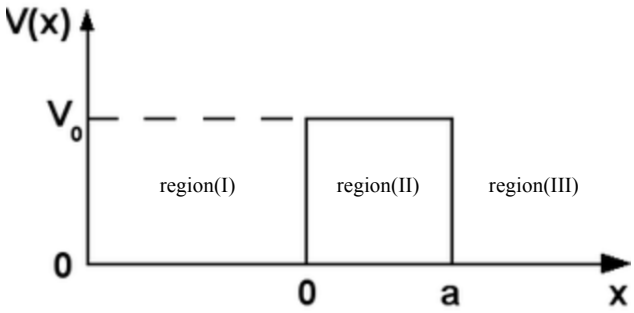

FIGURE A.2: A potential barrier of height, V_0 which divides the space to three different regions.

A.3 Tunneling in semiconductor devices

There are two possible ways for electrons to tunnel in different layers of the semiconducting devices. In the process known as direct tunneling, electrons tunnel between energetic states in different layers of the device which conserve the energy and momentum of electrons. On the other hand, electrons can tunnel between layers due to elastic or inelastic scattering events. Since, there are always some imperfections in semiconductor crystals, such as impurities or deformations in the lattice structure, the tunneling due to scattering is very common in such devices. The energy of electron is conserved in the elastic event, while its momentum changes during the collision. Both energy and momentum of electron change due to an inelastic scattering event. Generally, electron-phonon interactions are responsible for the most inelastic scattering events [79].

In1950s, tunneling was utilized in semiconductor devices [80] such as Esaki diodes inventing in 1957 [81]. In such tunneling devices, the current decreases by increasing the voltage. This phenomenon which is known as negative differential conductance (NDC), has attracted many attention for the generation of high-frequency electromagnetic waves. For instance, microwave generators were developed using the transferred electron diodes [82, 83, 84] based on n-type GaAs and InP. The strong NDC was exhibited in the semiconductor superlattices [85, 86] and double-barrier resonant tunneling diodes (DBRTDs) [87, 88, 89, 79] as well.

Here we briefly explain the tunneling mechanism through the simplest tunnel diode composed of two semiconductors. The semiconductors are doped oppositely to form an Esaki p – n junction. The left semiconductor which is doped with the acceptor impurities normally called p-type semiconductor. In this semiconductor, the states

close to the top of the valence band are empty and the Fermi level is inside the valence band. On the other side, the n-type semiconductor is doped with donor impurities. So, the Fermi level is above the band gap and in the conduction band.

A depletion layer is located between two doped semiconductors whose width depends on the amount of impurities added to the semiconductors. In the heavily doped semiconductors the depletion layer becomes very thin ($\sim$ 10 nm with carrier concentrations of $\approx 10^{19}\text{cm}^3$) which increases the probability of tunneling.

A typical current-voltage I-V characteristic of a tunneling device is plotted in Fig. (A.3a), with the NDC region shown in yellow. Here we explain the critical points (A-E) in the I-V characteristic [79]:

- **Point A**: When there is no bias voltage, the Fermi level of two semiconductors are aligned, and therefore there is no current flow. This is shown in Fig. (A.3b).
- **Point B**: By applying a small forward bias, the Fermi energy of the p-type semiconductor (left) shift with respect to the n-type one (right) and as a result electrons from the conduction band in the right side can tunnel through the junction to the valence band of left semiconductor, see Fig. (A.3c).
- **Point C**: By increasing the bias voltage the overlap between the available valence states (between E_F and E_V in the p-layer) and the filled conduction states (between E_F and E_C in the n-layer) becomes maximum at $V_b = V_{peak}$ and therefore the resonant peak is observed in the I-V characteristics. This is shown in Fig. (A.3d).
- **Point D**: For voltages larger than $V = V_{peak}$, the current reduces because the number of states available for tunneling decreases. In this case, the filled conductance states are in a higher level of energy with respect to the empty valence states, see Fig. (A.3e). In this region, increasing the applied bias voltage decreases the current and hence it is known as the negative differential conductance (NDC) region.
- **Point E**: The current decreases by increasing the voltage until the states are so energetically misaligned such that tunneling is not possible to occur, see Fig. (A.3f). Although, in this case, the electrons conduct over the barrier which leads to increasing the current.

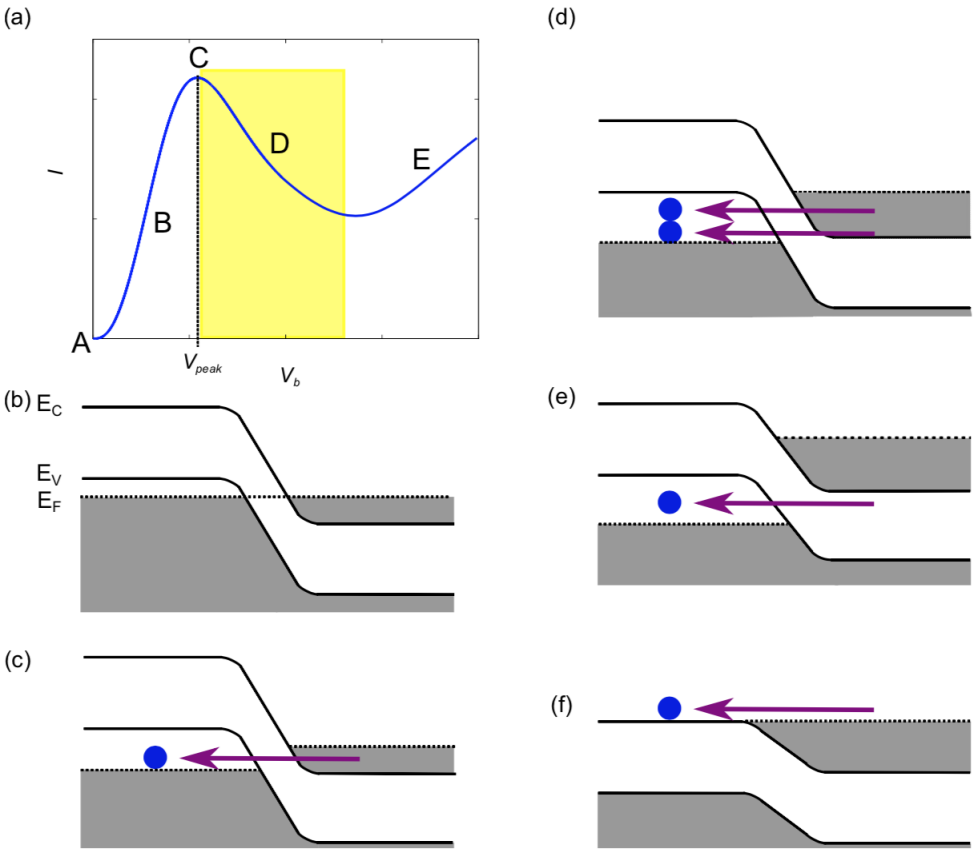

FIGURE A.3: (a) The general I-V characteristics of a tunnel diode, with the NDC region highlighted yellow. Points A-E mark bias voltages for which the band structure is plotted in (b-f). (b) The band structure of a tunnel diode, with a positively doped semiconductor on the left, negatively doped semiconductor on the right. The conduction band energy, E_C and valence band, E_V are shown, and filled states are colored grey. Here, the applied voltage is 0 V, i.e. point A in (a). Fermi levels, E_F , in the p and n regions are aligned and no current flows. (c) A small forward bias is applied and electrons in the conductance band of the n region will tunnel to the empty states in the valence band of the p region. This leads to a small tunnel current (point B). (d) A larger applied voltage leads to a large number of electrons in the n-region having the same energy as empty states in the p-region, thus giving a maximum tunnel current of the peak at C. (e) For $V_b > V_{peak}$, V_b energetically shifts the available tunneling and empty states such that the tunneling decreases and thus the current at point D is lower. (f) As the forward bias further increases, the tunnel current drops to zero, but electron-hole injection increases due to the lower potential barrier, point E [79].

Appendix B

Mathematica Code

We have provided here the Mathematica code which describes the algorithm utilized to obtain I-V characteristics shown in Figs. (4.10) and (4.11).

General input parameters

eVg = –45; (* Gate voltage *)

μT = 0; (* Chemical potential of the top AGNR layer *)

k = 8.617342 * 10^{-5}; (* Boltzmann constant in eV/ K *)

T0 = 300; (* Temperature in K *)

Numerical precision

precision = 20; (* Numerical Precision *)

η = 10^{-5}; (* Small number added to the Hamiltonian *)

Lattice parameters without strain

aCC = 0.42; (* Carbon-Carbon distance in nanometer (nm) *)

TCC = –2.64; (* Intra-layer Carbon-Carbon transfer energy in eV *)

TBN = –2.79; (* Intra-layer Boron-Nitride transfer energy in eV *)

tBN = –0.6; (* Inter-layer Boron-Nitride transfer energy in eV: not affected under strain *)

tCB = –0.43; (* Inter-layer Carbon-Boron transfer energy in eV: not affected under strain *)

tCN = –0.43; (* Inter-layer Carbon-Nitride transfer energy in eV: not affected under strain *)

εC = 0; (* Carbon on-site potential energy in eV *)

εB = 3.34; (* Boron on-site potential energy in eV *)

εN = –1.4; (* Nitride on-site potential energy in eV *)

Strain matrix inputs; Eq. 3.44

```
ϑ = π/2; (* Direction of the strain *)
ε0 = 0.02; (* Modulus of the strain *)
α = 3.37; (* The decay rate of transfer energies, see Eq. (3.47) *)
σ = 0.165; (* Poisson's ratio for graphene *)
strain = ε0 {{Cos[ϑ]^2 − σSin[ϑ]^2, (1 + σ)Sin[ϑ] Cos[ϑ]},
  {(1 + σ)Sin[ϑ] Cos[ϑ], Sin[ϑ]^2 − σ Cos[ϑ]^2}}; (* strain matrix *)
```

Vectors connecting site A to the nearest neighbor sites B

```
δ[1] = aCC{1, 0}; (* no strain; See Fig. 4.7 *)
δ[2] = aCC {-1/2, √3/2}; (* no strain; See Fig. 4.7 *)
δ[3] = aCC {-1/2, -√3/2}; (* no strain; See Fig. 4.7 *)
δs[i_]:=δ[i] + strain.δ[i]//Simplify; (* vectors under the applied strain *)
```

Transfer energies under strain

$$\texttt{tsCC[i\_]:=TCC Exp}\left[-\alpha\left(\frac{\texttt{Norm[δs[i]]}}{\texttt{aCC}}-1\right)\right]$$

$$\texttt{tsBN[i\_]:=TBN Exp}\left[-\alpha\left(\frac{\texttt{Norm[δs[i]]}}{\texttt{aCC}}-1\right)\right]$$

```
TCCs = tsCC[1];
TCCu = tsCC[2];
TCCd = tsCC[3];
TBNs = tsBN[1];
TBNu = tsBN[2];
TBNd = tsBN[3];
```

Dimensions of the device

```
M = 16; (* The number of unit cells *)
m = 31; (* The number of atoms in each slice of an unit cell (N_W) *)
Zo[m_]:=Table[0, {i, 1, m}, {j, 1, m}]; (* Zero matrix of (m × m) *)
Zop[p_, q_]:=Table[0, {i, 1, p, 1}, {j, 1, q, 1}]; (* Zero matrix of (p × q) *)
```

This procedure calculate the self energy of leads

```
SelfEnergy[ε_, V_]:=
```

```
Module[{ε1, K1, T12, T21, T23, T32, T34, T43, T41, T14, d, A,
F, B, nf, df, g11, Tdl, ΣLL, ΣRR, ΣL, ΣR, iteration},
ε1 = 10^-300.;
K1 = Table[If[i == j, (ε + Iη) - εC - V, 0], {i, 1, m}, {j, 1, m}];
T12 = Table[If[i == j, TCC, If[i == j + 1, TCC, 0], 0], {i, 1, m},
{j, 1, m}];
T21 = T12†;
T23 = Table[If[i == j, TCC, 0], {i, 1, m}, {j, 1, m}];
T32 = T23†;
T34 = Table[If[i == j, TCC, If[i + 1 == j, TCC, 0], 0], {i, 1, m},
{j, 1, m}];
T43 = T34†;
T41 = Table[If[i == j, TCC, 0], {i, 1, m}, {j, 1, m}];
T14 = T41†;
d[0] = ArrayFlatten[{{K1, T12, Zo[m], Zo[m]}, {T21, K1, T23, Zo[m]},
{Zo[m], T32, K1, T34}, {Zo[m], Zo[m], T43, K1}}];
A[0] = ArrayFlatten[{{Zo[m], Zo[m], Zo[m], Zo[m]},
{Zo[m], Zo[m], Zo[m], Zo[m]}, {Zo[m], Zo[m], Zo[m], Zo[m]},
{T41, Zo[m], Zo[m], Zo[m]}}];
F[0] = ArrayFlatten[{{K1, T12, Zo[m], Zo[m]}, {T21, K1, T23, Zo[m]},
{Zo[m], T32, K1, T34}, {Zo[m], Zo[m], T43, K1}}];
B[0] = A[0]†;
iteration[n_]:=(
Do[
d[i] = d[i - 1] - A[i - 1].Inverse[F[i - 1]].B[i - 1];
A[i] = A[i - 1].Inverse[F[i - 1]].A[i - 1];
B[i] = B[i - 1].Inverse[F[i - 1]].B[i - 1];
F[i] = F[i - 1] - A[i - 1].Inverse[F[i - 1]].B[i - 1]-
B[i - 1].Inverse[F[i - 1]].A[i - 1]
, {i, 1, n, 1}];
{A[n][[3m + 1, 1]], d[n]} );
nf = Catch[Do[ If[Abs[iteration[n][[1]]] ≤ ε1, Throw[n]],
{n, 1, 2000, 1} ]];
df = iteration[nf][[2]];
```

```
g11 = Inverse[df];
Tdl = ArrayFlatten[{{Zo[m], Zo[m], Zo[m], Zo[m]},
{Zo[m], Zo[m], Zo[m], Zo[m]}, {Zo[m], Zo[m], Zo[m], Zo[m]},
{T41, Zo[m], Zo[m], Zo[m]}}];
ΣLL = Tdl.g11.(Tdl)†;
ΣRR = Tdl.g11.(Tdl)†;
ΣL = Table[ΣLL[[i, j]], {i, 1, m}, {j, 1, m}];
ΣR = Table[ΣRR[[i, j]], {i, 3m + 1, 4m}, {j, 3m + 1, 4m}];
{g11, ΣLL, ΣRR, ΣL, ΣR}];
```

This function calculate the I-V characteristics:

```
FuncI[eVb_]:=
FuncI[eVb] =
Module[{V5, V4, V3, V2, V1, μB, h, s, H, t, T, Hu, Tu, tr, list, f},
```

Layers potential

```
V5 = (–0.01eVg – eVb);
V4 = 3/4(–0.01eVg – eVb);
V3 = 2/4(–0.01eVg – eVb);
V2 = 1/4(–0.01eVg – eVb);
V1 = 0;
μB = –eVb; (* Chemical potential of the bottom AGNR layer *)
```

Building the Hamiltonian of a unit cell; see Section 4.2.2

```
h[1][1, 1] = (εC + V1)IdentityMatrix[m];
h[1][2, 2] = (εB + V2)IdentityMatrix[m];
h[1][3, 3] = (εN + V3)IdentityMatrix[m];
h[1][4, 4] = (εB + V4)IdentityMatrix[m];
h[1][5, 5] = (εC + V5)IdentityMatrix[m];

h[2][1, 1] = (εC + V1)IdentityMatrix[m];
h[2][2, 2] = (εN + V2)IdentityMatrix[m];
h[2][3, 3] = (εB + V3)IdentityMatrix[m];
h[2][4, 4] = (εN + V4)IdentityMatrix[m];
```

```
h[2][5, 5] = (εC + V5)IdentityMatrix[m];

h[3][1, 1] = (εC + V1)IdentityMatrix[m];
h[3][2, 2] = (εB + V2)IdentityMatrix[m];
h[3][3, 3] = (εN + V3)IdentityMatrix[m];
h[3][4, 4] = (εB + V4)IdentityMatrix[m];
h[3][5, 5] = (εC + V5)IdentityMatrix[m];

h[4][1, 1] = (εC + V1)IdentityMatrix[m];
h[4][2, 2] = (εN + V2)IdentityMatrix[m];
h[4][3, 3] = (εB + V3)IdentityMatrix[m];
h[4][4, 4] = (εN + V4)IdentityMatrix[m];
h[4][5, 5] = (εC + V5)IdentityMatrix[m];

s[1][1, 2] = tCBIdentityMatrix[m];
s[1][2, 3] = tBNIdentityMatrix[m];
s[1][3, 4] = tBNIdentityMatrix[m];
s[1][4, 5] = tCBIdentityMatrix[m];

s[2][1, 2] = Zo[m];
s[2][2, 3] = Zo[m];
s[2][3, 4] = Zo[m];
s[2][4, 5] = Zo[m];

s[3][1, 2] = tCBIdentityMatrix[m];
s[3][2, 3] = tBNIdentityMatrix[m];
s[3][3, 4] = tBNIdentityMatrix[m];
s[3][4, 5] = tCBIdentityMatrix[m];

s[4][1, 2] = Zo[m];
s[4][2, 3] = Zo[m];
s[4][3, 4] = Zo[m];
s[4][4, 5] = Zo[m];
```

```
H[1] = ArrayFlatten[{{h[1][1, 1], s[1][1, 2], Zo[m], Zo[m], Zo[m]},
{s[1][1, 2]†, h[1][2, 2], s[1][2, 3], Zo[m], Zo[m]} ,
{Zo[m], s[1][2, 3]†, h[1][3, 3], s[1][3, 4], Zo[m]} ,
{Zo[m], Zo[m], s[1][3, 4]†, h[1][4, 4], s[1][4, 5]} ,
{Zo[m], Zo[m], Zo[m], s[1][4, 5]†, h[1][5, 5]}}] ;

H[2] = ArrayFlatten[{{h[2][1, 1], s[2][1, 2], Zo[m], Zo[m], Zo[m]},
{s[2][1, 2]†, h[2][2, 2], s[2][2, 3], Zo[m], Zo[m]} ,
{Zo[m], s[2][2, 3]†, h[2][3, 3], s[2][3, 4], Zo[m]} ,
{Zo[m], Zo[m], s[2][3, 4]†, h[2][4, 4], s[2][4, 5]} ,
{Zo[m], Zo[m], Zo[m], s[2][4, 5]†, h[2][5, 5]}}] ;

H[3] = ArrayFlatten[{{h[3][1, 1], s[3][1, 2], Zo[m], Zo[m], Zo[m]},
{s[3][1, 2]†, h[3][2, 2], s[3][2, 3], Zo[m], Zo[m]} ,
{Zo[m], s[3][2, 3]†, h[3][3, 3], s[3][3, 4], Zo[m]} ,
{Zo[m], Zo[m], s[3][3, 4]†, h[3][4, 4], s[3][4, 5]} ,
{Zo[m], Zo[m], Zo[m], s[3][4, 5]†, h[3][5, 5]}}] ;

H[4] = ArrayFlatten[{{h[4][1, 1], s[4][1, 2], Zo[m], Zo[m], Zo[m]},
{s[4][1, 2]†, h[4][2, 2], s[4][2, 3], Zo[m], Zo[m]} ,
{Zo[m], s[4][2, 3]†, h[4][3, 3], s[4][3, 4], Zo[m]} ,
{Zo[m], Zo[m], s[4][3, 4]†, h[4][4, 4], s[4][4, 5]} ,
{Zo[m], Zo[m], Zo[m], s[4][4, 5]†, h[4][5, 5]}}] ;

t[1, 2][1, 1] = Table[If[i == j, TCCu, If[i == j + 1, TCCd, 0], 0],
{i, 1, m}, {j, 1, m}];
t[1, 2][2, 2] = Table[If[i == j, TBNs, 0], {i, 1, m}, {j, 1, m}];
t[1, 2][3, 3] = Table[If[i == j, TBNu, If[i == j + 1, TBNd, 0], 0],
{i, 1, m}, {j, 1, m}];
t[1, 2][4, 4] = Table[If[i == j, TBNs, 0], {i, 1, m}, {j, 1, m}];
t[1, 2][5, 5] = Table[If[i == j, TCCu, If[i == j + 1, TCCd, 0], 0],
{i, 1, m}, {j, 1, m}];
T[1, 2] = ArrayFlatten[{{t[1, 2][1, 1], Zo[m], Zo[m], Zo[m], Zo[m]},
{Zo[m], t[1, 2][2, 2], Zo[m], Zo[m], Zo[m]},
```

```
{Zo[m], Zo[m], t[1, 2][3, 3], Zo[m], Zo[m]},
{Zo[m], Zo[m], Zo[m], t[1, 2][4, 4], Zo[m]},
{Zo[m], Zo[m], Zo[m], Zo[m], t[1, 2][5, 5]}};

t[2, 3][1, 1] = Table[If[i == j, TCCs, 0], {i, 1, m}, {j, 1, m}];
t[2, 3][2, 2] = Table[If[i == j, TBNu, If[i == j + 1, TBNd, 0], 0],
{i, 1, m}, {j, 1, m}];
t[2, 3][3, 3] = Table[If[i == j, TBNs, 0], {i, 1, m}, {j, 1, m}];
t[2, 3][4, 4] = Table[If[i == j, TBNu, If[i == j + 1, TBNd, 0], 0],
{i, 1, m}, {j, 1, m}];
t[2, 3][5, 5] = Table[If[i == j, TCCs, 0], {i, 1, m}, {j, 1, m}];
T[2, 3] = ArrayFlatten[{{t[2, 3][1, 1], Zo[m], Zo[m], Zo[m], Zo[m]},
{Zo[m], t[2, 3][2, 2], Zo[m], Zo[m], Zo[m]},
{Zo[m], Zo[m], t[2, 3][3, 3], Zo[m], Zo[m]},
{Zo[m], Zo[m], Zo[m], t[2, 3][4, 4], Zo[m]},
{Zo[m], Zo[m], Zo[m], Zo[m], t[2, 3][5, 5]}};

t[3, 4][1, 1] = Table[If[i == j, TCCd, If[i + 1 == j, TCCu, 0], 0],
{i, 1, m}, {j, 1, m}];
t[3, 4][2, 2] = Table[If[i == j, TBNs, 0], {i, 1, m}, {j, 1, m}];
t[3, 4][3, 3] = Table[If[i == j, TBNd, If[i + 1 == j, TBNu, 0], 0],
{i, 1, m}, {j, 1, m}];
t[3, 4][4, 4] = Table[If[i == j, TBNs, 0], {i, 1, m}, {j, 1, m}];
t[3, 4][5, 5] = Table[If[i == j, TCCd, If[i + 1 == j, TCCu, 0], 0],
{i, 1, m}, {j, 1, m}];
T[3, 4] = ArrayFlatten[{{t[3, 4][1, 1], Zo[m], Zo[m], Zo[m], Zo[m]},
{Zo[m], t[3, 4][2, 2], Zo[m], Zo[m], Zo[m]},
{Zo[m], Zo[m], t[3, 4][3, 3], Zo[m], Zo[m]},
{Zo[m], Zo[m], Zo[m], t[3, 4][4, 4], Zo[m]},
{Zo[m], Zo[m], Zo[m], Zo[m], t[3, 4][5, 5]}};

t[4, 1][1, 1] = Table[If[i == j, TCCs, 0], {i, 1, m}, {j, 1, m}];
t[4, 1][2, 2] = Table[If[i == j, TBNd, If[i + 1 == j, TBNu, 0], 0],
{i, 1, m}, {j, 1, m}];
```

```
t[4, 1][3, 3] = Table[If[i == j, TBNs, 0], {i, 1, m}, {j, 1, m}];
t[4, 1][4, 4] = Table[If[i == j, TBNd, If[i + 1 == j, TBNu, 0], 0],
{i, 1, m}, {j, 1, m}];
t[4, 1][5, 5] = Table[If[i == j, TCCs, 0], {i, 1, m}, {j, 1, m}];
T[4, 1] = ArrayFlatten[{{t[4, 1][1, 1], Zo[m], Zo[m], Zo[m], Zo[m]},
{Zo[m], t[4, 1][2, 2], Zo[m], Zo[m], Zo[m]},
{Zo[m], Zo[m], t[4, 1][3, 3], Zo[m], Zo[m]},
{Zo[m], Zo[m], Zo[m], t[4, 1][4, 4], Zo[m]},
{Zo[m], Zo[m], Zo[m], Zo[m], t[4, 1][5, 5]}}];
```

The unit cell Hamiltonian

```
Hu = ArrayFlatten[{{H[1], T[1, 2], Zo[5m], Zo[5m]},
{T[1, 2]^†, H[2], T[2, 3], Zo[5m]},
{Zo[5m], T[2, 3]^†, H[3], T[3, 4]},
{Zo[5m], Zo[5m], T[3, 4]^†, H[4]}}];
```

The transfer matrix between unit cells

```
Tu = ArrayFlatten[{{Zo[5m], Zo[5m], Zo[5m], Zo[5m]},
{Zo[5m], Zo[5m], Zo[5m], Zo[5m]},
{Zo[5m], Zo[5m], Zo[5m], Zo[5m]},
{T[4, 1], Zo[5m], Zo[5m], Zo[5m]}}];
```

The transmission function as a function of energy

```
tr[ε_]:=Module[{gL, gR, ΣL, ΣL1, γL, ΣL2, ΣR, γR, GL, G, TLR},

ΣL1 = SelfEnergy[ε, V1][[5]];
ΣL = ArrayFlatten[{{ΣL1, Zop[m, 20m - m]},
{Zop[20m - m, m], Zop[20m - m, 20m - m]}}];
γL = i (ΣL - ΣL^†); (* The broadening functions of left lead *)

ΣL2 = SelfEnergy[ε, V5][[5]];
ΣR = ArrayFlatten[{{Zop[20m - m, 20m - m], Zop[20m - m, m]},
{Zop[m, 20m - m], ΣL2}}];
γR = i (ΣR - ΣR^†); (* The broadening functions of right lead *)
```

The recursive method to evaluate the Green's function

```
GL[1, 1] = Inverse[εIdentityMatrix[4 * 5m] – Hu – ΣL];
Do[GL[i, i] = Inverse[εIdentityMatrix[4 * 5m] – Hu–
 Tu†.GL[i – 1, i – 1].Tu] , {i, 2, M – 1}] ;
Do[GL[1, i] = GL[1, i – 1].Tu.GL[i, i], {i, 2, M – 1}];
GL[M, M] = Inverse[εIdentityMatrix[4 * 5m] – Hu–
 Tu†.GL[M – 1, M – 1].Tu – ΣR] ;
G[1, M] = GL[1, M – 1].Tu.GL[M, M];
TLR = Tr[γL.G[1, M].γR.G[1, M]†]//Chop//Quiet
]//Quiet;
```

Integrating the transmission function over the energy window to evaluate the current in meV

```
list = {#, tr[#]//Quiet//Chop}&/@
Range[–(eVb + 0.201), 0.201, 0.01];
f = Interpolation[list, InterpolationOrder → 1];
NIntegrate [f[ε] (−1/(1+Exp[(ε−μB)/(k T0)]) + 1/(1+Exp[(ε−μT)/(k T0)])),
{ε, –(eVb + 0.2), 0.2}] * 10^3
]
```

Evaluating the I-V plot; purple curve in Fig. (4.11)

```
ProgressIndicator[Dynamic[eVb], {0, 1}]
Do[Print[eVb, " I =", Timing[FuncI[eVb]]//Chop], {eVb, 0, 1, 0.01}];
ListI = {#, FuncI[#]//Chop}&/@Range[0, 1, 0.01]
fI = Interpolation[ListI, InterpolationOrder → 1];
Plot[fI[Vb], {Vb, 0, 1}]
```

Bibliography

[1] Dmitri E. Nikonov M. P. Anantram Mark S. Lundstrom. In: *IEEE* 96 (2008), p. 1511.

[2] S.Datta. In: *IEDM'02. International* (2002), pp. 703–706.

[3] S.Datta. In: *Superlattice. Microst.* 28 (2000), pp. 253–278.

[4] S.Datta. "Electronic Transport in Mesoscopic Systems". In: *Cambridge University Press* (1995).

[5] K. S. Novoselov et al. In: *American Association for the Advancement of Science* 306 (2004), pp. 666–669.

[6] A. K. Geim and K. S. Novoselov. In: *Nature Materials* 6 (2007), pp. 183–191.

[7] P. R. Wallace. In: *Phys. Rev.* 71 (1947), p. 622.

[8] S. V. Morozov D. Jiang M. I. Katsnelson I. V. Grigorieva S. V. Dubonos K. S. Novoselov A. K. Geim and A. A. Firsov. In: *Nature* 438 (2005), pp. 197–200.

[9] K. S. Novoselov M. I. Katsnelson and A. K. Geim. In: *Nat. Phys.* 2 (2006), p. 620.

[10] F. Schwierz. In: *Nat. Nanotech.* 5 (2010), p. 487.

[11] M. Bao R. Cheng J. Bai Y. Liu Y. Qu K. L. Wang Y. Huang andX. Duanz L. Liao Y.-C. Lin. In: *Nature* 467 (2010), p. 305.

[12] Y. Lee X. Xu J.-S. Park Y. Zheng J. Balakrishnan T. Lei H. R. Kim Y. I. Song Y.-J. Kim K. S. Kim B. Ozyilmaz J.-H. Ahn B. H. Hong S. Bae H. Kim and S. Iijima. In: *Nat. Nanotech.* 5 (2010), p. 574.

[13] L. Gaudreau J. Osmond M. Bernechea F. P. G. de Arquer F. Gatti G. Konstantatos M. Badioli and F. H. L. Koppens. In: *Nat. Nanotech.* 7 (2012), p. 363.

[14] S. V. Morozov L. Britnell R. Jalil L. A. Ponomarenko P. Blake K. S. Novoselov K. Watanabe T. Taniguchi A. S. Mayorov R. V. Gorbachev and A. K. Geim. In: *Nano Lett* 6 (2011), p. 2396.

[15] A. F. Young J. Hone P. Kim K. L. Shepard I. Meric C. R. Dean. In: *IEEE IEDM Tech. Dig.* (2010), pp. 556–559.

[16] R. Jalil B. D. Belle F. Schedin M. I. Katsnelson L. Eaves S. V. Morozov A. S. Mayorov N. M. R. Peres A. H. Castro Neto J. Leist A. K. Geim L. A. Ponomarenko L. Britnell R. V. Gorbachev and K. S. Novoselov. In: *Nano Lett.* 12 (2012), p. 1707.

[17] Y-J Yu D-Y Lee S. H. Lee P. Kim J. Hone M. S. Choi G-H. Lee and W. J. Yoo. In: *Nat Commun* 4 (2013), p. 1624.

[18] C-W Huang-X. Zou L. Liao S. Chen Z. Fan K. Zhang W. Wu X. Xiao C. Jiang W-W Wu J. Wang Q. Yao. In: *Adv Mater* 28 (2016), p. 8302.

[19] G. Chen Z. Shi C-C Liu L. Zhang G. Xie M. Cheng D. Wang R. Yang D. Shi K. Watanabe T. Taniguchi Y. Yao Y. Zhang W Yang and G. Zhang. In: *Nat Mater* 12 (2013), p. 792.

[20] Y. Zhang U.C. Coskun W. Bao C.N. Lau F. Miao S. Wijeratne. In: *Science* 317 (2007), p. 1530.

[21] S.M. Goodnick D.K. Ferry. "Transport in nanostructures". In: *Cambridge University Press* (1997).

[22] K. Flensberg H. Bruus. "Many-Body Quantum Theory in Condensed Matter Physics". In: *Oxford University Press* (2004).

[23] M. Buttiker Ya.M. Blanter. "Shot Noise in Mesoscopic Conductors". In: *Physics Reports* 336 (2000), p. 1.

[24] P. Dietl. "Diploma Thesis: Numerical Studies of Electronic Transport through Graphene Nanoribbons with Disorder". In: (2009).

[25] G. Metalidis. "Dissertation: Electronic Transport in Mesoscopic Systems". In: (2007).

[26] E. N. Economou. "Green's Functions in Quantum Physics". In: *Springer Verlag* (1983).

[27] G. D. Mahan. "Many Particle Physics". In: *Kluwer Acad./Plenum Publ.* (2000).

[28] Y. Imry. "Introduction to Mesoscopic Physics". In: *Oxford University Press* (1997).

[29] D. S. Fisher and P. A. Lee. In: *Phys. Rev. B* 23 (1981), p. 6851.

[30] D. J. Thouless and S. Kirkpatrick. In: *J. Phys. C: Solid State Phys* 14 (1981), p. 235.

[31] J. M. Lope z Sancho M. P. Lope z Sancho and J. Rubio. In: *J. Phys. F* 15 (1985), p. 851.

[32] R. W. Giannetta M. Hannan I. Adesida D. Guan U. Ravailoi and M. R. Melloch. In: *Phys. Rev. B* 67 (2003), p. 205328.

[33] K. Takayanagi T. Ando and K. Kobayashi. In: *Physica E: Low-dimensional Systems and Nanostructures* 2 (2007), pp. 228–232.

[34] F. Schedin. In: *Nature Materials* 6 (2007), pp. 652 –655.

[35] H. B. Heersch. In: *Nature* 446 (2007), pp. 56–59.

[36] E. McCann. "Electronic properties of monolayer and bilayer graphene Graphene Nanoelectronics". In: *Berlin: Springer* (2012).

[37] T. Nakanishi T. Ando and R. Saito. In: *J. Phys. Soc. Jpn.* 67 (1998), pp. 2857–2862.

[38] J. C. Charlier L. E. F. F. Torres S. Roche. "Introduction to Graphene-Based Nanomaterials". In: *Cambridge University Press, New York* (2014).

[39] J. P. Hobson and W. A. Nierenberger. In: *Phys. Rev.* 89 (1953), p. 662.

[40] D. AKINWANDE H.-S. PHILIP WONG. "Carbon Nanotube and Graphene Device Physics". In: *(cambridge university press)* (2011).

[41] Hassan Raza. "NanoScience and Technology". In: *Springer* (2011).

[42] V. M. Pereira and A. H. Castro Neto. In: *Phys. Rev. B* 80 (2009), p. 045401.

[43] P. Ming F. Liu and J. Li. In: *Phys. Rev. B* 76 (2007), p. 064120.

[44] H.Jang S.Y.Lee J.M.Kim K.S.Kim J.H.Ahn P.Kim J.Choi K.S.Kim Y.Zhao and B. H. Hong. In: *Nature* 457 (2009), p. 706.

[45] L. D. Landau and E. M. Lifshitz. "Theory of Elasticity". In: *Pergamon* (1986).

[46] G. B. Stence T. Wen D. G. Proctor E. J. Seldin. In: *J. Appl. Phys.* 41 (1970), p. 3373.

[47] W. A. Harrison. "Elementary Electronic Structure". In: *World Scientific* (1999).

[48] C. Piermarocchi G. Grosso. In: *Phys. Rev. B* 51 (1995), p. 16772.

[49] S. C. Erwin D. A. Papaconstantopoulos M. J. Mehl and M. R. Pederson. "Tight-Binding Approach to Computational Materials Science". In: *Materials Research Society, Pittsburgh* (1998), p. 221.

[50] F. Guinea A. H. Castro Neto. In: *Phys. Rev. B* 75 (2007), p. 045404.

[51] N. M. R. Peres K. S. Novoselov A. H. Castro Neto F. Guinea and A. K. Geim. In: *Rev. Mod. Phys.* 81 (2009), p. 109.

[52] A. K. Geim and K. S. Novoselov. In: *Nat. Mater.* 6 (2007), p. 183.

[53] N. M. R. Peres K. S. Novoselov A. H. Castro Neto F. Guinea and A. K. Geim. In: *Rev. Mod. Phys.* 81 (2009), p. 109.

[54] I. Meric C. Lee L. Wang S. Sorgenfrei K. Watanabe T. Taniguchi P. Kim K. L. Shepard C. R. Dean A. F. Young and J. Hone. In: *Nature Nanotechnology* 5 (2010), p. 722.

[55] A. K. Geim L. A. Ponomarenko A. Mishchenko M. T. Greenaway T. M. Fromhold K. S. Novoselov L. Britnell R. V. Gorbachev and L. Eaves. In: *Nat. Commun.* 4 (2013), p. 1794.

[56] R. Jalil B. D. Belle F. Schedin A. Mishchenko T. Georgiou M. I. Katsnelson L. Eaves S. V. Morozov N. M. R. Peres J. Leist A. K. Geim K. S. Novoselov L. Britnell R. V. Gorbachev and L. A. Ponomarenko. In: *Science* 335 (2012), p. 947.

[57] X. Xu S. R. Patil U. Hetmaniuk Y. Zhao Z. Wan and M. P. Anantram. In: *Sci. Rep.* 5 (2015), p. 10712.

[58] T. E. Tanoue H. Mizuta. "physics and applications of resonant tunnelling diodes". In: *Cambridge University Press* (2006).

[59] T. Kim S.-H. Cho K. Kim J.-Y. Choi and H.-J. Chung. In: *Nature.* 479 (2011), p. 338.

[60] L. Brown-P. Y. Huang R. W. Havener D. A. Muller M. P. Levendorf C.-J. Kim and J. Park. In: *Nature.* 488 (2012), p. 627.

[61] Q. Gao S. C. de la Barrera and R. M. Feenstra. In: *J. Vac. Sci. Technol. B.* 32 (2014), 04E101.

[62] L. Brey. In: *Phys. Rev. A.* 2 (2014), p. 014003.

[63] D. Jena R. M. Feenstra and G. Gu. In: *J. Appl. Phys* 111 (2012), p. 043711.

[64] F. Zahid K. M. M. Habib and R. K. Lake. In: *Appl. Phys. Lett.* 98 (2011), p. 192112.

[65] Y. Kamakura N. Mori T. Edagawa and L. Eaves. In: *Jpn. J. Appl. Phys.* 53 (2014), 04EN04.

[66] B. Sensale-Rodriguez. In: *Appl. Phys. Lett.* 103 (2013), p. 123109.

[67] F. T. Vasko. In: *Phys. Rev. B.* 87 (2013), p. 075424.

[68] H. Haug and A. P. Jauho. In: *Springer* (1996).

[69] S. Luryi. In: *Appl. Phys. Lett.* 52 (1988), p. 501.

[70] U. Hetmanuik Y. Zhao Z. Wan and M. P. Anantram. In: *IEEE ELECTRON DEVICE LETTERS* 37 (2016), p. 1242.

[71] S. N. Karmakar P. Dutta S. K. Maiti. In: *Journal of Applied Physics* 114 (2013).

[72] J. M. Lopez Sancho M. P. Lopez Sancho and J. Rubio. In: *J. Phys. F: Met. Phys* 14 (1984), p. 1205.

[73] J. Kudrnovsky M. Sob I. Turek V. Drchal and P. Weinberger. "Electronic Structure of Disordered Alloys, Surfaces and Interfaces". In: *Springer* (1997).

[74] I. Zasada J. Sawiska and Z. Klusek. In: *Phys. Rev. B* 81 (2010), p. 155433.

[75] N. Peres R. Ribeiro. In: *Phys. Rev. B* 81 (2011), p. 235312.

[76] A. S. Arnold et al. In: *(Springer, 1990)* (1990).

[77] C. D. Parker W. D. Goodhue E. R. Brown T. C. L. G. Sollner and C. L. Chen. In: *Appl. Phys. Lett.* 55 (1989), p. 1777.

[78] F. Mandl. "Quantum Mechanics". In: *(Wiley, 1992)* (1992).

[79] J. GASKELL. "Dissertation: High-frequency oscillations in graphene resonant tunnelling heterostructures". In: (2016).

[80] S. M. Sze and K. K. Ng. "Physics of Semiconductor Devices". In: *Wiley* (2006).

[81] L. Esaki. In: *Phys. Rev* 109 (1958), p. 603.

[82] B. K. Ridley. In: *Proc. Phys. Soc.* 82 (1963), p. 954.

[83] C. Hilsum. In: *Proc. IRE* 50 (1962), p. 185.

[84] J. B. Gunn. In: *Solid State Commun.* 1 (1963), p. 88.

[85] L. Esaki and R. Tsu. In: *IBM Journal of Research and Development* 14 (1970), p. 61.

[86] R. F. Kazarinov and R. A. Suris. In: *Sov. Phys. Semicond. USSR* 5 (1971), p. 707.

[87] L. Esaki L. L. Chang and R. Tsu. In: *Appl. Phys. Lett.* 24 (1974), p. 593.

[88] S. Suzuki M. Asada and N. Kishimoto. In: *Jpn. J. Appl. Phys.* 47 (2008), p. 4375.

[89] A. Teranishi H. Asugiyama S. Suzuki M. Asada and H. Yokoyama. In: *Appl. Phys. Lett.* 97 (2010), p. 242102.